

Prompt Photon Production in
Proton-Proton Collisions at
 $\sqrt{s} = 200\text{GeV}$

Takuma Horaguchi



Thesis submitted to the Department of Physics in
partial fulfillment of the requirements for the degree of

Doctor of Science

at Tokyo Institute of Technology

February, 2006

Abstract

Cross section for production of prompt photon in proton-proton collisions at $\sqrt{s} = 200$ GeV at the PHENIX experiment is reported. This is the prompt photon measurement at the highest energy ever made in the proton-proton collisions. Prompt photon means a photon directly produced by parton-parton collision.

Proton-proton collisions at the Relativistic Heavy Ion Collider (RHIC) can provide information on the structure of the proton. Prompt photon at high transverse momentum is produced mainly by quark-gluon Compton scattering ($qg \rightarrow \gamma q$). The measurement of the prompt photon cross section is a test of perturbative Quantum Chromodynamics (pQCD), and it gives us the gluon distribution in the nucleon.

In PHENIX, data with an integrated luminosity of 0.35pb^{-1} have been collected in the run of year 2003 at $\sqrt{s} = 200$ GeV. The analyzed data sample consists of 56M events with the high- p_T trigger. The measured p_T range is from 3.25 GeV/c to 16 GeV/c.

Prompt photons and photons from hadron decays are detected by the PHENIX Electro-Magnetic Calorimeter (EMCal). The EMCal consists of six sectors of lead scintillator calorimeter and two sectors of lead glass calorimeter. Each of these sectors covers the pseudo-rapidity range of $|\eta| < 0.35$ and the azimuthal angle of 0.4 rad. The cross section was measured over 4 orders of magnitude. The cross section shows a steep decrease as p_T increases. The total systematic error in the cross section is evaluated to be 14.8% at the largest p_T bin and 93.1% at the smallest p_T bin. The main source of the systematic error is uncertainty in the evaluation of the missing π^0 photon. The uncertainty of normalization due to the luminosity error is 9.7%.

It is shown that the present result is consistent with a next-to-leading-order pQCD calculation over the 4 orders of magnitude of cross section within experimental and theoretical uncertainties. The theoretical curve shows however slightly less steep fall as a function of p_T , which is an open subject for future theoretical studies. It was found that x_T scaling is valid with the present data. This work also serves as a basis of the measurement of the polarized gluon distribution function of the proton in the future. It is useful also as a reference of the quark gluon plasma search in heavy ion collisions.

Contents

1	Introduction	16
2	Theoretical Background	20
2.1	Perturbative Quantum ChromoDynamics (pQCD)	20
2.1.1	Quarks and Leptons	20
2.1.2	The QCD Lagrangian	21
2.1.3	Asymptotic Freedom and Confinement	22
2.1.4	pQCD in Hadron Collisions	25
2.1.5	Parton Distribution Function (PDF)	25
2.1.6	Fragmentation Function (FF)	28
2.2	Prompt Photon Production	32
2.2.1	Prompt Photon Production in pQCD	32
2.2.2	Overview of Experiments	34
2.3	Spin Physics	39
2.3.1	Nuclear Spin Problem	39
2.3.2	Polarized Gluon Distribution Function	40
2.4	Heavy Ion Physics	41
3	Experimental Setup	43
3.1	RHIC Accelerator	43
3.2	PHENIX Detector Overview	44
3.3	Magnet System	48
3.4	Beam Detectors	51
3.4.1	Beam-Beam Counters (BBC)	51
3.4.2	Zero Degree Calorimeters (ZDC)	51
3.5	Central Arm Spectrometers	53
3.5.1	Drift Chamber (DC)	53
3.5.2	Pad Chamber (PC)	59
3.5.3	Ring Imaging Cherenkov Detector (RICH)	60
3.5.4	Time Expansion Chamber (TEC)	62
3.5.5	Time Of Flight Counter (TOF)	62

3.6	ElectroMagnetic Calorimeter (EMCal)	63
3.6.1	Overview of EMCal	63
3.6.2	Lead Scintillator Calorimeter (PbSc)	64
3.6.3	Lead Glass Calorimeter (PbGl)	67
3.6.4	Shower Shape Measurement on Photon Identification	74
3.7	PHENIX Muon Arm	74
3.7.1	Muon Tracker (MuTr)	76
3.7.2	Muon IDentifier (MuID)	76
3.8	PHENIX Data Acquisition (DAQ) System	77
3.8.1	DAQ Overview	77
3.8.2	Front-end Electronics Module for EMCal	79
3.8.3	Level 1 Trigger	81
4	Analysis	84
4.1	Outline of Analysis	84
4.2	Run and Trigger Selection	85
4.3	Calibration of EMCal	86
4.3.1	Quality Assurance of EMCal	86
4.3.2	Energy Calibration	86
4.3.3	Time of Flight Calibration	92
4.4	Photon Cluster Selection	92
4.5	π^0 yield Extraction	97
4.5.1	Fiducial Area	97
4.5.2	π^0 Reconstruction	97
4.5.3	Tool of EMCal Detector Simulation	98
4.5.4	π^0 Missing Ratio	103
4.6	Contribution of η , η' , ω	103
4.7	Charged Particle Background	106
4.8	Neutral Particle Background	108
4.9	Non-Vertex Origin Background	112
4.10	Correction for Photon Conversion	120
4.11	Photon Efficiency with High- p_T Trigger	122
4.12	Trigger Bias of Minimum Bias Trigger	123
4.13	Acceptance and Smearing Correction	123
4.14	Cross Section and Systematic Errors	123
4.14.1	Evaluation of Cross Section	123
4.14.2	Systematic errors	126
5	Results and Discussion	132
5.1	Results	132
5.2	Comparison with Other Experiments	134

5.3	x_T Scaling	134
5.4	Comparison with NLO pQCD Calculation	137
5.5	Comparison with π^0 cross section	137
6	Conclusion	143
	Acknowledgement	145
A	PHENIX Coordinate System	147
B	Kinematics of π^0 Decay	149
C	Prompt Photon Production at Leading Order	151
D	Cross Section from Other Experiments	153
E	Optical Alignment System for Muon Trackers	160
E.1	Optical Alignment System (OASys)	160
E.2	Results	162

List of Tables

2.1	Summary of up, down, strange quarks. Q is the electric charge. J is the spin. I_z is the third component of isospin. B is the baryon number. S is the strangeness. C is the charm quantum number. b is the bottom quantum number. T is the top quantum number [14].	21
2.2	Summary of charm, bottom, top quarks [14].	22
2.3	Summary of leptons. T_3 is the third component of weak isospin. L_e, μ, τ is the electron, muon, τ lepton numbers, respectively [14].	23
2.4	Summary of gauge bosons [14].	23
2.5	The parton-parton two body scattering differential cross sections. Factors of $\pi\alpha_s^2/s^2$, $\pi\alpha\alpha_s/s^2$ and $\pi\alpha^2/s^2$ have been factored out of the purely strong interaction, the single photon production and the double photon production processes, respectively. The e_q is the electric charge of quark. The s, t and u are the Mandelstam variables [75].	26
2.6	Measurements of prompt photon.	40
3.1	Summary of the collected data with PHENIX at RHIC during the recent RHIC beam period.	44
3.2	Summary of the PHENIX detector subsystems.	47
3.3	Summary of the resolution of PHENIX subsystems.	48
3.4	Fundamental parameters of PHENIX EMCAL. Moliere radius is defined as $R_M = 21\text{MeV} \times X_0/E_c$, where E_c is the critical energy. 99% of the energy is inside a radius $3R_M$	65
3.5	The table of ERT trigger thresholds in RUN2003.	82
4.1	Production and branching ratio of other hadrons to π^0 [125].	108
4.2	Single photon conversion correction factors. The errors are evaluated systematic errors of energy smearing, vertex cut, and acceptance.	122

4.3	π^0 conversion correction factors. The errors are evaluated systematic errors of energy smearing, vertex cut, and acceptance.	122
4.4	The acceptance and smearing correction for each trigger mask period.	124
4.5	Table of systematic errors.	130
4.6	Table of systematic error (continued).	131
5.1	Invariant cross section for prompt photon production in proton-proton collisions at $\sqrt{s} = 200$ GeV with the statistical uncertainty, and the systematic uncertainty for each p_T bin.	142
D.1	Data table of invariant cross sections of prompt photon by NA24 collaboration at the beam momentum of 300 GeV ($\sqrt{s} = 23.75$ GeV) [82].	153
D.2	Data table of invariant cross sections of prompt photon by R110 collaboration at $\sqrt{s} = 63$ GeV [80].	153
D.3	Data table of invariant cross sections of prompt photon by R806 collaboration at $\sqrt{s} = 63$ GeV.	154
D.4	Data table of invariant cross sections of prompt photon by UA1 collaboration at $\sqrt{s} = 546$ GeV [84].	154
D.5	Data table of invariant cross sections of prompt photon by UA1 collaboration at $\sqrt{s} = 630$ GeV [84].	155
D.6	Data table of invariant cross sections of prompt photon by UA2 collaboration at $\sqrt{s} = 630$ GeV [85].	155
D.7	Data table of invariant cross sections of prompt photon by UA6 collaboration at the beam momentum of 315 GeV ($\sqrt{s} = 24.3$ GeV) [77].	156
D.8	Data table of invariant cross sections of prompt photon by UA6 collaboration at the beam momentum of 315 GeV ($\sqrt{s} = 24.3$ GeV) [78].	156
D.9	Data table of invariant cross sections of prompt photon by WA70 collaboration at the beam momentum of 280 GeV ($\sqrt{s} = 22.3$ GeV) [81].	156
D.10	Data table of invariant cross sections of prompt photon by CDF collaboration at $\sqrt{s} = 1800$ GeV [86].	157
D.11	Data table of invariant cross sections of prompt photon by D0 collaboration at $\sqrt{s} = 1800$ GeV [87].	158
D.12	Data table of invariant cross sections of prompt photon by E704 collaboration at the beam momentum of 200 GeV ($\sqrt{s} = 19.4$ GeV) [79].	158

D.13 Data table of invariant cross sections of prompt photon by E706 collaboration at the beam momentum of 530 GeV ($\sqrt{s} = 31.5$ GeV) [76].	159
D.14 Data table of invariant cross sections of prompt photon by E706 collaboration at the beam momentum of 800 GeV ($\sqrt{s} = 38.7$ GeV).	159

List of Figures

2.1	Summary of the values of α_s as a function of μ . The lines show the central values and the $\pm 1\sigma$ limits of our average [14]. . . .	24
2.2	Production of a high p_T hadron h in a hard scattering process.	27
2.3	An example of the proton structure function $F_2(x, Q^2)$ measured by H1, ZEUS, BCDMS, E665, NMC and SLAC [14]. . .	29
2.4	The distribution of the unpolarized parton density as a function of x using the MRST2001 [53] parameterization at a scale $\mu^2 = 10\text{GeV}^2$ [14].	30
2.5	The fragmentation functions expressed by the total charged particle production cross sections obtained in the e^+e^- collisions are shown as a function of x , where $x = (2E_h/\sqrt{s})$ is the scaled hadron energy [14].	31
2.6	A sketch of prompt photon production for quark gluon Compton scattering process (left) and quark anti-quark annihilation process (right).	34
2.7	A sketch of prompt photon production for fragmentation process (left). A sketch of photon production from hadron decay (right).	35
2.8	The Feynman diagrams of prompt photon production at leading-order for quark gluon Compton scattering process.	35
2.9	The Feynman diagrams of prompt photon production at leading-order for quark anti-quark annihilation process.	35
2.10	The fraction of $gq \rightarrow \gamma q$ and $q\bar{q} \rightarrow \gamma g$ as function of p_T in $p+p$ at $\sqrt{s} = 200\text{GeV}$	36
2.11	The fraction of $gq \rightarrow \gamma q$ and $q\bar{q} \rightarrow \gamma g$ as function of p_T in $p+\bar{p}$ at $\sqrt{s} = 200\text{GeV}$	36
2.12	The fraction of $gq \rightarrow \gamma q$ and $q\bar{q} \rightarrow \gamma g$ as function of p_T in $p+\bar{p}$ at $\sqrt{s} = 1800\text{GeV}$	37
2.13	The fraction of $gq \rightarrow \gamma q$ and $q\bar{q} \rightarrow \gamma g$ as function of x_T in $p+p$ at $\sqrt{s} = 200\text{GeV}$	37

2.14	The fraction of $gq \rightarrow \gamma q$ and $q\bar{q} \rightarrow \gamma g$ as function of x_T in $p + \bar{p}$ at $\sqrt{s} = 200\text{GeV}$	38
2.15	The fraction of $gq \rightarrow \gamma q$ and $q\bar{q} \rightarrow \gamma g$ as function of x_T in $p + \bar{p}$ at $\sqrt{s} = 1800\text{GeV}$	38
2.16	The ratio of direct process to fragmentation process as a function of photon p_T	39
2.17	A sketch of the collisions of the polarized protons. The red circles denote the proton beam. The arrows denote the direction of the proton spin. The top figure shows the helicity of beam1 (left):+, beam2 (right):- . The bottom figure shows the helicity of beam1 (left):+, beam2 (right):-	41
2.18	Phase diagram as functions of density and temperature.	42
3.1	Schematic view of the RHIC complex.	45
3.2	A cutaway drawing of the PHENIX detector is shown. The major detector subsystems are pointed by labelled arrows.	46
3.3	The PHENIX magnets are shown in perspective and cut away to show the interior structures. Arrows indicate the beam direction of RHIC.	49
3.4	CM and MM magnetic field lines are shown on a cutaway drawing of the PHENIX magnets. The beam line is parallel to the Z axis in this figure. The beams collide at $Z = 0$	50
3.5	A single Beam-Beam counter consists of one-inch mesh dynode photo-multiplier tubes with a 3 cm thick quartz radiator.	52
3.6	A BBC array consists of 64 BBC elements.	52
3.7	A sketch of a collision and produced particles coming to the BBCs. T_N and T_S are the averaged hit time of incoming particles.	53
3.8	The top picture is the view of the collision region and the bottom picture is the schematic view of the ZDC location including deflection of protons and charged fragments.	54
3.9	The design of the production of Tungsten Module. Dimensions are in mm.	55
3.10	The central spectrometer has two arms which are viewed in a cut through the collision point.	56
3.11	The view of DC frame.	57
3.12	The schematic view of wire positions within one sector and inside the anode plane.	58
3.13	The distribution of momentum resolution.	59
3.14	The pad and pixel geometry (left). A cell defined by three pixel is at the center of the right picture.	60
3.15	A cutaway view of one arm of the PHENIX RICH detector.	61

3.16	TEC six-plane sector.	62
3.17	Schematic view of the components of a single TOF panel which consists of 96 plastic scintillation counters with photomultiplier tubes at both ends, light guides and supports.	63
3.18	Interior view of a PbSc calorimeter module showing a stack of scintillator and lead plates, wavelength shifting fiber readout and leaky fiber inserted in the central hole.	66
3.19	PbSc EMCal energy linearity measured in beam tests at BNL (left) and CERN (right). The residual (calorimeter measured energy less the beam energy, divided by the beam energy) is shown for the 5x5 tower energy sum. The solid lines show total systematic uncertainties in the analysis.	67
3.20	PbSc EMCal energy resolution obtained by beam tests at CERN and BNL. The dashed line shows the fit to a linear formula ($\sigma(E)/E = 1.2\% + 6.2\%/\sqrt{E(\text{GeV})}$). The dashed dotted line shows the fit to the quadratic formula ($\sigma(E)/E = 2.1\% \oplus 8.1\%/\sqrt{E(\text{GeV})}$), where \oplus denotes a root of the quadratic sum, $a \oplus b = \sqrt{a^2 + b^2}$	68
3.21	PbSc timing resolution for different particles. Top: lineshape for 1 GeV/c electrons, pions and protons. Bottom: resolution in the momentum range of 0.3-1.0 GeV/c.	69
3.22	Expanded view of a lead-glass detector supermodule.	70
3.23	PbGl energy resolution versus incident energy.	71
3.24	PbGl timing resolution versus energy deposit in a single module for positrons of incident momenta 0.5, 0.75, 1.0, 1.5, 2.0, 3.0, and 4.0 GeV/c and for 1.0 GeV/c pions.	72
3.25	Pion rejection factor versus incident energy.	73
3.26	χ^2 distribution for showers induced by 2 GeV/c electrons and pions in the PbSc calorimeter.	75
3.27	Shower profile in EMCal.	75
3.28	Schematic of PHENIX Muon Arm.	76
3.29	Schematic diagram of the PHENIX On-Line system.	80
3.30	Block diagram of the energy and timing measurement circuits.	81
3.31	Schematic pattern of the EMCal fast trigger summing operation.	83
4.1	The vertex position distribution of BBC in run 92446.	85
4.2	The number of hits for each channel in one sector (W0) for photon energy between 3.0 GeV and 4.0 GeV is shown in (a). The number of hits for each channel in one sector (W0) for run between 87791 and 89211 is shown in (b). The color filled bins are removed as a hot channel.	87

4.3	Hot and dead tower map. Top left is W3 and top left is E3. The black area is removed in this analysis.	88
4.4	Deposited energy $\times 1/\cos(\theta)$ distribution by charged particles with more than 0.4 GeV/c, when cluster has its maximum tower in (63,12) in W0 sector.	89
4.5	Invariant mass distribution with p_T of more than 1.0 GeV/c when one of two clusters have its maximum tower in (63,13) in W0 sector.	89
4.6	Diagram of the basic procedure of energy calibration and its iterative work. The final correction factor is the product of all the correction factor.	90
4.7	Deviation of the MIP peak in 1st (black bottom), 2nd (red middle), and 3rd (green middle) iteration in W0 sector. The correction factors for a tower, named as C1 to C3 respectively, are defined as the ratio between the expected MIP energy and the observed MIP peak. The final correction is the product of all the factors.	91
4.8	Deviation of the π^0 peak in 1st (black bottom), 2nd (red middle), 3rd (green middle), and 4th (blue top) iteration in W0 sector. The correction factors for a tower, named as C1 to C4 respectively, are defined as the ratio between the expected π^0 energy and the observed π^0 peak. The final correction is the product of all the factors.	91
4.9	TOF distribution for one tower.	93
4.10	TOF peak distributions for PbSc (left) and PbGl (right). The left figure has double peak.	93
4.11	Functions to describe energy dependence of TOF.	94
4.12	Photon shape cut efficiency in PbSc (west).	95
4.13	Photon shape cut efficiency in PbSc (east).	96
4.14	Photon shape cut efficiency in PbGl (east).	96
4.15	Fiducial area is shown. The towers from the arm edge is used as a veto region.	97
4.16	An example of π^0 mass distribution. The blue region is π^0 mass window. The green region is used for fitting of combinatorial background.	99
4.17	Invariant mass distribution of two photons with minimum energy cut at 150 MeV. Each panel corresponds to a certain photon p_T (West Arm).	100
4.18	Invariant mass distribution of two photons with minimum energy cut at 150 MeV. Each panel corresponds to a certain photon p_T (East Arm).	101

4.19	The fraction of π^0 photon signal in West Arm.	102
4.20	The fraction of π^0 photon signal in East Arm.	102
4.21	π^0 missing ratio R . Red line is for West arm and green line is for East arm.	104
4.22	The error of π^0 missing ratio $\Delta(1 + R)$ for West Arm is shown. Red line is $(1 + R)$ and blue line is $(1 + R) \pm \Delta(1 + R)$	104
4.23	The error of π^0 missing ratio $\Delta(1 + R)$ for East Arm is shown. Red line is $(1 + R)$ and blue line is $(1 + R) \pm \Delta(1 + R)$	105
4.24	The fraction of 1tag and merged photon for π^0 photon which hits the EMCal west. The fraction is normalized to all the photon originating from π^0 decay. The green line represents the fraction of merged photon and the red line represents the fraction of merged photon + 1tag.	105
4.25	The fraction of 1tag and merged photon for π^0 photon which hits the EMCal east. The fraction is normalized to all the photon originating from π^0 decay. The green line represents the fraction of merged photon and the red line represents the fraction of merged photon + 1tag.	106
4.26	The distortion of factor of non- π^0 hadronic decay contribution by the π^0 merge in the West arm.	107
4.27	The distortion of factor of non- π^0 hadronic decay contribution by the π^0 merge in the East arm.	107
4.28	DC track occupancy ($z \geq 0$) of $\phi(\text{rad})$ along the run sequence. The top part corresponds to the east arm. The bottom part corresponds to the west arm.	109
4.29	DC track occupancy ($z < 0$) of $\phi(\text{rad})$ along the run sequence. The top part corresponds to the east arm. The bottom part corresponds to the west arm.	109
4.30	Track matching of direction in z of EMCal with DC track.	110
4.31	Track matching of direction in ϕ of EMCal with DC track.	110
4.32	A sketch of the trajectory of a charged hadron.	111
4.33	Extrapolations of the spectra. Pions are from the measurement of identified charged hadrons, Dotted lines: extrapolation, solid curves: used in this analysis. Black represents π^- . Blue represents \bar{p}	113
4.34	Input spectra compared to the pion spectra. Extrapolation to high p_T region is done with the combination of measured spectra and a PYTHIA output. Black squares are from PHENIX measurements. Blue line is from PYTHIA. Red line shows a connection of data (low p_T) and PYTHIA (high p_T). Red dotted lines show a systematic error bands.	114

4.35	Comparison of the EMCal response with \bar{p} data. An additional scale factor 0.85 ± 0.10 is needed to adjust them. The bottom panel shows the difference between the measurement and the calculation after this tuning. Three lines show the energy scale uncertainty. Black represents the momentum of particles. Red represents $ecore \times \cos(\theta)$. Blue is Black \times response matrix.	115
4.36	Comparison of the EMCal response with \bar{p} data with a photon shape cut. Only for \bar{p} , an additional factor of 1.6 is needed. The bottom panel shows the difference after the tuning. Three lines show the energy scale uncertainty. Black represents the momentum of particles. Red represents $ecore \times \cos(\theta)$. Blue is Black \times response matrix.	116
4.37	Estimation of anti-neutron contributions. Black represents photon cluster. Red represents the estimated anti-neutron spectra. Blue represents red \times response matrix \times factor. The contributions to the total photon clusters are shown in the bottom panel.	117
4.38	Error in contamination evaluation due to variations of the input spectra. Black represents anti-neutron. Green represents K_L^0 . Red represents neutron.	118
4.39	Error in contamination evaluation due to variations of the correction factors of the energy scale. Black represents anti-neutron. Green represents K^{0L} . Red represents neutron.	119
4.40	Origins of EMCal clusters in $r - z$ plane. Definition of θ_r is also shown. Red points are taken as secondary sources because of large θ_r	120
4.41	Energy distribution of all and non-vertex origin secondary clusters from data.	121
4.42	p_T spectra of input and output (FastMC). Black represents input spectra, while red represents output spectra after acceptance cut and smearing effect.	125
4.43	Invariant cross section in West Arm with statistical error only.	127
4.44	Invariant cross section in East Arm with statistical error only.	128
4.45	Ratio of prompt photon signal to all photon ($N_\gamma^{raw}/N_\gamma^{all}$). The black line shows a second polynomial function fit to the signal fraction.	129
5.1	Invariant cross section for prompt photon production with statistical error and systematic error. Black line represents statistical error. Color filled band represents systematic error.	133

5.2	Comparison of the obtained invariant cross section at $\sqrt{s} = 200$ GeV with the results of other experiments at \sqrt{s} between 19.4 and 63 GeV.	135
5.3	The results of other experiments at \sqrt{s} between 24.3 and 1800 GeV are shown.	136
5.4	Cross section for prompt photon production $(\sqrt{s})^{5.0} \times E \frac{d^3\sigma}{dp^3}$ at \sqrt{s} between 19.4 and 1800GeV.	138
5.5	Cross section for π^0 production $(\sqrt{s})^{6.3} \times E \frac{d^3\sigma}{dp^3}$ at \sqrt{s} between 62 and 540GeV.	139
5.6	Comparison of invariant cross section for prompt photon production at $\sqrt{s} = 200$ GeV with NLO pQCD calculations. The three curves represent NLO calculations with different scales of $0.5p_T$ (top), p_T (middle) and $2p_T$ (bottom).	140
5.7	The ratio of the obtained cross section for the prompt photon production to the cross section for π^0 . Black line represents statistical error. Color filled band represents systematic error.	141
A.1	The PHENIX coordinate system.	148
E.1	One arm of the PHENIX muon detector. Three stations of the tracking chambers are placed inside the muon magnet. Each station consists of eight octant cathode strip chambers [128].	164
E.2	Overview of the OASys. Seven OASys beams, from the light source, through the lens to the CCD camera, surround one octant chamber. There are $7 \times 8 = 56$ OASys beams in total for one muon arm. Relative straightness is measured from the focal image position on the CCD camera [128].	165
E.3	Sample of focal image on the CCD, for a typical sharp-focus channel. Sliced X- and Y-dimensional light intensity histograms are also shown beside the image. The solid curves are the results of Gaussian fitting. The “window cut” regions ignored by the Gaussian fittings are indicated as the gray regions around the peaks [128].	166
E.4	Sample of focal image on the CCD for a typical broad-focus channel. Because the raw CCD image is too weak for the focal image to be recognized, an intensified image is also shown at the bottom left corner. The sliced X- and Y-dimensional light intensity histograms show that the wide, weak peaks can be clearly identified. The window cut indicated by the gray region is indispensable because of its highly deformed peak shape [128].	167

E.5 Peak position distributions for the focal position resolution measurements: a) typical sharp-focus channel and b) typical broad-focus channel. One thousand events are taken for each channel. The width σ of the Gaussian-like peaks indicate the position determination resolution of 1.4 and 3.1 μm [128]. . . . 168

E.6 Time dependent motions of the relative focal positions are shown for a period of 18 days. Both horizontal and vertical directional focal positions are plotted with arbitrary position offsets. Room temperature measured near the chambers is also plotted [128]. 169

Chapter 1

Introduction

Elementary particles are the smallest pieces of the matter in the universe. In ancient Greece, Democritus who was a philosopher thought about the origin of the matter, and provided the idea that the matter was composed of “atom” which was regarded as undivide component of all the matter. Particle physics or high energy physics is one of the field of science to investigate such as elementary particles and the interaction of elementary particles. The development of science and technology gives us much more detailed information of the matter. The obtained picture by such as the development has changed the “unbreakable” constituent into the “breakable” constituent. In other words the elementary particle which was regarded as “unbreakable” constituent consists of smaller particles. Such a change of picture of the elementary particle was repeated in the history of science.

In 19th century, the atomic theory was introduced by J. Dalton. At that time, the atom was regarded as the elementary particle of the matter. In 1897, J. J. Thomson discovered a particle which had a negative charge and was lighter than atom by the cathode ray in the vacuum tube [1, 2]. It indicated that atom was not the elementary particle and had the structure with smaller constituents. That particle which was discovered J. J. Thomson was the electron. Now electron is known as the constituent of atom. The structure of atom was found by E. Rutherford in 1911 [3]. He discovered the nucleus in the center of atom using α -ray scattering with platinum. In addition, the neutron was discovered by J. Chadwick in 1932 [4]. It was found that the neutron was a constituent of the nucleus. Around that time, the particles which had been discovered, for example, proton and neutron, were thought as the elementary particles. The pion was predicted by H. Yukawa in 1935 at first as a mediator of the nuclear force [5], and then discovered by C. F. Powell in cosmic ray in 1947 [6]. Now that these particles are understood to have the structure of more smaller particles, too. Those particles are called

quark and lepton.

In the universe, it is known that there are four forces, which are called the gravity, electromagnetic, weak and strong, respectively. The strong interaction has a strength of about 100 times that of electromagnetic interaction. The weak interaction has a strength of about 1/1000 times that of electromagnetic interaction. The gravity is much smaller than the other interaction, therefore the gravity can be negligible in the world of elementary particles. The dominated force of macroscopic world is however gravity. The scale of distance of gravity is very huge, therefore the gravity can form the galaxies. The electromagnetic force combines the nucleus with electron and forms the atom, and also combines the atoms and forms the molecules, then combines the molecules and forms the matter. In the microscopic world, the electromagnetic force performs a decisive role. In further microscopic world like the nucleus, the strong force dominates. The nucleus which is formed by protons and neutrons is combined by the nuclear force. The nuclear force is a kind of the strong force by the color; the strong force works between the quarks and gluons.

The gravity and electromagnetic forces are the long distance force because the strength of forces decrease by the power of distance. On the other hand the strong and weak forces are the short distance force. The strong force reaches only the size of nucleus ($\sim 10^{-15}$ m). The distance of the weak force is smaller than that of the strong force ($\sim 10^{-18}$ m). The reason why the distance of the weak force is very short, is that the mediators of the weak force which are the W^\pm and Z^0 have a large mass (~ 90 GeV). The reason why the strong force is the short distance force is different from that of the weak force. The mediator of the strong force is the gluon which is massless particle. However, the strength of the strong force has two components, not only the component of decreasing by the power of distance but also the component of proportional to distance. The more quarks are separated, the more the potential energy is saved between two quarks. At some distance, it becomes easier to produce a pair of new quark and anti-quark rather than keeping the distance between the quarks against the increasing force. Therefore, the strong force decreases rapidly at some distance. That is the reason why the strong force is called the short distance force. Its origin is the color and this mechanism is called “color confinement” of quarks.

In order to understand the fundamental interactions, there are some theory for each of them. The strong force is described by Quantum Chromodynamics (QCD). It is known that the electromagnetic and the weak force are the different sides of the same force. The unified force is called the electroweak interaction. This force is described by Glashow-Weinberg-Salam theory [7, 8, 9, 10]. The QCD and Glashow-Weinberg-Salam theory are combined

and called the $SU(3) \times SU(2) \times U(1)$ Standard Model.

To investigate more microscopic world, the more higher energy beam of particle have been needed. The high energy beam which is accelerated with accelerator is collided with the target, and the scattered particles are detected with the various radiation detectors. The resolution of the accelerator as a “microscope” depends on the energy of incident beam, because the particle of incident beam has the de Broglie wave ($\lambda \sim \hbar/p$), where λ is the length of de Broglie wave, \hbar is the Plank’s constant divided by 2π and the p is the momentum of incident particle. Therefore, to resolve the phenomenon of the elementary particles, the highest energy accelerator is needed as a tool of the research. This is the reason why the “particle physics” is also called “high energy physics”.

The Relativistic Heavy Ion Collider (RHIC) [106] at Brookhaven National Laboratory can provide collisions of various ions from proton to gold. The RHIC is also operated as the first polarized proton-proton collider with energy range from 50 GeV to 250 GeV. The RHIC is designed to accelerate polarized protons up to 250 GeV and Au nuclei up to 100 GeV/nucleon. At such a high energy the proton beam can be regarded as a bundle of quarks and gluons. Therefore quark-quark, quark-gluon and gluon-gluon collisions take place, which are very useful for the study of QCD.

The Pioneering High Energy Nuclear Interaction eXperiment (PHENIX) detector has collected 56M events in proton-proton collisions at $\sqrt{s} = 200$ GeV using the high- p_T trigger. Data in Electro-Magnetic Calorimeter (EMCal) in PHENIX detector are mainly used in this thesis. The EMCAL consists of six sectors of lead scintillator calorimeter (PbSc) and two sectors of lead glass calorimeter (PbGl). It is located at a radial distance of approximately 5 m from the beam axis. Each of these sectors covers the pseudo-rapidity range of $|\eta| < 0.35$ and the azimuthal angle of $\phi = 0.4$ rad. The measurement of spin-averaged prompt photon cross section in proton-proton collisions is reported in this thesis. This is the prompt photon measurement at highest energy in the world in the proton-proton collisions. One aim is a test of perturbative Quantum ChromoDynamics (pQCD). The other is to provide the gluon distribution in the nucleon and a reference data for Quark Gluon Plasma (QGP) search in heavy ion collisions. This measurement is also the first step the determination of gluon spin contribution to the proton spin.

In chapter 2, the motivation and background for this work are introduced.

In Chapter 3, overview of the RHIC complex and PHENIX detector is presented. The description of the RHIC complex is in Section 3.1, and the PHENIX detector overview is in Section 3.2 to Section 3.8.

In Chapter 4, the analysis method is explained in detail. The Outline of this analysis is introduced in Section 4.1. It is very important to evaluate

the background signals, because there are many background sources for the prompt photon production. In Section 4.4 to Section 4.9, the subtraction of background and evaluation of background signals are discussed. In Section 4.10 to Section 4.13, the photon detection efficiency, trigger bias, and photon conversion loss are discussed. The calculation of cross section for prompt photon and evaluation of systematic errors are described in Section 4.14,

In Chapter 5, the results of the analysis are presented. The comparison with other experiments and with pQCD calculation are discussed.

In Chapter 6, the summary of in this thesis is described.

In Appendix A, the PHENIX coordinate system and frequently used kinematical variables are explained. The kinematics of π^0 decay is explained in Appendix B. The prompt photon cross section at leading order is explained in Appendix C. The prompt photon cross section from other experiments are listed in Appendix D. In Appendix E, my contribution to PHENIX Muon Tracker are described. My contribution is finding the dependence of temperature and magnetic field for PHENIX Muon Tracker.

Chapter 2

Theoretical Background

In this chapter, the motivation and background for the present work is introduced. One motivation is a test of perturbative Quantum ChromoDynamics (pQCD). The other is to provide the gluon distribution in the nucleon and a reference data for Quark Gluon Plasma (QGP) search in heavy ion collisions. The above motivations are described in Section 2.3 and Section 2.4.

2.1 Perturbative Quantum ChromoDynamics (pQCD)

2.1.1 Quarks and Leptons

The Quark model was introduced by M. Gell-Mann and G. Zweig in 1964 [11], [12], [13] to explain many discovered hadrons. Table 2.1, 2.2, 2.3, 2.4 [14] shows all fundamental particles in the Standard Model.

The strong interaction is an interaction which works between quarks and gluons. The idea of color quantum number was introduced to resolve conflict with Fermi statistics by M. Y. Han and Y. Nambu and also by O. W. Greenberg in 1965 [15] [16]. The short summary of discovery of the quarks and gluons can be described as follows. M. Gell-Mann and K. Nisijima introduced the strangeness as a new quantum number in 1953. The first discovery of the strange particle was in 1947 [17] in cosmic rays. Moreover, new particles with the strangeness were discovered using accelerators in 1950's, for example Cosmotron. The charm quark was discovered in 1974 [18] [19] as a bound state of the charm quark and anti-charm quark at Stanford Linear Accelerator Center (SLAC) and Alternating Gradient Synchrotron (AGS) in Brookhaven Notional Laboratory (BNL). The bottom quark was discovered in 1978 [20] as a bound state of the bottom quark and anti-bottom quark at

proton synchrotron in Fermi National Laboratory. The first evidence of gluon was reported in 1978 [21] at PETRA in DESY as a gluon jet. The top quark was discovered in 1994 [22] at TEVATRON in Fermi National Laboratory.

	u	d	s
Q	$\frac{1}{3}$	$-\frac{2}{3}$	$-\frac{1}{3}$
J	$\frac{1}{2}$	$\frac{1}{2}$	$\frac{1}{2}$
I_z	$\frac{1}{2}$	$-\frac{1}{2}$	0
B	$\frac{1}{3}$	$\frac{1}{3}$	$\frac{1}{3}$
S	0	0	-1
C	0	0	0
b	0	0	0
T	0	0	0
Mass (MeV)	1.5 ~ 4	4 ~ 8	80 ~ 130

Table 2.1: Summary of up, down, strange quarks. Q is the electric charge. J is the spin. I_z is the isospin. B is the baryon number. S is the strangeness. C is the charm quantum number. b is the bottom quantum number. T is the top quantum number [14].

2.1.2 The QCD Lagrangian

Quantum Chromodynamics (QCD) is the gauge field theory which describes the strong interactions of colored quarks and gluons. That theory is one of the components of the Standard Model. The quarks have a specific flavor (See Section 2.1.1) and one color of the three, red, green, and blue. The gluons have a color of the eight. The hadrons are the state which is color singlet of quarks, anti-quarks, and gluons. The QCD Lagrangian is described as follows:

$$L_{QCD} = -\frac{1}{4}F_{\mu\nu}^{(a)}F^{(a)\mu\nu} + i\sum_q\bar{\phi}_q^i\gamma^\mu(D_\mu)_{ij}\phi_q^j - \sum_q m_q\bar{\phi}_q^i\phi_{qi}, \quad (2.1)$$

$$F_{\mu\nu}^{(a)} = \partial_\mu A_\nu^a - \partial_\nu A_\mu^a - g_s f_{abc}A_\mu^b A_\nu^c, \quad (2.2)$$

$$(D_\mu)_{ij} = \delta_{ij}\partial_\mu + ig_s\sum_a\frac{\lambda_{ij}^a}{2}A_\mu^a, \quad (2.3)$$

	c	b	t
Q	$+\frac{2}{3}$	$-\frac{1}{3}$	$+\frac{2}{3}$
J	$\frac{1}{2}$	$\frac{1}{2}$	$\frac{1}{2}$
I_z	0	0	0
B	$\frac{1}{3}$	$\frac{1}{3}$	$\frac{1}{3}$
S	0	0	0
C	+1	0	0
b	0	-1	0
T	0	0	+1
Mass(GeV)	1.15 ~ 1.35	4.1 ~ 4.4 (\bar{M} S mass) 4.6 ~ 4.9 (1S mass)	174.3 ± 5.1 (direct observation of top events) $178.1^{+10.4}_{-8.3}$ (Standard Model electroweak fit)

Table 2.2: Summary of charm, bottom, top quarks [14].

where the $\phi_q^i(x)$ are the 4-component Dirac spinors associated with the field of the each quark of color i and flavor q . The $A_\mu^a(x)$ are the gluon (Yang-Mills) fields. The g_s is the QCD coupling constant, and the f_{abc} are the structure constants of the $SU(3)$ algebra. The Feynman rules are derived from this Lagrangian and can be found in [23].

2.1.3 Asymptotic Freedom and Confinement

The QCD describes the strong interaction successfully, which is characterized by the two features. One is the asymptotic freedom [24] [25], the other is the confinement. The renormalization scale dependence of the effective QCD coupling constant $\alpha_s = g_s^2/4\pi$ is controlled by β -function as follows:

$$\begin{aligned} \mu \frac{\partial \alpha_s}{\partial \mu} &= 2\beta(\alpha_s) = -\frac{\beta_0}{2\pi} \alpha_s^2 - \frac{\beta_1}{4\pi^2} \alpha_s^3 - \frac{\beta_2}{64\pi^3} \alpha_s^4 - \dots, \\ \beta_0 &= 11 - \frac{2}{3} n_f, \end{aligned} \quad (2.4)$$

	e	ν_e	μ	ν_μ	τ	ν_τ
Q	-1	0	-1	0	-1	0
J	$\frac{1}{2}$	$\frac{1}{2}$	$\frac{1}{2}$	$\frac{1}{2}$	$\frac{1}{2}$	$\frac{1}{2}$
T_3	$-\frac{1}{2}$	$\frac{1}{2}$	$-\frac{1}{2}$	$\frac{1}{2}$	$-\frac{1}{2}$	$\frac{1}{2}$
Le	+1	+1	0	0	0	0
$L\mu$	0	0	+1	+1	0	0
$L\tau$	0	0	0	0	+1	+1
Mass(MeV)	0.511	$< 3 \times 10^{-6}$	105.66	< 0.19	1776.99	< 18.2

Table 2.3: Summary of leptons. T_3 is the third component of weak isospin. Le, μ, τ is the electron, muon, τ lepton numbers, respectively [14].

	γ	W^+	W^-	Z	$g_i(i = 1\dots 8)$
Q	0	+1	-1	0	0
J	1	1	1	1	1
Mass(GeV)	0	80.43	80.43	91.19	0

Table 2.4: Summary of gauge bosons [14].

$$\begin{aligned}\beta_1 &= 51 - \frac{19}{3}n_f, \\ \beta_2 &= 2857 - \frac{5033}{9}n_f + \frac{325}{27}n_f^2,\end{aligned}$$

where μ is a renormalization scale, n_f is the number of quark flavor, g_s is the color charge. The solution of Equation 2.5 is expressed as an expansion in inverse powers of $\ln(\mu^2)$ as follows:

$$\begin{aligned}\alpha_s &= \frac{4\pi}{\beta_0 \ln(\mu^2/\Lambda^2)} \left[1 - \frac{2\beta_1}{\beta_0^2} \frac{\ln[\ln(\mu^2/\Lambda^2)]}{\ln(\mu^2/\Lambda^2)} \right. \\ &\quad \left. + \frac{4\beta_1^2}{\beta_0^4 \ln^2(\mu^2/\Lambda^2)} \left(\left(\ln[\ln(\mu^2/\Lambda^2)] - \frac{1}{2} \right)^2 + \frac{\beta_2\beta_0}{8\beta_1^2} - \frac{5}{4} \right) \right], \quad (2.5)\end{aligned}$$

where Λ is the scale parameter in QCD. It is clear that the Equation 2.5 approaches to 0 when μ^2 increases to infinity. Figure 2.1 clearly shows the

decrease in $\alpha_s(\mu)$ with increasing μ . This means that when two quarks are close to each other, the strong force is relatively weak. On the other hand, when two quarks move farther apart the force becomes stronger. At some distance, it becomes easier to produce a pair of new quark and anti-quark rather than keeping the distance between the quarks against the increasing force. The created quark and anti-quark form a hadron. The weakness of interaction at short distance is called 'asymptotic freedom', while the strength of the long distance is called 'confinement'. Because of the asymptotic freedom, the QCD quantity (for example, cross section σ) can be calculated using perturbation method as follows:

$$\sigma = c_1\alpha_s + c_2\alpha_s^2 + c_3\alpha_s^3 + \dots, \quad (2.6)$$

where $c_i, (i = 1, 2, \dots)$ come from calculating the appropriate Feynman diagrams. Such a method is called perturbative Quantum ChromoDynamics (pQCD). The pQCD is applied to calculate the QCD quantity when μ^2 is more than 1 GeV^2 . Due to the confinement, a quark cannot be extracted from hadrons.

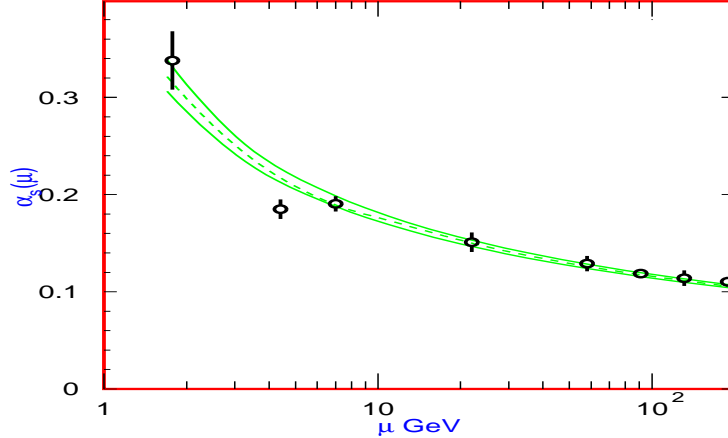


Figure 2.1: Summary of the values of α_s as a function of μ . The lines show the central values and the $\pm 1\sigma$ limits of our average [14].

2.1.4 pQCD in Hadron Collisions

The high-energy hadron interaction is described by the parton model improved by QCD. In this model a hard scattering process of the two hadrons is represented as an interaction of the quarks and gluons which are the constituents of the incoming hadrons.

The cross section for a hard scattering process, for example the production of a hadron h ($pp \rightarrow hX$), can be written as follows,

$$\begin{aligned} \frac{d\sigma^{pp \rightarrow hX}}{dP} &= \sum_{f_1, f_2, f} \int dx_1 dx_2 dz f_1^p(x_1, \mu^2) f_2^p(x_2, \mu^2) \\ &\times \frac{d\hat{\sigma}^{f_1 f_2 \rightarrow f X'}}{dP}(x_1 p_1, x_2 p_2, p_h, \mu) \times D_f^h(z, \mu^2). \end{aligned} \quad (2.7)$$

Here P means any appropriate set of the kinematic variables of the reaction. $f_i^p(x_i, \mu^2)$ represents the probability density for finding a parton type f_i in the proton (parton distribution function)(See Section 2.1.5). x is a fraction of the parton's momentum in the proton's momentum and μ is the factorization scale. The $\hat{\sigma}^{f_1 f_2 \rightarrow f X'}$ are the base of hard process cross section for f_1 and f_2 which are initial partons producing f which are a final state parton and unobserved parton X' . p_1 and p_2 are the momenta of initial protons. $D_f^h(z, \mu^2)$ is the probability density for finding a h with fraction of momentum z in the final state parton f (fragmentation function) (See Section 2.1.6).

The picture of the QCD improved parton model as used in Equation 2.7 consists of three parts; one is a parton distribution function f_i^p , another is a subprocess cross section $d\hat{\sigma}^{f_1 f_2 \rightarrow f X'}$, the other is a fragmentation function D_f^h . The parton distribution function and fragmentation function represent intrinsic constituents of the proton and the hadronization mechanism, respectively. They cannot be calculated from the first principles in QCD at present. On the other hand, the subprocess cross section $\hat{\sigma}^{f_1 f_2 \rightarrow f X'}$ can be calculated by pQCD as perturbation series in the strong coupling constant α_s . Table 2.5 shows the parton-parton two body scattering differential cross sections. The cross section is required to satisfy in the following condition,

$$\mu \frac{d\sigma^{pp \rightarrow hX}}{d\mu} = 0, \quad (2.8)$$

because the cross section must be independent of the arbitrary scale. The several theoretical publications discuss the optimization of the scale [26],

2.1.5 Parton Distribution Function (PDF)

The parton distribution function is the probability density for finding a type of parton in the proton. The proton structure function $F_2(x, Q^2)$ is measured

Subprocess	Cross section
$qq' \rightarrow qq'$	$\frac{4}{9} \frac{s^2+u^2}{t^2}$
$qq \rightarrow qq$	$\frac{4}{9} \left[\frac{s^2+u^2}{t^2} + \frac{s^2+t^2}{u^2} \right] - \frac{8}{27} \frac{s^2}{tu}$
$q\bar{q} \rightarrow q'\bar{q}'$	$\frac{4}{9} \frac{t^2+u^2}{s^2}$
$q\bar{q} \rightarrow q\bar{q}$	$\frac{4}{9} \left[\frac{s^2+u^2}{t^2} + \frac{u^2+t^2}{s^2} \right] - \frac{8}{27} \frac{u^2}{st}$
$gq \rightarrow gq$	$-\frac{4}{9} \left[\frac{s}{u} + \frac{u}{s} \right] + \frac{s^2+u^2}{t^2}$
$q\bar{q} \rightarrow gg$	$\frac{32}{27} \left[\frac{t}{u} + \frac{u}{t} \right] - \frac{8}{3} \frac{t^2+u^2}{s^2}$
$gg \rightarrow q\bar{q}$	$\frac{1}{6} \left[\frac{t}{u} + \frac{u}{t} \right] - \frac{3}{8} \frac{t^2+u^2}{s^2}$
$gg \rightarrow gg$	$\frac{9}{2} \left[3 - \frac{tu}{s^2} - \frac{su}{t^2} - \frac{st}{u^2} \right]$
$gq \rightarrow \gamma q$	$-\frac{e_q^2}{3} \left[\frac{u}{s} + \frac{s}{u} \right]$
$q\bar{q} \rightarrow \gamma g$	$\frac{8}{9} e_q^2 \left[\frac{u}{t} + \frac{t}{u} \right]$
$q\bar{q} \rightarrow \gamma\gamma$	$\frac{2}{3} e_q^4 \left[\frac{t}{u} + \frac{u}{t} \right]$
$gg \rightarrow \gamma\gamma$	$\left[\sum_{i=1}^{nf} e_q^2 \right]^2 \frac{\alpha_s^2}{8\pi^2} \left[\frac{1}{8} \left[\frac{s^2+t^2}{u^2} \ln^2 \left[-\frac{s}{u} \right] + 2 \frac{s-t}{u} \ln \left[-\frac{s}{t} \right] \right]^2 \right.$ $+ \left[\frac{s^2+u^2}{t^2} \ln^2 \left[-\frac{s}{u} \right] + 2 \frac{s-u}{t} \ln \left[-\frac{s}{u} \right] \right]^2 + \left[\frac{t^2+u^2}{s^2} \left[\ln^2 \frac{t}{u} + \pi^2 \right] + 2 \frac{t-u}{s} \ln \frac{t}{u} \right]^2$ $\times \frac{1}{2} \left[\frac{s^2+t^2}{u^2} \ln^2 \left[-\frac{s}{t} \right] + 2 \frac{s-t}{u} \ln \left[-\frac{s}{t} \right] + \frac{s^2+u^2}{t^2} \ln^2 \left[-\frac{s}{u} \right] + 2 \frac{s-u}{t} \ln \left[-\frac{s}{u} \right] \right.$ $\left. + \frac{t^2+u^2}{s^2} \left[\ln^2 \frac{t}{u} + \pi^2 \right] + 2 \frac{t-u}{s} \ln \frac{t}{u} \right]$ $+ \frac{\pi^2}{2} \left[\left[\frac{s^2+t^2}{u^2} \ln \left[-\frac{s}{t} \right] + \frac{s-t}{u} \right]^2 + \left[\frac{s^2+u^2}{t^2} \ln \left[-\frac{s}{u} \right] + \frac{s-u}{t} \right]^2 \right] + 4$

Table 2.5: The parton-parton two body scattering differential cross sections. Factors of $\pi\alpha_s^2/s^2$, $\pi\alpha\alpha_s/s^2$ and $\pi\alpha^2/s^2$ have been factored out of the purely strong interaction, the single photon production and the double photon production processes, respectively. The e_q is the electric charge of quark. The s , t and u are the Mandelstam variables [75].

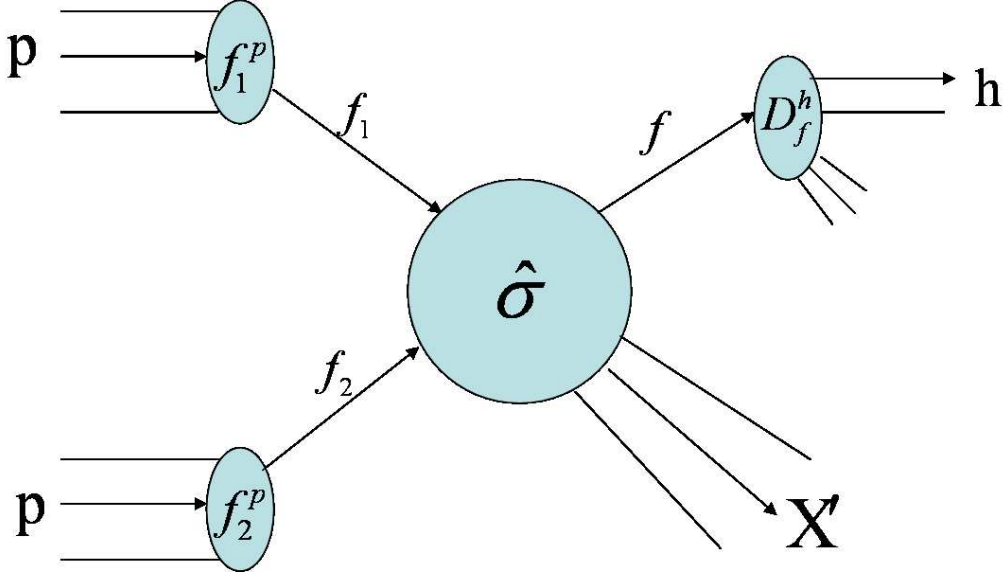


Figure 2.2: Production of a high p_T hadron h in a hard scattering process.

by ZEUS [31] and H1 [32] at Deutsches Elektronen Synchrotron (DESY) and Stanford Linear Accelerator (SLAC) [33] experiments using the electron-proton scattering, by EMC [34], NMC [35], BCDMS [36] and E665 [37] at FNAL using the muon-proton scattering. $F_2(x, Q^2)$ can be written as follows;

$$F_2(x, Q^2) = x \cdot \sum_f e_f^2 (q_f(x, Q^2) + \bar{q}_f(x, Q^2)) \quad (2.9)$$

where x is Bjorken x , f is the quark flavor, e_f is the charge of the quark and anti-quark and $q_f(x, Q^2)$ and $\bar{q}_f(x, Q^2)$ is the quark and anti-quark distribution function. The Q^2 dependence of parton distribution functions can be calculated with DGLAP equation [27, 28, 29, 30] as follows;

$$t \frac{\partial}{\partial t} \begin{pmatrix} q_i(x, t) \\ g(x, t) \end{pmatrix} = \frac{\alpha_s}{2\pi} \sum_{q_j, \bar{q}_j} \int_x^1 \frac{dy}{y} \quad (2.10)$$

$$\times \begin{pmatrix} P_{q_i q_j}(\frac{x}{y}, \alpha_s(t)) & P_{q_i g}(\frac{x}{y}, \alpha_s(t)) \\ P_{g q_j}(\frac{x}{y}, \alpha_s(t)) & P_{g g}(\frac{x}{y}, \alpha_s(t)) \end{pmatrix} \begin{pmatrix} q_j(y, t) \\ g(y, t) \end{pmatrix} \quad (2.11)$$

where $P_{ab}(\frac{x}{y}, \alpha_s(t))$ represents the probability of finding a parton type a in a parton of type b with a fraction $\frac{x}{y}$ of the longitudinal momentum of the parent parton. t is defined as μ^2 . Figure 2.3 [14] shows $F_2(x, Q^2)$ measured by H1, ZEUS, BCDMS, E665, NMC and SLAC as a function of Q^2 .

The ratio of \bar{d} to \bar{u} is measured by NMC. NMC found a violation of Gottfried sum rule. The ratio of \bar{d} to \bar{u} is measured from Drell-Yan process in proton-proton collisions and proton-nuclear collisions by NA51 [38] and E866 [39]. The ratio of d to u is measured from the process of $W^\pm \rightarrow l^\pm \nu$ by CDF [40]. The gluon density is given by the inclusive jet production [41] [42] and prompt photon production [43].

The parton distribution function is tried to be extracted from many experimental results by several theoretical groups [44] [45, 46] [47] [48]. The global analysis including systematic error estimation and next-to-next-to-leading-order (NNLO) global analysis are performed. An example of the parton distribution function is shown in Figure 2.4 [14].

2.1.6 Fragmentation Function (FF)

The fragmentation function ($D_f^h(z, \mu^2)$) indicates the probability density for finding a hadron h with the fraction of momentum z when f is the scattered parton. The fragmentation function satisfies the sum rule as follows;

$$\sum_h \int z D_f^h(z, \mu^2) dz = 1 \quad (2.12)$$

The fragmentation function is measured by ALEPH [59, 66], OPAL [60, 61, 62, 63, 68], DELPHI [65] and L3 [67] at CERN, HRS [56], MARKII [57, 69] and TPC [64] at SLAC, TASSO [54, 55] at DESY, AMY [58] at KEK in e^+e^- collisions using the $e^+ + e^- \rightarrow \gamma$ or $Z \rightarrow h + X$ process. An example of the fragmentation function in e^+e^- collisions for all charged particles is shown Figure 2.5 [14].

The scale dependence of parton fragmentation function can be calculated with DGLAP equation like the parton distribution function as follows;

$$t \frac{\partial}{\partial t} D_i(x, t) = \sum_j \int_x^1 \frac{dz}{z} \frac{\alpha_s}{2\pi} P_{ji}(z, \alpha_s) D_j\left(\frac{x}{z}, t\right). \quad (2.13)$$

where t is defined as μ^2 .

The pQCD theoretical calculations for hadrons [70], [71], [72], [73] and photons [74] at next-to-leading-order (NLO) are performed.

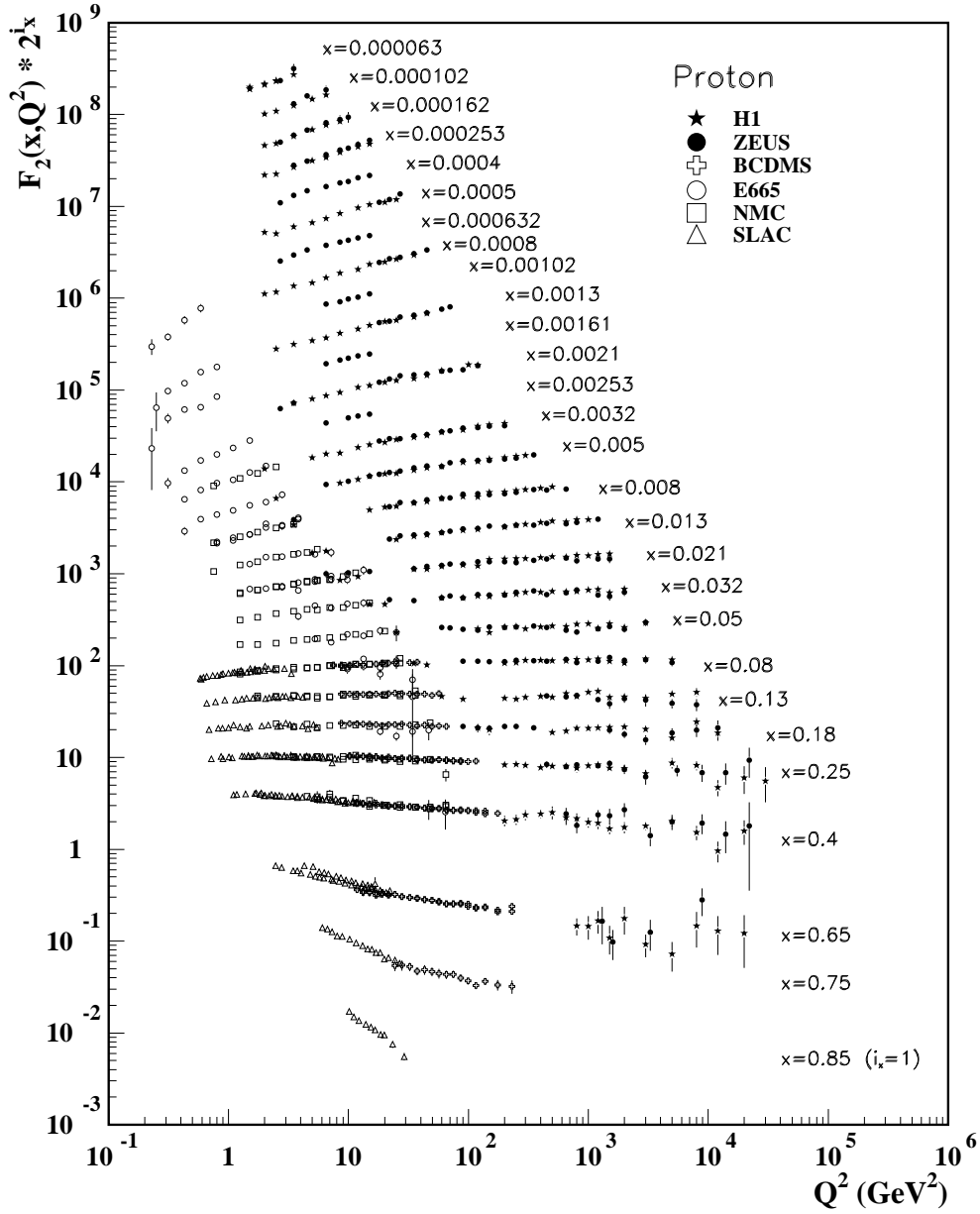


Figure 2.3: An example of the proton structure function $F_2(x, Q^2)$ measured by H1, ZEUS, BCDMS, E665, NMC and SLAC [14].

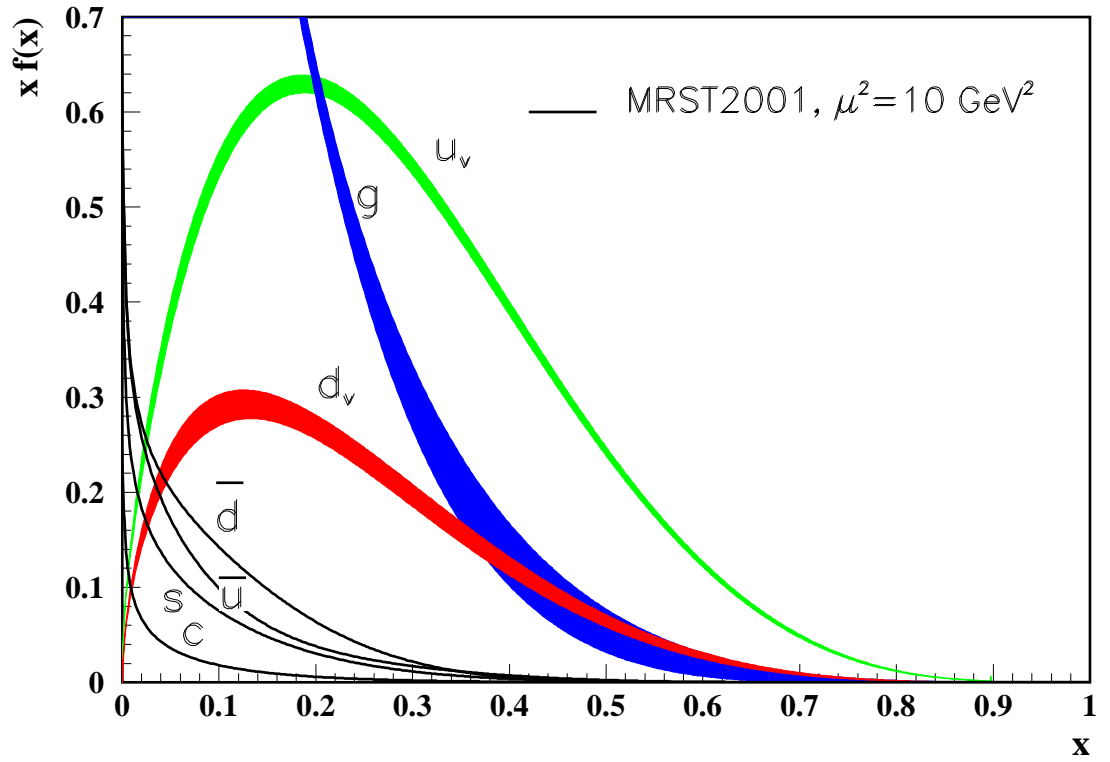


Figure 2.4: The distribution of the unpolarized parton density as a function of x using the MRST2001 parameterization at a scale $\mu^2 = 10 \text{ GeV}^2$ [14].

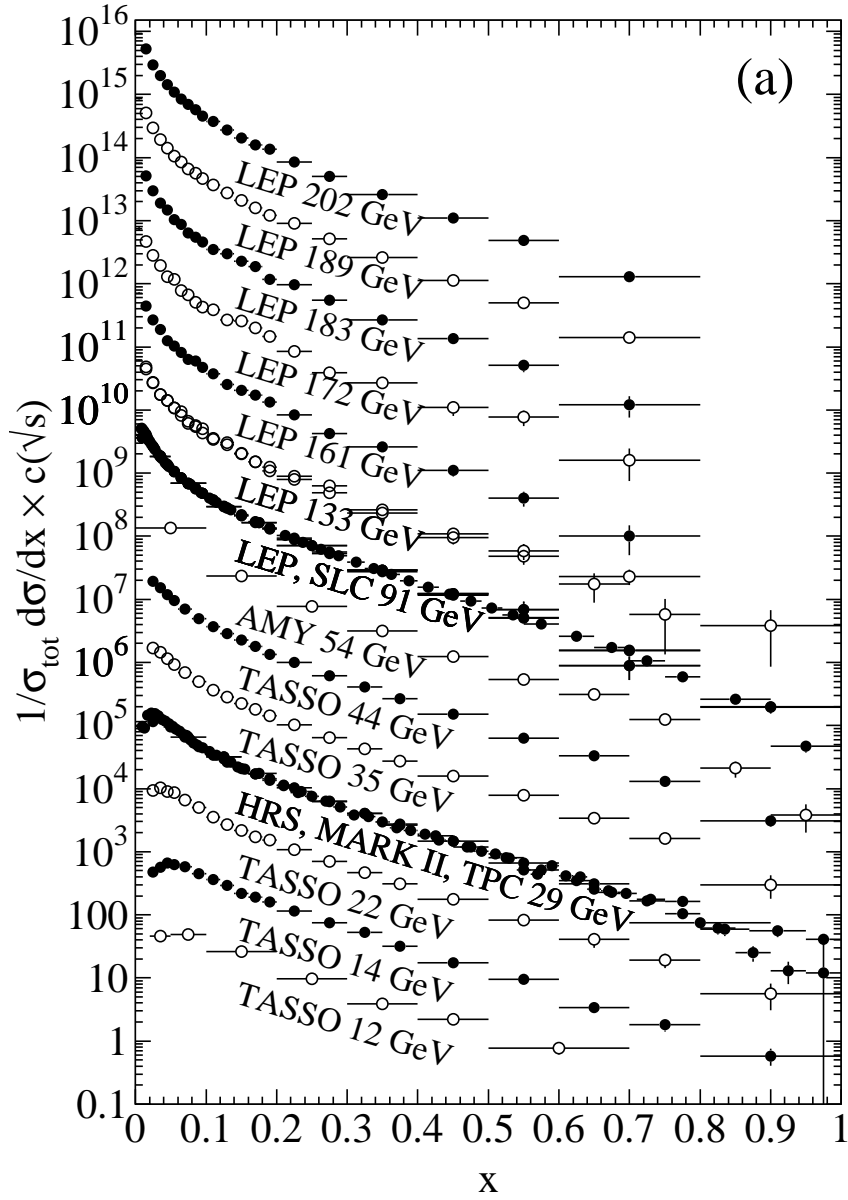


Figure 2.5: The fragmentation functions expressed by the total charged particle production cross sections obtained in the e^+e^- collisions are shown as a function of x , where $x = (2E_h/\sqrt{s})$ is the scaled hadron energy [14].

2.2 Prompt Photon Production

2.2.1 Prompt Photon Production in pQCD

The sketch of photon productions are shown in Figure 2.6 and 2.7. The photon produced by quark gluon Compton process, quark anti-quark annihilation process and fragmentation process are defined as prompt photon. However, the photon from hadron decay is not defined as prompt photon. Therefore, for example, the photon from π^0 decay is not prompt photon.

The measurement of the high transverse momentum prompt photon production is one of tests of the pQCD, and it gives us the gluon distribution in the nucleon. The high transverse momentum prompt photon production is closely related with high transverse momentum jet production. Here, transverse momentum is defined as follows:

$$p_T = p \sin \theta, \quad (2.14)$$

where θ is the angle from Z-axis, and p is the momentum of the photon or hadron. The coordinate system is explained in Appendix A. However, the study of prompt photon production has several advantages compared to the study of jet from the experimental points of view. The prompt photon is detected with an electromagnetic calorimeter, while the jet requires both electromagnetic and hadronic calorimeter. The energy resolution of electromagnetic calorimeters is generally better than that of hadronic calorimeters. Therefore systematic errors in the photon energy scale are smaller. Moreover, the prompt photon does not fragment like a jet. Energy and direction of the prompt photon are directly measured in the calorimeter without a jet algorithm to reconstruct a jet axis. On the other hand, the prompt photon production has relatively low event rate compared with the jet production, and many background sources from the jet production are not negligible. Therefore, it is important to subtract and evaluate the background for the prompt photon production in detail.

There are two processes for the prompt photon production at leading-order (LO). One is the quark gluon Compton process $gq \rightarrow \gamma q$ (Figure 2.8(a)), the other is the annihilation process $q\bar{q} \rightarrow \gamma g$ (Figure 2.9(b)). The differential cross section for prompt photon production $gq \rightarrow \gamma q$ and $q\bar{q} \rightarrow \gamma g$ can be written, respectively as;

$$-\frac{1}{3}e_q^2 \left(\frac{u}{s} + \frac{s}{u} \right) \quad (gq \rightarrow \gamma q), \quad (2.15)$$

and

$$\frac{8}{9}e_q^2 \left(\frac{u}{t} + \frac{t}{u} \right) \quad (q\bar{q} \rightarrow \gamma g), \quad (2.16)$$

where e_q is the electric charge of the quark, s , t , and u are Mandelstam variables (Appendix C). The color and spin indices are averaged (summed) over the initial (final) states. A detailed review can be found in [75]. In hadron-hadron collisions, the cross section depends on \sqrt{s} and p_T . For prompt photons produced with $\eta \approx 0$ (Appendix A) in the colliding hadrons center of mass frame, the initial state partons are probed at

$$x \sim x_T = 2p_T/\sqrt{s}. \quad (2.17)$$

This can be understood as follows. The proton beam energy is $\sqrt{s}/2$. In the case of the two colliding partons with the same x , the momentum of each parton is $x\sqrt{s}/2$ which should be equal to p . In the central rapidity ($\eta \approx 0$), $p \sim p_T = x_T\sqrt{s}/2$. Therefore, $x_T = 2p_T/\sqrt{s}$.

As shown in Figure 2.4, the gluon density is much larger than the quark and anti-quark density at small x , while at medium and large x the quark density is larger than the gluon density, and anti-quark density is much smaller than the gluon density. Therefore, the prompt photon production in proton-proton collisions is mainly due to the quark gluon Compton scattering process for all p_T range, while the prompt photon production in proton-anti-proton collisions is due to the quark gluon Compton scattering process at low p_T and the quark anti-quark annihilation process at high p_T . This suggests that the prompt photon production is a useful tool for extraction of gluon distribution function. Figure 2.10 shows the ratio of the quark gluon Compton scattering process to the quark anti-quark annihilation process in pp collisions at $\sqrt{s} = 200$ GeV. The quark gluon Compton scattering process dominates the quark anti-quark annihilation process for all p_T range. Figure 2.11 shows such a ratio in $p\bar{p}$ collisions at $\sqrt{s} = 200$ GeV. Figure 2.12 shows such a ratio in $p\bar{p}$ collisions at $\sqrt{s} = 1800$ GeV. This energy is the highest in the world in $p\bar{p}$ collisions. In low p_T region, the quark gluon Compton scattering process dominates, while quark anti-quark annihilation process dominates in high p_T region. Figure 2.13, 2.14, 2.15 show such a ratio as a function of x_T . The ratio of the quark gluon Compton scattering process to the quark anti-quark annihilation process is so different, if the beam type is different. Therefore, it is important for the measurement of prompt photon in pp collisions at $\sqrt{s} = 200$ GeV.

As mentioned above, the prompt photons are produced through the two processes which are the quark gluon Compton scattering process ($gq \rightarrow \gamma q$) and the quark anti-quark annihilation process ($q\bar{q} \rightarrow \gamma g$). However, the possibility of bremsstrahlung from the partons must also be considered. Such a case is included in fragmentation process. The photon fragmentation func-

tions from partons can be calculated by QED as follows [75];

$$zD_{\gamma/q_i}(z, Q^2) = e_{q_i}^2 \frac{\alpha_s}{2\pi} [1 + (1-z)^2] \ln(Q^2/\Lambda^2), \quad (2.18)$$

and

$$zD_{\gamma/g}(z, Q^2) = 0. \quad (2.19)$$

where z is the fraction of the parent parton's momentum, Λ is the scale parameter in QCD. e_{q_i} is the charge of the i th quark. The photon fragmentation function increases uniformly with the scale Q^2 over the whole z range. The photon fragmentation functions evolve with Q^2 as a result of $q\bar{q}$ pair production and gluon bremsstrahlung. The further description is found in [75]. Figure 2.16 shows the fraction of the direct process and the fragmentation process. The fragmentation process contributes substantially at low p_T region and the direct process is more than the fragmentation process at high p_T region.

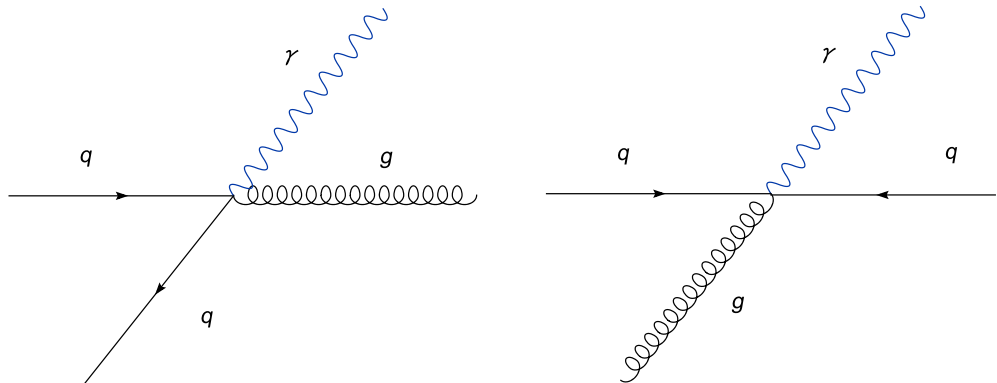


Figure 2.6: A sketch of prompt photon production for quark gluon Compton scattering process (left) and quark anti-quark annihilation process (right).

2.2.2 Overview of Experiments

The measurement of prompt photon in proton-proton collisions was performed by E706 [76] at Tevatron, E704 [79] at FNAL, UA6 [77, 78], WA70 [81], NA24 [82] at SPS, R110 [80], R806 [83] at ISR. The measurement of prompt photon in proton-anti-proton collisions was performed by UA6 [77, 78] at SPS, UA1 [84], UA2 [85] at $Spp\bar{p}S$, CDF [86], D0 [87] at Tevatron. A summary of measurements of prompt photon by these experiments is listed in table 2.6.

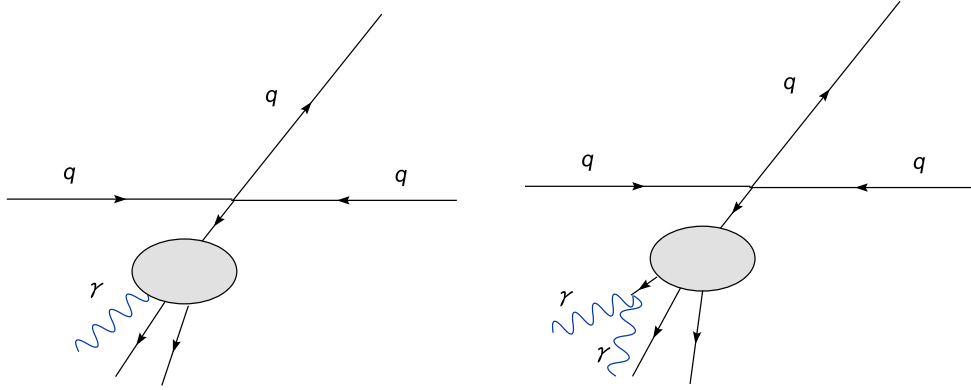


Figure 2.7: A sketch of prompt photon production for fragmentation process (left). A sketch of photon production from hadron decay (right).

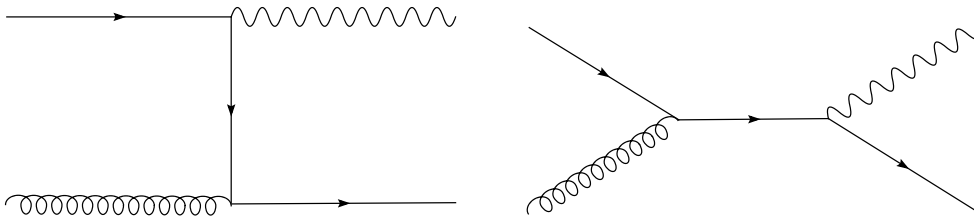


Figure 2.8: The diagrams of prompt photon production at leading-order for quark gluon Compton scattering process.

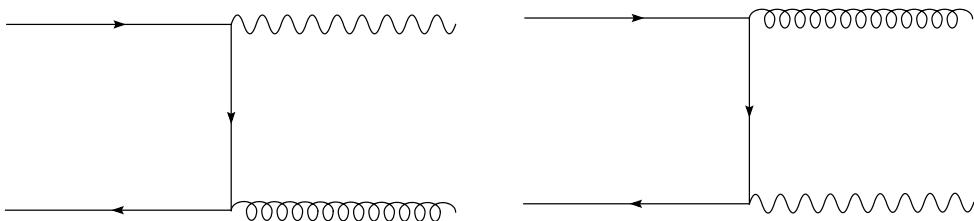


Figure 2.9: The diagrams of prompt photon production at leading-order for quark anti-quark annihilation process.

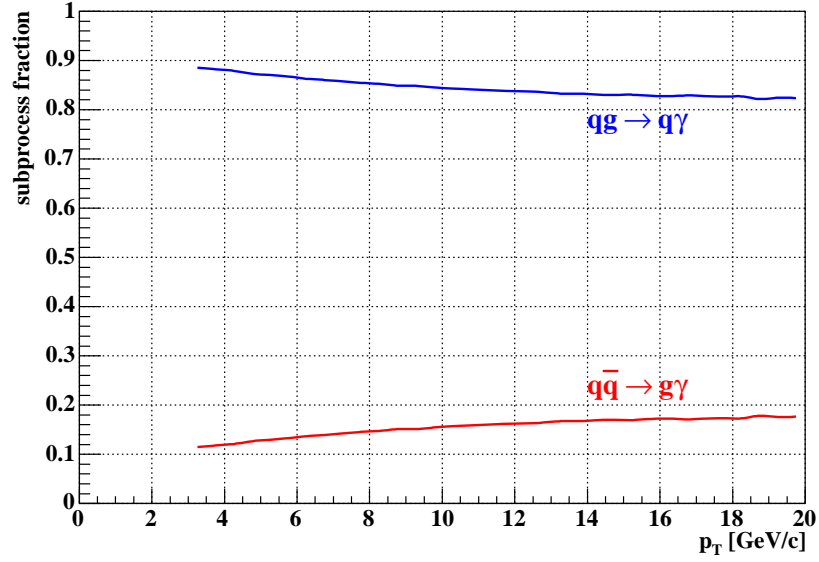


Figure 2.10: The fraction of $qg \rightarrow \gamma q$ and $q\bar{q} \rightarrow \gamma g$ as function of p_T in $p + p$ at $\sqrt{s} = 200\text{GeV}$.

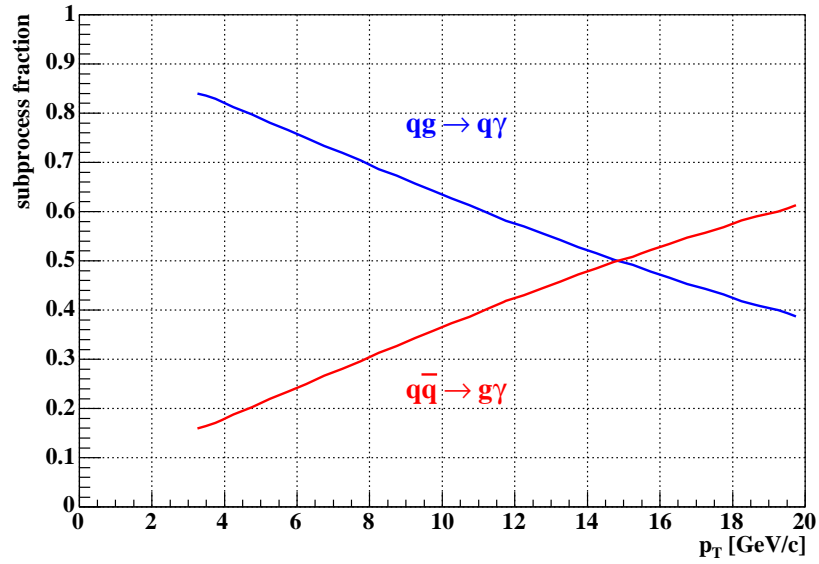


Figure 2.11: The fraction of $qg \rightarrow \gamma q$ and $q\bar{q} \rightarrow \gamma g$ as function of p_T in $p + \bar{p}$ at $\sqrt{s} = 200\text{GeV}$.

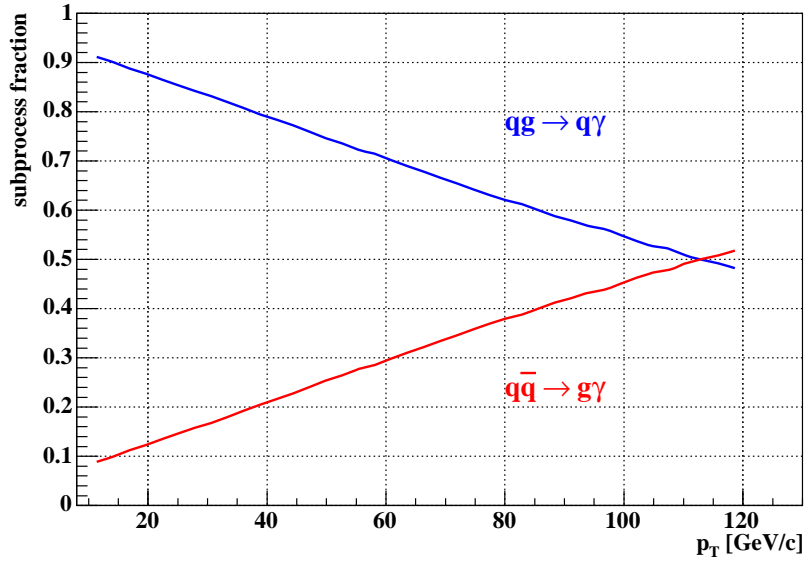


Figure 2.12: The fraction of $qq \rightarrow \gamma q$ and $q\bar{q} \rightarrow \gamma g$ as function of p_T in $p + \bar{p}$ at $\sqrt{s} = 1800\text{GeV}$.

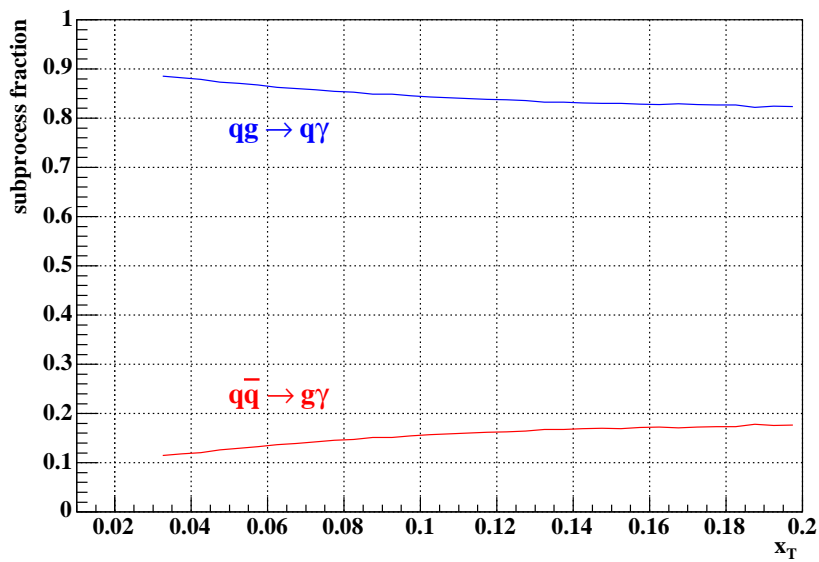


Figure 2.13: The fraction of $qq \rightarrow \gamma q$ and $q\bar{q} \rightarrow \gamma g$ as function of x_T in $p + p$ at $\sqrt{s} = 200\text{GeV}$.

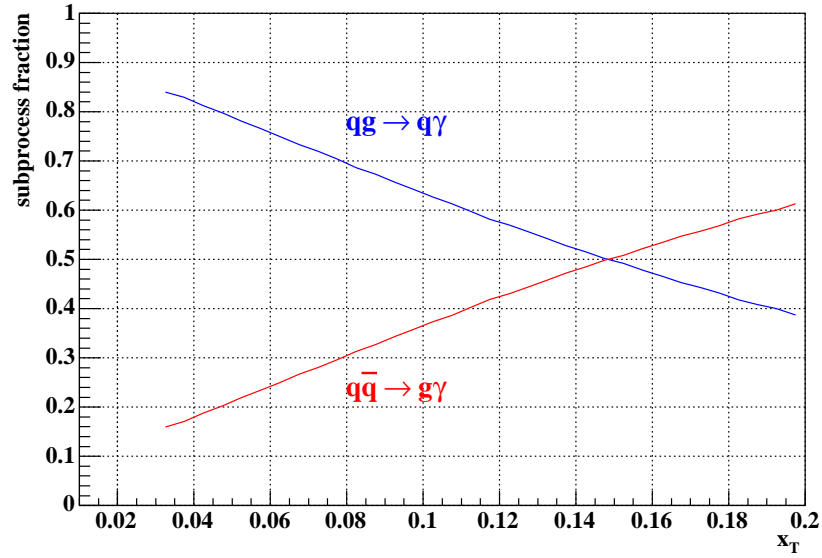


Figure 2.14: The fraction of $qg \rightarrow \gamma q$ and $q\bar{q} \rightarrow \gamma g$ as function of x_T in $p + \bar{p}$ at $\sqrt{s} = 200\text{GeV}$.

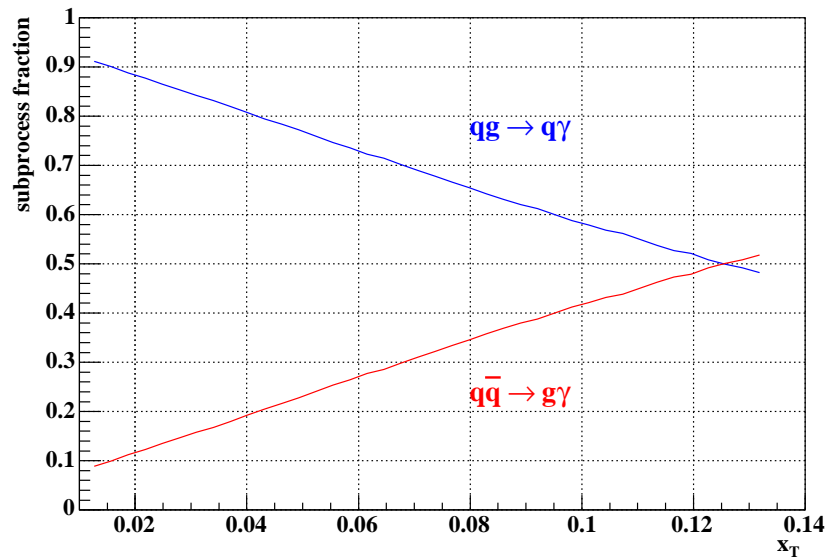


Figure 2.15: The fraction of $qg \rightarrow \gamma q$ and $q\bar{q} \rightarrow \gamma g$ as function of x_T in $p + \bar{p}$ at $\sqrt{s} = 1800\text{GeV}$.

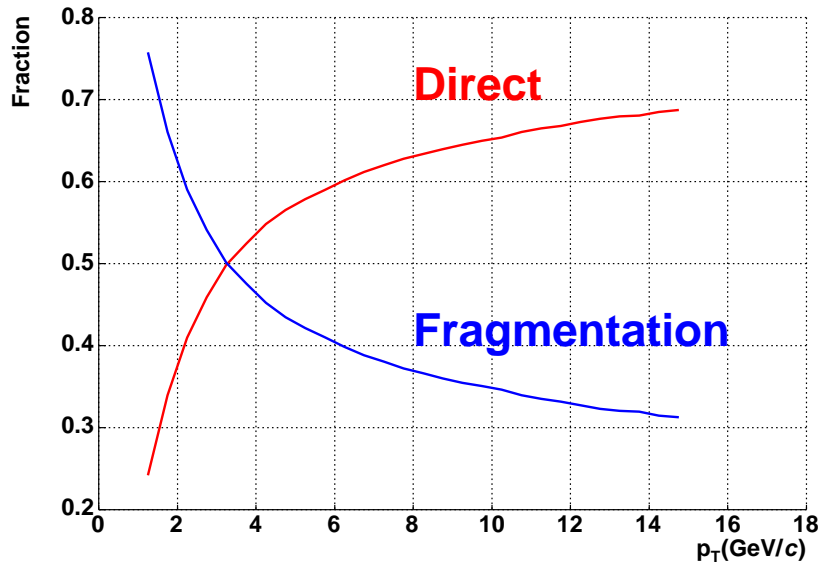


Figure 2.16: The ratio of direct process to fragmentation process as a function of photon p_T .

2.3 Spin Physics

2.3.1 Nuclear Spin Problem

It had been believed that the proton spin is carried by the quark spin. The spin dependent structure function measurements started at SLAC by E80 [88] and E130 [89]. In 1988, the European Muon Collaboration (EMC) measured spin dependent structure function with higher statistics and in a wider kinematic range, and reported that the contribution of quark spin for proton spin is only $12 \pm 9 \pm 14\%$ [90, 91]. This result is called “Nuclear Spin Problem”. Later, E142 [92], E143 [93], E154 [94] and E155 [95] at SLAC, SMC [96] at CERN and HERMES [97, 98] at DESY measured the contribution of quark spin for proton and neutron spin and reported consistent results with EMC. The proton spin can be written as follows;

$$\frac{1}{2} = \frac{1}{2}\Delta\Sigma + \Delta G + L_q + L_g \quad (2.20)$$

where $\Delta\Sigma$ and ΔG are quark and gluon contribution spin to the proton spin and L_q and L_g are the orbital angular momentum of quarks and gluons, respectively.

Accelerators	Collisions	Experiments	Pub. Year	\sqrt{s} [GeV]	p_T [GeV/c]
Tevatron	Fixed p	E706	2004	38.7	3.5-12.0
Tevatron	Fixed p	E706	2004	31.6	3.5-12.0
SPS	$p + p$	UA6	1998	24.3	4.1-7.7
SPS	$p + \bar{p}$	UA6	1998	24.3	4.1-7.7
FNAL	Fixed p	E704	1995	19.4	2.5-3.8
ISR	$p + p$	R110	1989	63	4.5-10.0
SPS	$p + p$	WA70	1988	22.9	4.11-5.70
SPS	$p + p$	NA24	1987	23.8	3.25-6.00
ISR	$p + p$	R806	1989	63	4.75-10.36
$Spp\bar{S}$	$p + \bar{p}$	UA1	1988	546	17-46
$Spp\bar{S}$	$p + \bar{p}$	UA1	1988	630	17-90
$Spp\bar{S}$	$p + \bar{p}$	UA2	1992	630	15.9-82.3
Tevatron	$p + \bar{p}$	CDF	1995	1800	12.3-114.7
Tevatron	$p + \bar{p}$	D0	1996	1800	10.5-72.0

Table 2.6: Measurements of prompt photon.

2.3.2 Polarized Gluon Distribution Function

The measurement of the polarized gluon distribution function is important for understanding the origin of the proton spin. The polarized gluon distribution function has been measured by HERMES [99] at DESY using a deep inelastic scattering. The process used is $e + p \rightarrow h^+ h^- X$, where $h = \pi, K$. SMC and COMPASS also reported the results. Another approach to the polarized gluon distribution function is a measurement of prompt photon production ($gq \rightarrow \gamma q$) in proton-proton collisions. The polarized gluon distribution function can be evaluated from double spin asymmetry [100];

$$A_{LL} = \frac{1}{P_1 P_2} \frac{N_{++} - N_{+-}}{N_{++} + N_{+-}} \quad (2.21)$$

where P_1 and P_2 are the beam polarizations, N_{++} represents the number of observed photon when helicity of beam1 is + and helicity of beam2 is +. N_{+-}

represents the number of photons when helicity of beam1 is + and helicity of beam2 is -. Figure 2.17 shows a sketch of the collisions of the polarized protons. The A_{LL} can be written to Leading-Order (LO) as follows [100];

$$A_{LL} \approx \frac{\Delta g(x_1)}{g(x_1)} \cdot \left[\frac{\sum_q e_q^2 [\Delta q(x_2) + \Delta \bar{q}(x_2)]}{\sum_q e_q^2 [q(x_2) + \bar{q}(x_2)]} \right] \cdot \hat{a}_{LL}(gq \rightarrow \gamma g) + (1 \leftrightarrow 2). \quad (2.22)$$

where $\Delta g(x)$ and $g(x)$ are polarized and unpolarized gluon distribution function. $\Delta q(x)$ ($\Delta \bar{q}(x)$) and $q(x)$ ($\bar{q}(x)$) are polarized and unpolarized quark (anti-quark) distribution function. The e_q represents the electric charge of quarks. The \hat{a}_{LL} is the partonic asymmetry and is calculable with pQCD. The polarized gluon distribution function will be measured from prompt photon production at RHIC in the near future as the luminosity and the beam polarization are increasing every year.

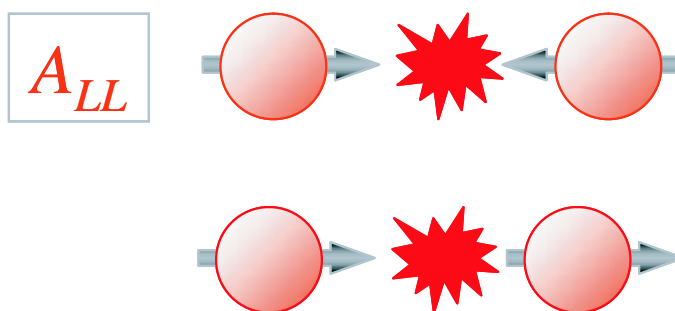


Figure 2.17: A sketch of the collisions of the polarized protons. The red circles denote the proton beam. The arrows denote the direction of the proton spin. The top figure shows the helicity of beam1 (left):+, beam2 (right):- . The bottom figure shows the helicity of beam1 (left):+, beam2 (right):- .

2.4 Heavy Ion Physics

Quarks are confined inside hadron, as discussed in Section 2.1.3. However, in a high density and/or high temperature condition, the hadrons are expected to form another state of matter. This is called quark gluon plasma (QGP). The QGP is related to the early universe. Figure 2.18 shows a phase diagram as functions of temperature and density. According to a recent lattice calculation [101], the transition temperature at 0 baryon density is 170 MeV. The QGP searches have been performed in heavy ion collisions at the Bevatron at

Berkeley, the Alternating Gradient Synchrotron (AGS) at BNL, the Super Proton Synchrotron (SPS) at CERN, and at RHIC.

One of the possible signal of QGP is jet quenching effect. The parton loses its energy with strong interaction when it goes through the QGP, which is predicted with the QCD calculation [102, 103, 104, 105]. The jet production in heavy ion collisions is reduced with strong interactions in the QGP matter, but prompt photon production in heavy ion collisions is not reduced because it does not interact by strong interaction. That is the jet quenching scenario. Therefore, the prompt photon production in proton-proton collisions can be a good reference for QGP study.

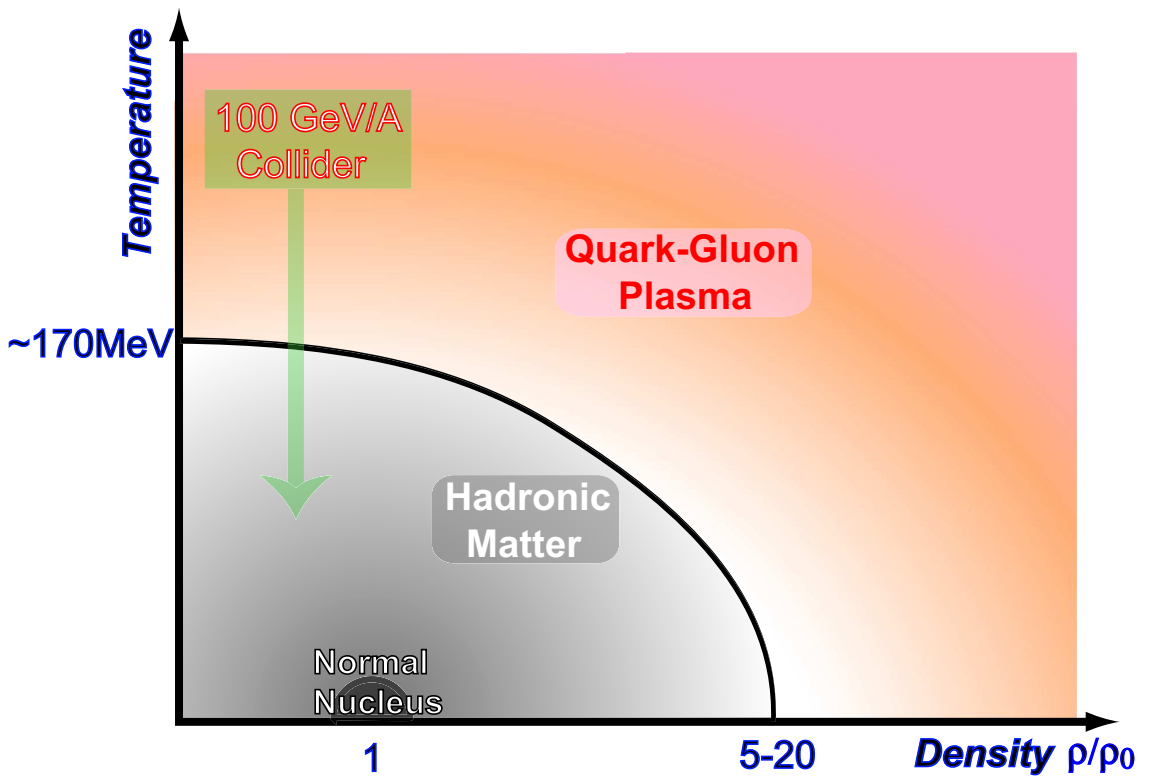


Figure 2.18: Phase diagram as functions of density and temperature.

Chapter 3

Experimental Setup

The RHIC complex and PHENIX detector are overviewed in this chapter. The description of the RHIC complex is described in Section 3.1, and the PHENIX detector is overviewed in Section 3.2 - 3.8.

3.1 RHIC Accelerator

The Relativistic Heavy Ion Collider (RHIC) [106] at Brookhaven National Laboratory can provide collisions of various ions from proton to Au. The RHIC is also operated as the first polarized proton-proton collider. The RHIC is designed to accelerate polarized protons up to 250 GeV and Au nuclei up to 100 GeV/nucleon. The designed luminosity is $2 \times 10^{26} \text{cm}^{-2} \text{s}^{-2}$ for Au ions and $2 \times 10^{32} \text{cm}^{-2} \text{s}^{-2}$ for proton. The bunch crossing intervals is 106 nsec when there are 120 bunches in each ring.

Figure 3.1 shows a schematic view of the RHIC complex. It consists of the LINAC, the Booster, the Tandem van de Graaff, the Alternating Gradient Synchrotron (AGS), and the RHIC main ring. The polarized protons are injected into LINAC and accelerated up to 200 MeV. Exiting from the LINAC, the polarized protons are transferred to the Booster and then injected into the AGS. The AGS accelerates the polarized protons up to 23.4 GeV and injects them into one of the RHIC main rings. The RHIC main ring consists of two rings, one is called Blue ring, the other Yellow ring. The beam is transferred clockwise in the Blue ring and anti-clockwise in the Yellow ring. The polarization of proton is maintained with Siberian Snake magnets [107] in the AGS and RHIC ring.

In the Au-Au collisions, the Au ions are accelerated up to 1 MeV/nucleon using the Tandem van de Graaff and injected into the Booster. The Booster accelerates them up to 95 MeV/nucleon. They are injected into the AGS and

accelerated to 8.86 GeV using the AGS. They are transferred to the RHIC main ring. Table 3.4 shows the summary of collected data with PHENIX at RHIC during the recent RHIC beam periods.

There are four experiments in RHIC. The PHENIX detector is located at 8 o'clock, if the north is considered to be 12 o'clock direction. The other detectors, STAR [118], PHOBOS [119] and BRAHMS [120], are located at 6 o'clock, 10 o'clock and 2 o'clock, respectively.

The design value of integrated luminosity of proton-proton collision is 320 pb^{-1} at $\sqrt{s} = 200 \text{ GeV}$ and 800 pb^{-1} at $\sqrt{s} = 500 \text{ GeV}$. The design value of the proton beam polarization is 70%. The luminosity and the polarization of the proton beam have been improved every year as shown in Table 3.4.

Run	Period	Species	$\sqrt{s_{NN}}$	Integrated luminosity	Beam polarization
1	2000	Au+Au	130GeV	$1 \mu\text{b}^{-1}$	-
2	2001-2002	Au+Au	200GeV	$24 \mu\text{b}^{-1}$	-
		p+p	200GeV	0.15 pb^{-1}	15%
3	2002-2003	d+Au	200GeV	2.74 nb^{-1}	-
		p+p	200GeV	0.35 pb^{-1}	27%
4	2004	Au+Au	200GeV	$241 \mu\text{b}^{-1}$	-
		Au+Au	62.4GeV	$9 \mu\text{b}^{-1}$	-
		p+p	200GeV	0.12 pb^{-1}	40%
5	2004-2005	Cu+Cu	200GeV	3 nb^{-1}	-
		Cu+Cu	62.4GeV	0.19 nb^{-1}	-
		Cu+Cu	22.5GeV	$2.7 \mu\text{b}^{-1}$	-
		p+p	200GeV	3.8 pb^{-1}	49.5/44.5%

Table 3.1: Summary of the collected data with PHENIX at RHIC during the recent RHIC beam period.

3.2 PHENIX Detector Overview

The PHENIX detector subsystems [108] are described in this section. The PHENIX detector consists of four instrumented spectrometers and three beam

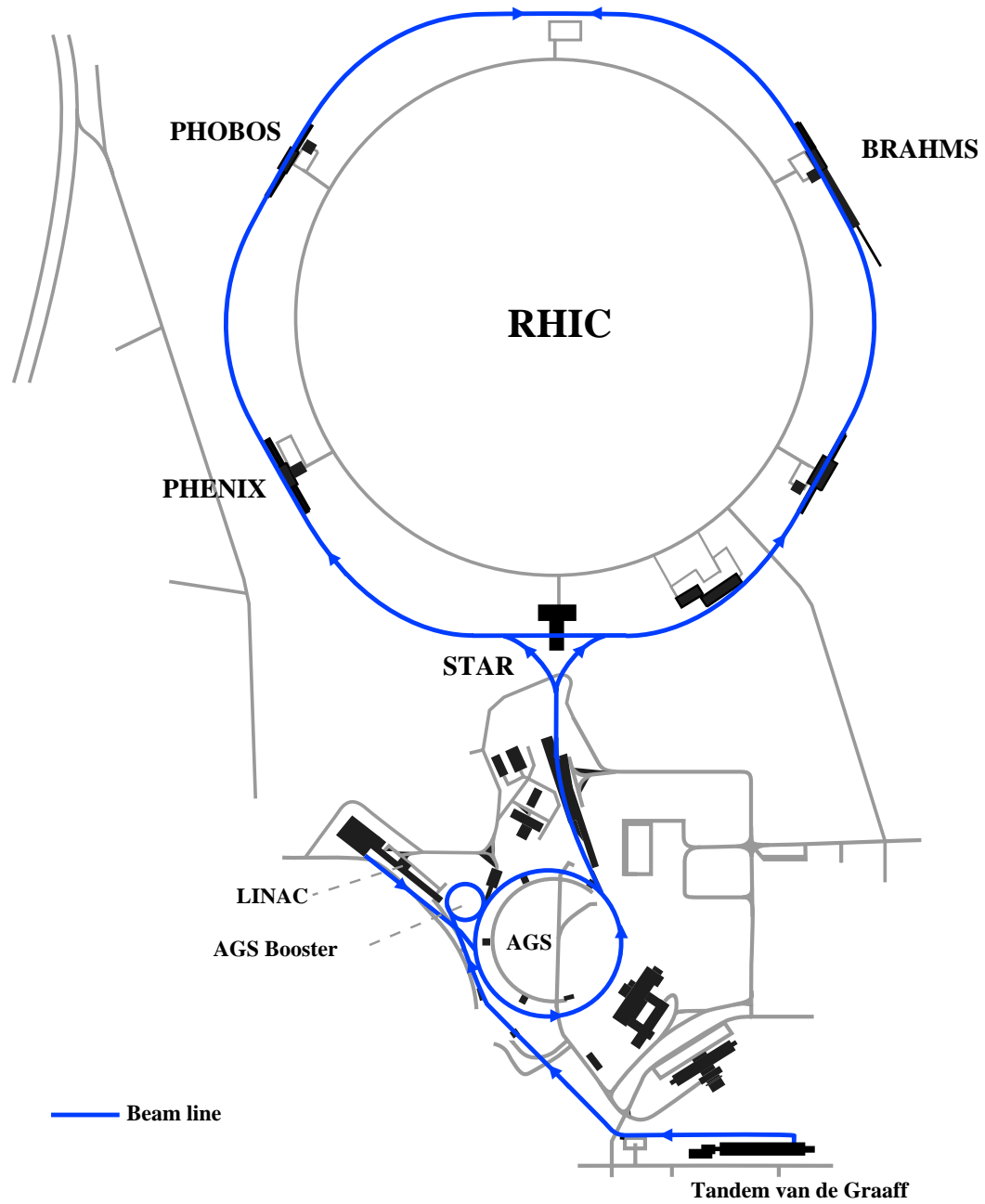


Figure 3.1: Schematic view of the RHIC complex.

detectors. One of the instrumented spectrometers is called Central Arm [110, 111]. The 'Central Arm' consists of Drift Chamber (DC), Pad Chamber (PC), Ring Imaging Cerenkov Detector (RICH), Time Expansion Chamber (TEC), Time Of Flight Counter (TOF) and ElectroMagnetic Calorimeter [112] (EMCal). They are explained in Section 3.5 and Section 3.6. Another one is called the 'Muon Arm' [113]. The Muon Arm consists of Muon Tracker (MuTr) and Muon Identifier (MuID). They are described in Section 3.7. The beam detectors are Zero Degree Calorimeter (ZDC) [117], Beam Beam Counters (BBC) [114] and Multiplicity-Vertex Detector (MVD). They are described in Section 3.4. Table 3.2 shows the summary of the PHENIX detector subsystem. Table 3.3 shows the summary of the typical resolution PHENIX detector.

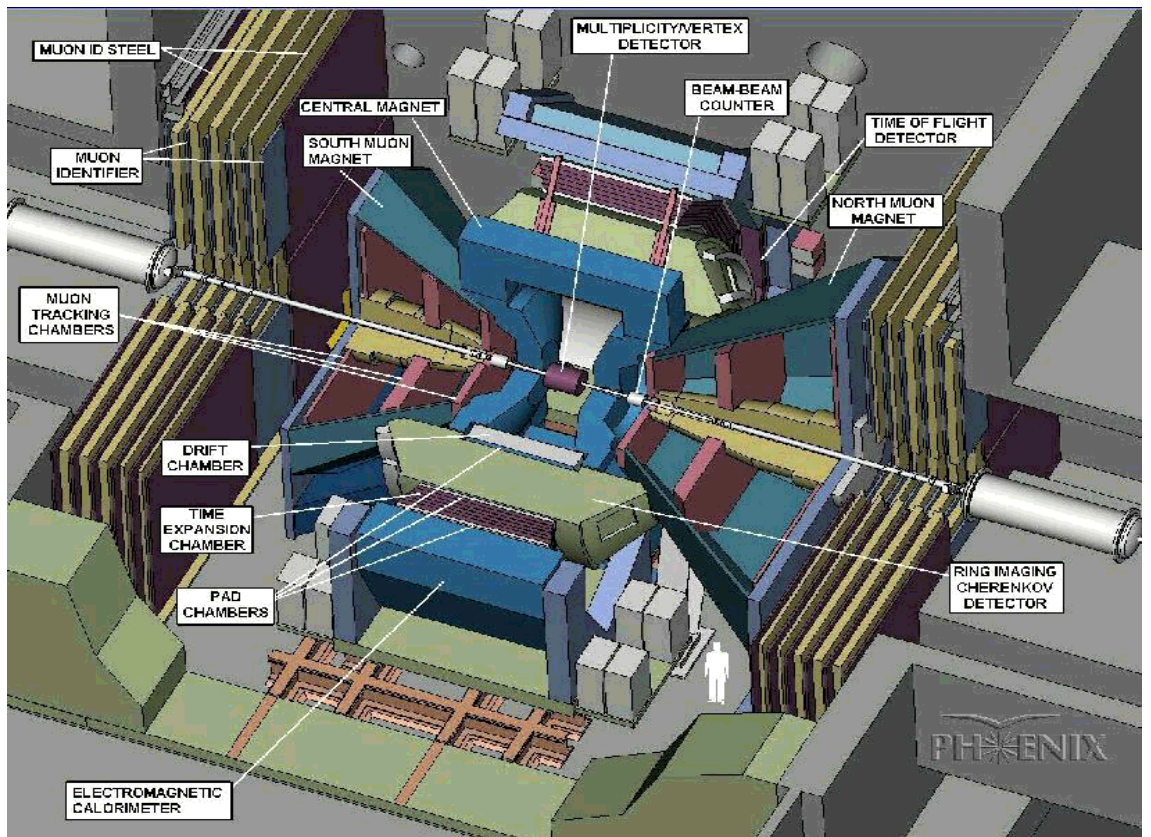


Figure 3.2: A cutaway drawing of the PHENIX detector is shown. The major detector subsystems are pointed by labelled arrows.

Element	Pseudo-rapidity $\Delta\eta$	Azimuthal angle $\Delta\phi$	Purpose and Special Features
CM	± 0.35	360°	Up to $1.15\text{T} \cdot \text{m}$.
MM(North)	-1.1 to -2.2	360°	$0.72\text{T} \cdot \text{m}$ for $\eta = 2$.
MM(South)	1.1 to 2.4	360°	$0.72\text{T} \cdot \text{m}$ for $\eta = 2$.
BBC	$\pm(3.1\text{to}3.9)$	360°	Starting timing, fast vertex.
ZDC	$\pm 2\text{mrad}$	360°	Minimum bias trigger.
DC	± 0.35	$90^\circ \times 2$	Charged particle tracking.
PC	± 0.35	$90^\circ \times 2$	Pattern recognition, tracking for nonbend direction.
TEC	± 0.35	90°	Pattern recognition.
RICH	± 0.35	$90^\circ \times 2$	Electron identification.
TOF	± 0.35	45°	Hadron identification.
EMCal (PbSc)	± 0.35	$90^\circ + 45^\circ$	Photon and electron detection.
EMCal (PbGl)	± 0.35	45°	Photon and electron detection.
MuTr (South)	-1.15 to -2.25	360°	Muon tracking.
MuTr (North)	1.15 to 2.44	360°	Muon tracking.
MuID (South)	-1.15 to -2.25	360°	Muon identification.
MuID (North)	1.15 to 2.44	360°	Muon identification.

Table 3.2: Summary of the PHENIX detector subsystem.

Subsystems	Resolution
BBC	$\sigma_{t_0} \sim 20\text{psec}, \sigma_{z\text{-vertex}} \sim 60\text{mm}$
ZDC	$\sigma_{z\text{-vertex}} \sim 250\text{mm}$
DC	$\sigma_{\alpha} \sim 1\text{mrad}, \sigma_z \sim 2\text{mm}$
PC1	$\sigma_{r\text{-}\phi} \sim 2.5\text{mm}, \sigma_z \sim 1.7\text{mm}$
PC2	$\sigma_{r\text{-}\phi} \sim 3.9\text{mm}, \sigma_z \sim 3.1\text{mm}$
PC3	$\sigma_{r\text{-}\phi} \sim 4.6\text{mm}, \sigma_z \sim 3.6\text{mm}$
TOF	$\sigma_t \sim 110\text{psec}$
TEC	$\sigma_{\text{space}} \sim 0.35\text{mm}$

Table 3.3: Summary of the resolution of PHENIX subsystems.

3.3 Magnet System

The PHENIX magnet system [109] consists of two spectrometer magnets with iron yoke and water-cooled copper coils. One is the Central Magnet (CM), the others are the north and south Muon Magnets (MMN, MMS). Figure 3.3 shows a schematic view of PHENIX magnet system on a cutaway drawing.

The CM provides a magnetic field around the collision point which is parallel to the beam. It allows to measure the momentum of charged particle in the polar angle range from 70° to 110° . Figure 3.4 shows lines of the magnetic field on a cutaway drawing of the PHENIX magnet system. The magnetic field integral varies from 0.43 Tm to 1.15 Tm at $\theta = 90^\circ$ (Appendix A). The magnetic field is needed up to the position of DC because the momentum of charged particles is calculated with the curvature between interaction point and DC. On the other hand, the magnetic field must be small enough in the region $R > 200$ cm, where R is the distance from vertex. The RICH located in $2.4 \text{ m} < R < 4.0 \text{ m}$ requires that the magnetic field is less than 100 Gauss-m, in order to minimize the smearing of the Cherenkov rings associated with low momentum electron. In addition, the photomultiplier tubes of the RICH and EMCal can be operated only in low magnetic field.

The MMN and MMS use solenoid coils to provide a radial magnetic field for reconstruction of muon momentum. The MMN covers a pseudo-rapidity range of -1.1 to -2.2, and MMS covers a pseudo-rapidity (see Appendix A) range of 1.1 to 2.4. They cover full azimuthal angle. The magnetic field integral is 0.72 Tm at $\theta = 15^\circ$.

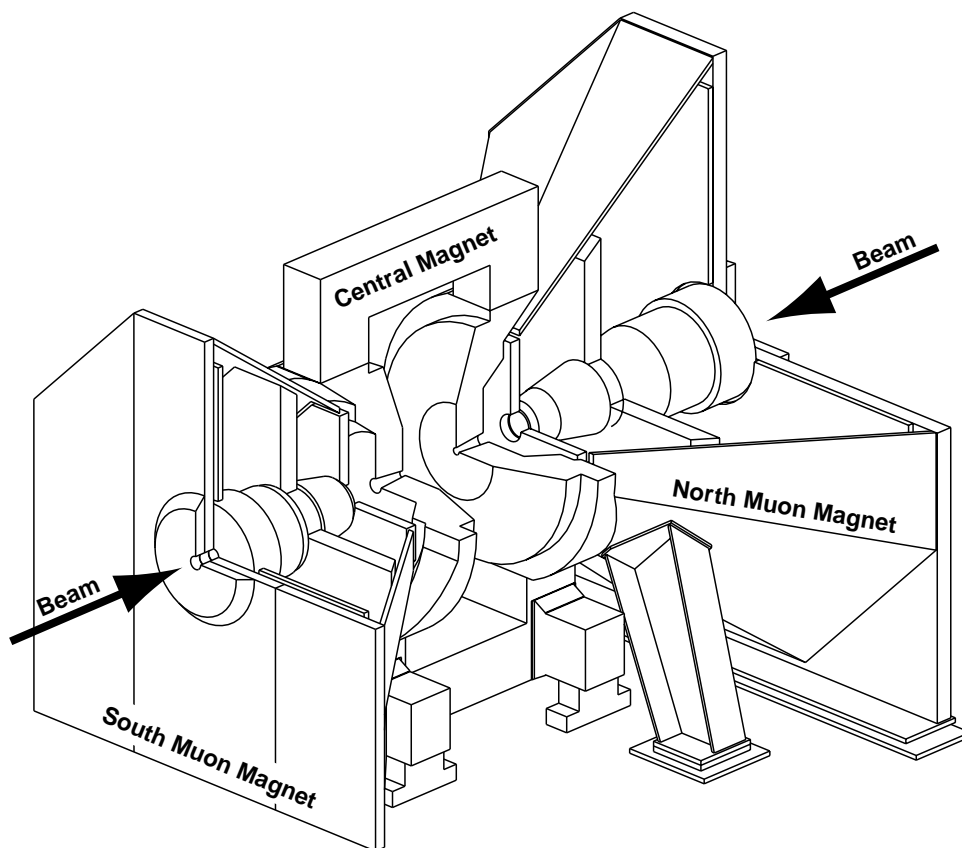
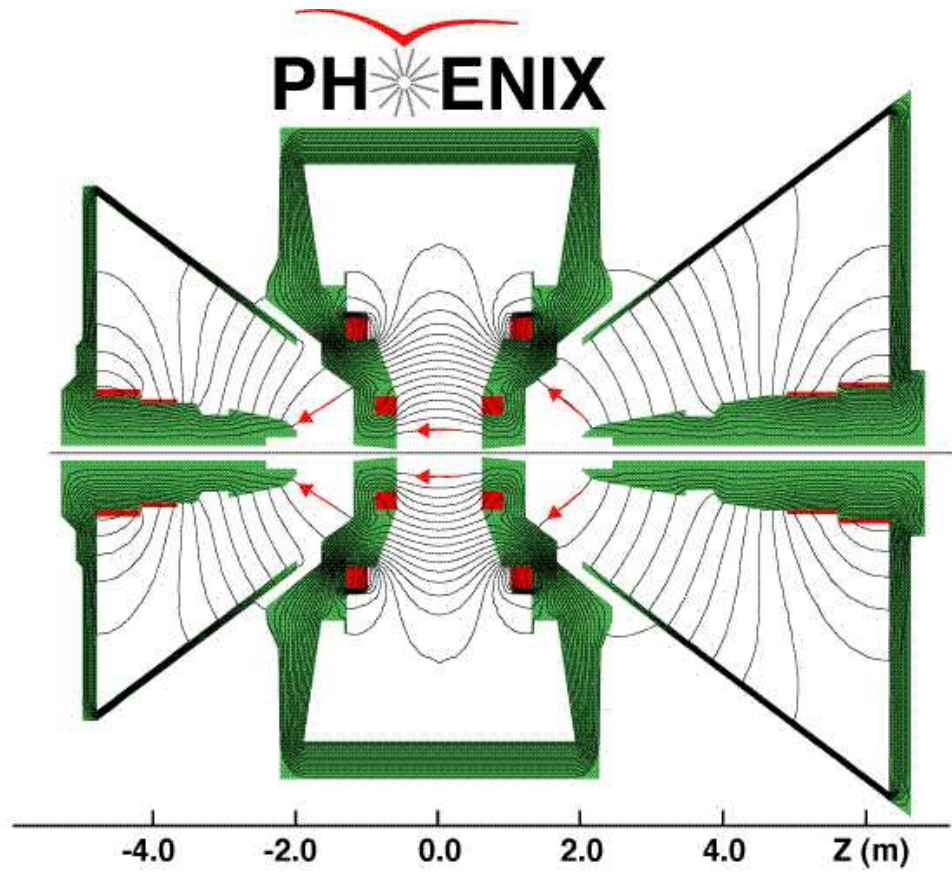


Figure 3.3: The PHENIX magnets are shown in perspective and cut away to show the interior structures. Arrows indicate the beam direction of RHIC.



Magnetic field lines for the two Central Magnet coils in combined (++) mode

Figure 3.4: CM and MM magnetic field lines are shown on a cutaway drawing of the PHENIX magnets. The beam line is parallel to the Z axis in this figure. The beams collide at $Z = 0$.

3.4 Beam Detectors

In this section, the PHENIX Global Detectors, namely BBC and ZDC are described. The PHENIX Global Detectors are used to measure the z-vertex to produce the trigger timing and to measure the luminosity in heavy ion and proton-proton collisions.

3.4.1 Beam-Beam Counters (BBC)

The PHENIX BBC consists of two sets of counters installed on the north side and the south side of the collision vertex point in parallel with the beam axis. The counters on the north and south sides are named BBCN and BBCS, respectively. The BBCs are located 144 cm away from the interaction point and surround the beam pipe. The BBCs cover a pseudo-rapidity range from 3.0 to 3.9 and the full azimuthal angle ϕ . The BBC consists of 64 one-inch mesh dynode photomultiplier tubes with a 3 cm thick quartz radiator as a Cherenkov radiator (Figures 3.5, 3.6).

The BBC is used to measure the collision vertex point in the direction of the beam axis, to measure the timing of beam-beam collisions for the time of flight of produced particles, and to produce a signal for the PHENIX LVL1 trigger. Figure 3.7 shows a sketch of a collision and produced particles coming to the BBCs. The z-vertex position(BBCz) and the time of beam-beam collision (T_0) are calculated as follows;

$$BBCz = \frac{T_S - T_N}{2} \times c \quad (3.1)$$

$$T_0 = \frac{T_S + T_N - 2L/c}{2} \quad (3.2)$$

where T_N and T_S are the averaged hit time with the incoming particles, c is the light velocity and L is the distance from $z = 0$ to both BBCs, $L = 144.35$ cm. The BBC can be triggered only by the 50% and 93% of the inelastic collisions for proton-proton and Au+Au collisions at $\sqrt{s} = 200$ GeV, respectively, because the coverage of the BBC is limited.

3.4.2 Zero Degree Calorimeters (ZDC)

The ZDC is located at ± 18 m from $z = 0$ along the beam line. It is a hadron calorimeter to detect neutrons emitted along the beam direction. It measures their total energy. Figure 3.8 shows the view of the collision region and the schematic view of the ZDC location including deflection of protons and charged fragments. Due to the bending magnet of the RHIC ring, most

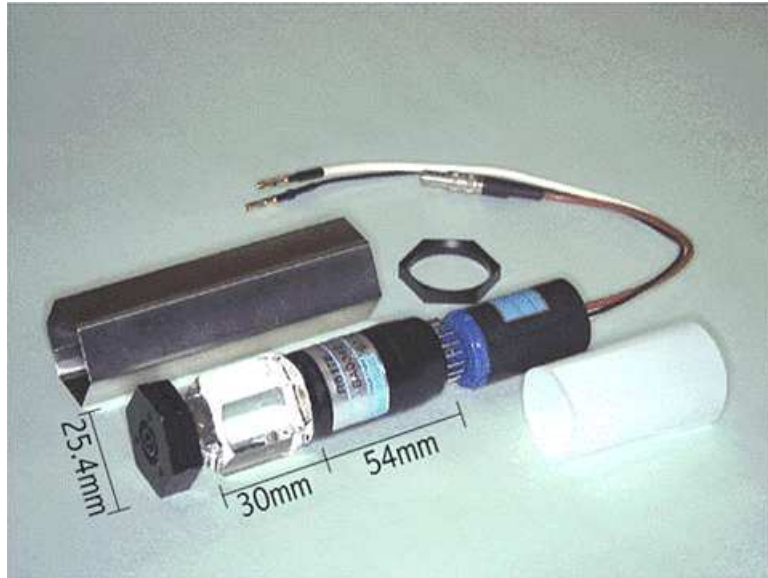


Figure 3.5: A single Beam-Beam counter consists of one-inch mesh dynode photo-multiplier tubes with a 3 cm thick quartz radiator.



Figure 3.6: A BBC array consists of 64 BBC elements.

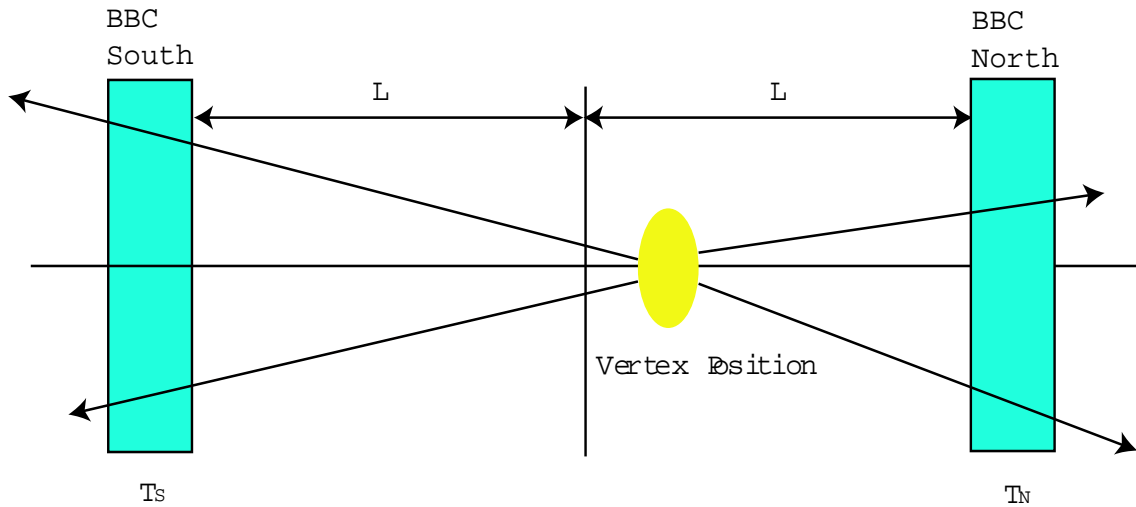


Figure 3.7: A sketch of a collision and produced particles coming to the BBCs. T_N and T_S are the averaged hit time of incoming particles.

of the charged particles are removed from the ZDC acceptance. Figure 3.9 shows the design of the production of Tungsten Module. The ZDC is used to measure the luminosity in heavy ion collisions and to lower the systematic uncertainty of the measurement of the luminosity in proton-proton collisions. The ZDC's are used together with BBC for the measurement of centrality for heavy ion collisions.

3.5 Central Arm Spectrometers

In this section, the PHENIX tracking detectors and particle identification detectors are explained. The PHENIX tracking system consists of the DC, the PC, and the TEC. The PHENIX particle identification detectors consists of the RICH, TOF, and TEC. They all together provide good tracking resolution and particle separation. The Central arm spectrometer is shown in Figure 3.10. The detectors are located as in this figure viewed from the beam line.

3.5.1 Drift Chamber (DC)

The PHENIX Drift Chambers (DC) have a cylindrical shape and are located in the region from 2 to 2.4 m from the z axis and 2 m along the beam direction.

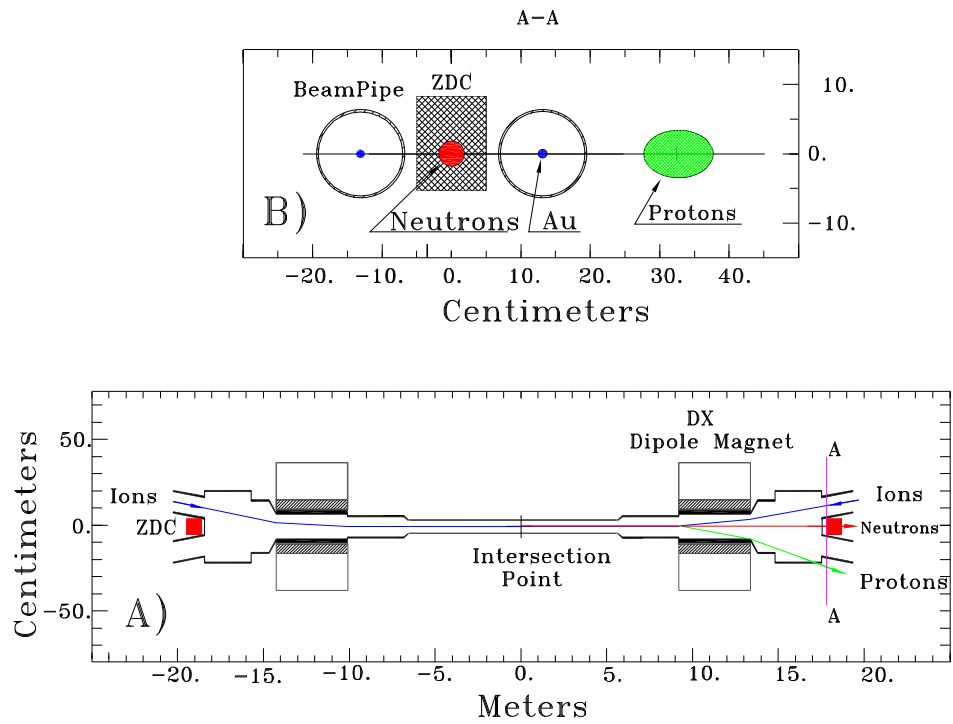


Figure 3.8: The top picture is the view of the collision region and the bottom picture is the schematic view of the ZDC location including deflection of protons and charged fragments.

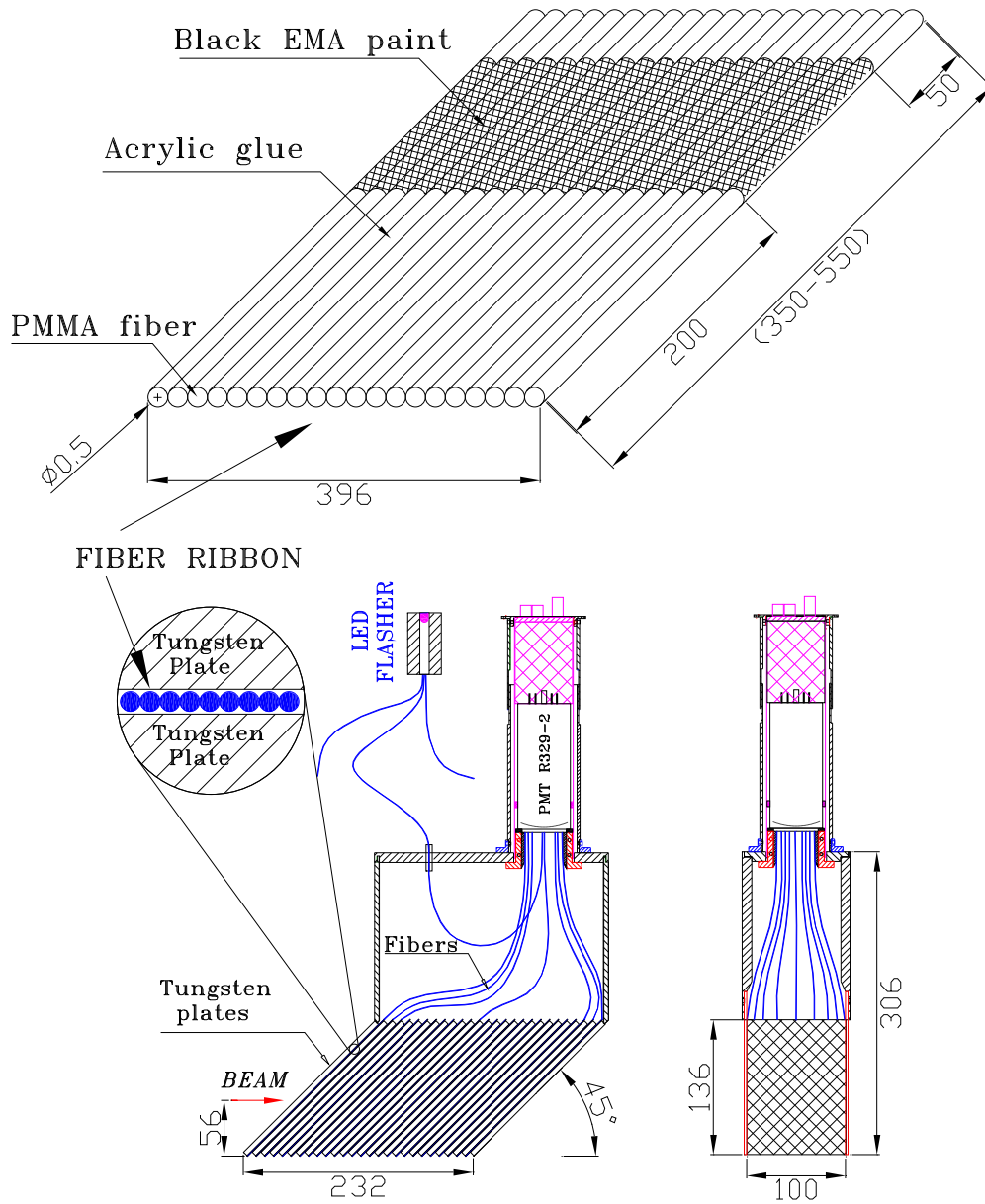


Figure 3.9: The design of the production of Tungsten Module. Dimensions are in mm.

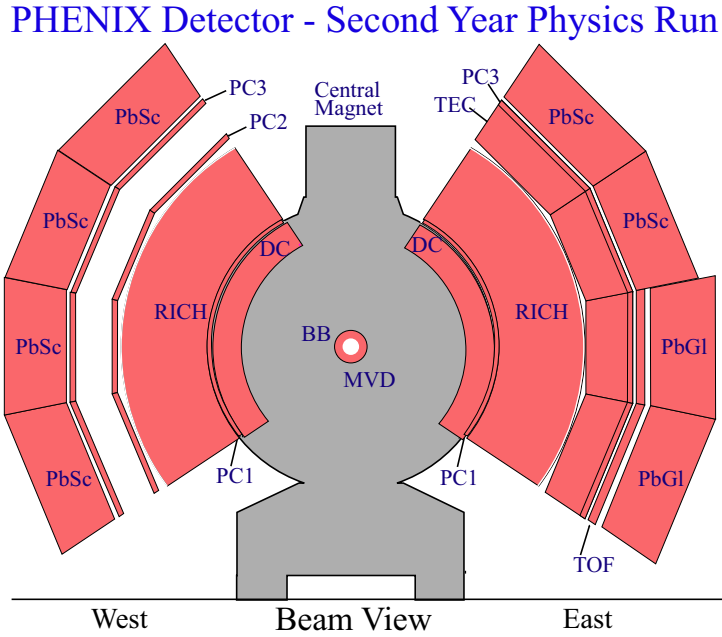


Figure 3.10: The central spectrometer has two arms which are viewed in a cut through the collision point.

The residual magnetic field at this location is 0.6 kG at maximum. Figure 3.10 shows the location of the DCs relative to the other detectors in the central spectrometer. Each DC determines p_T of each particle by measurement of charged particle trajectories in the r - ϕ direction. The DC is also involved in the pattern recognition at high particle track densities by providing the particle track information which is used to link tracks through the various PHENIX detector subsystems.

The momentum (in GeV/c) for a $Z = 1$ particle (Z :electric charge) determined with the DC is related to the angle α (Figure 4.32) (in mrad) by:

$$p = \frac{K}{\alpha} = \frac{87}{\alpha} \quad (3.3)$$

where 87 mrad GeV/c is simply the magnetic field integral:

$$K = \int_{0.3/R_{DC}} B dl \quad (3.4)$$

The DC system consists of two independent gas volumes. They are located in the west and east arms. The east arm detector is the same as the west arm like a mirror image. Each detector's volume is determined by a cylindrical titanium frame defining the azimuthal angle ϕ and beam axis limits of the

detector volume (Figure 3.11). The limits of the gas volume is defined by five-mil Al-mylar radially. Each frame is filled with drift chamber modules and is divided into 20 equal sectors covering 4.5° in ϕ . There are six types of wire modules stacked radially in each sector: X1, U1, V1, X2, U2 and V2. Each module contains 4 sense (anode) planes and 4 cathode planes forming cells with a 2-2.5 cm drift space in the ϕ direction. The X1 and X2 wire cells run in parallel to the beam to perform precise track measurements in r - ϕ . These wire cells are followed by two sets of small angle U,V wire planes. Those are used in the pattern recognition. U1, V1, U2, and V2 wires have stereo angles of about 6° relative to the X wires and measure the z coordinate of the track. The stereo angle was selected to minimize track ambiguities by matching the z resolution of the pad chambers. Each of the X- and U,V-stereo cells contain 12 and 4 anode (sense) wires, respectively. As a result, there are 40 drift cells in the DC located at different radii. Figure 3.12 shows the layout of wires within one DC sector. The stereo wires start in a sector on one side and end in a neighboring sector on the other side of the DC. The drift chambers are filled with a working gas mixture of 50% Ar and 50% Ethane.

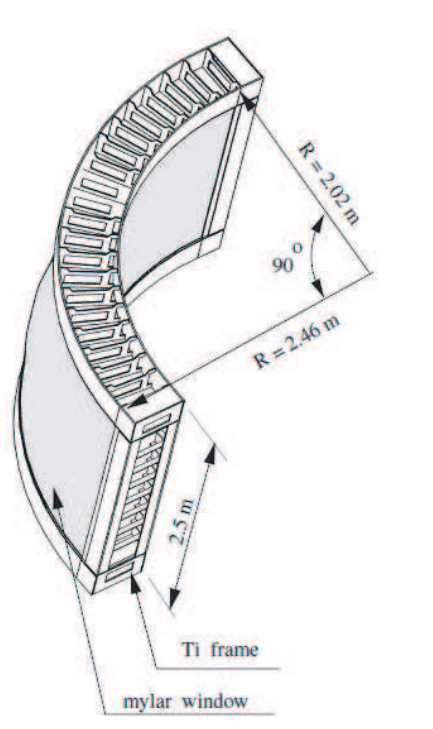


Figure 3.11: The view of DC frame.

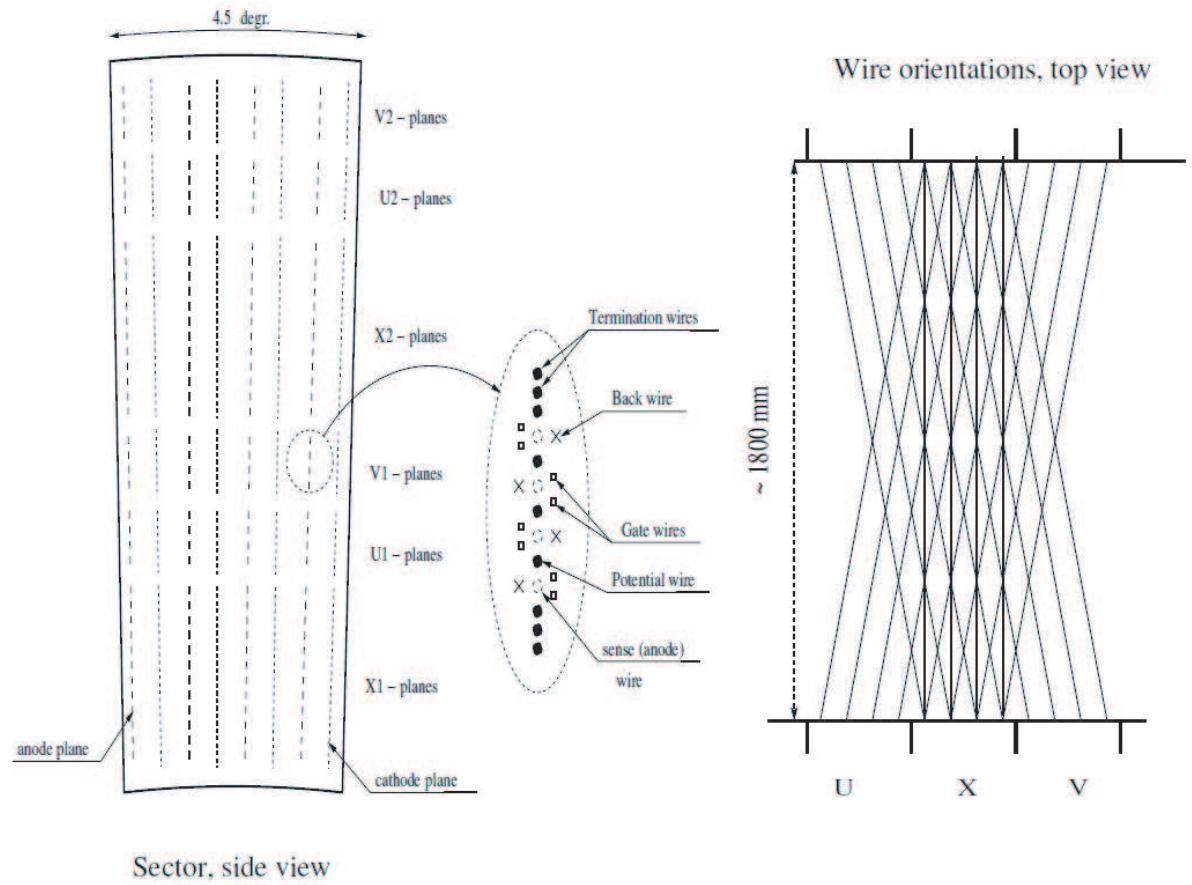


Figure 3.12: The schematic view of wire positions within one sector and inside the anode plane.

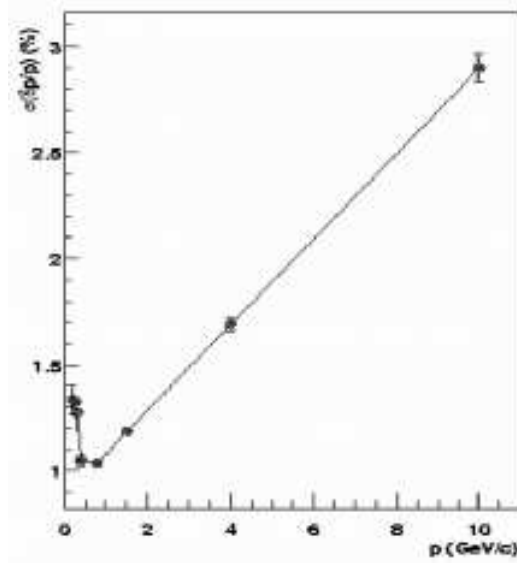


Figure 3.13: The distribution of momentum resolution.

3.5.2 Pad Chamber (PC)

The PHENIX Pad Chambers (PC) are multiwire proportional chambers which consist of three separate layers of the PHENIX central tracking system. Each detector contains a single plane of wires inside a gas volume bound by two cathode planes. One cathode is finely segmented into an array of pixels. The charge induced on a number of pixels when a charged particle starts an avalanche on an anode wire, is read out through specially designed readout electronics.

The PC system determines space points along the straight line particle trajectories outside the magnetic field. The radial location of the PC's in the central tracking arms is shown in Figure 3.10. The innermost pad chamber plane is located between the DC and the Ring Imaging Cherenkov Counter (RICH) (See Section 3.5.3) on both East and West arms, which is called PC1. PC3 is mounted just in front of the EMCal on both arms while the PC2 layer behind the RICH is present in the West arm only. PC1 is also essential for determining the three-dimensional momentum vector by providing the z coordinate at the exit of the DC.

Figure 3.14 shows the pad and pixel geometry (left). A cell defined by three pixels is at the center of the right picture.

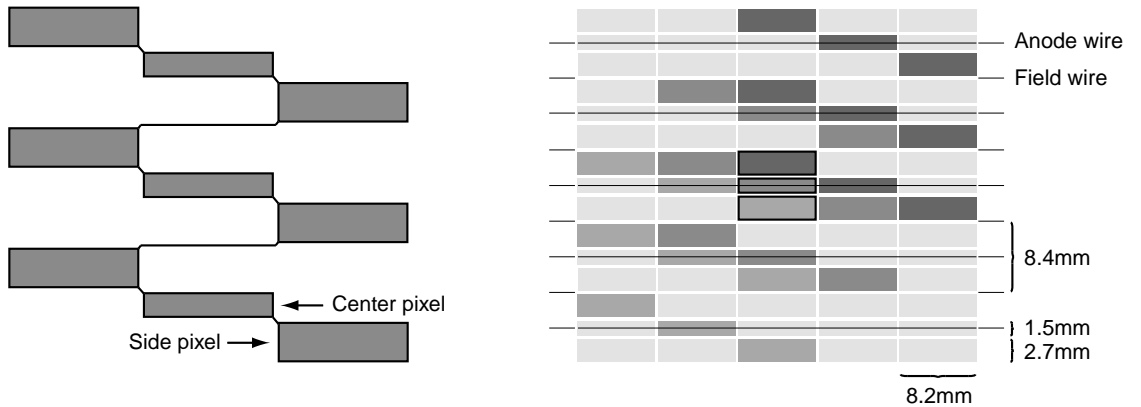


Figure 3.14: The pad and pixel geometry (left). A cell defined by three pixel is at the center of the right picture.

3.5.3 Ring Imaging Cherenkov Detector (RICH)

Ring Imaging Cherenkov (RICH) detector is contained in each of the PHENIX central arms. RICH provides e/π discrimination below the π Cherenkov threshold, which is about 4 GeV/c. In combination with the EMCAL in each arm and the TEC in East arm, the goal is to limit the false identification of hadrons as e^+ and e^- to less than 1 per 10^4 , for momenta below the π Cherenkov threshold. The EMCAL can reject about 90% of hadrons at momenta > 1 GeV/c, and the TEC (present in only East arm of PHENIX) provides dE/dx separation of electrons from pions for momenta below about 1 GeV/c.

Because the RICH is an electron detector and there are several detectors behind it, the amount of material in the RICH within the PHENIX acceptance is of great concern. Due mostly to π^0 decay, there is very large photon flux for central collisions of heavy ions which causes e^+e^- pairs to be created in whatever material is inside the RICH acceptance. The RICH windows, mirrors and even the radiator gas itself, have to be as thin as possible for this reason. As built, the PHENIX RICH detectors have a total thickness of 2% of a radiation length when filled with ethane gas.

Figure 3.15 contains a cutaway drawing of one of the RICH detectors revealing the internal components.

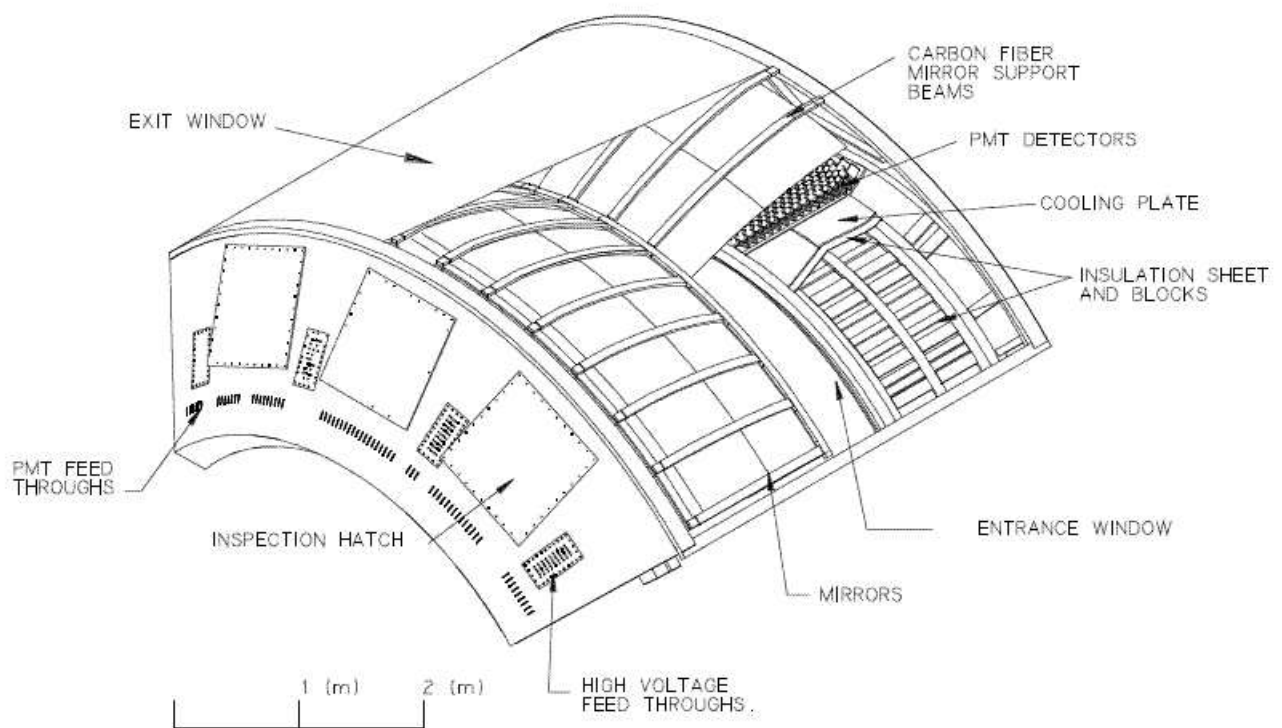


Figure 3.15: A cutaway view of one arm of the PHENIX RICH detector.

3.5.4 Time Expansion Chamber (TEC)

The Time Expansion Chamber (TEC) consists of a set of 24 large multi-wire tracking chambers arranged in four, six-chamber sectors (Figure 3.16) which reside in East arm. The TEC measures all charged particles passing through its active area, providing direction vectors that are matched to additional track information from the DC's and PC's. The tracking information is used to solve the complex pattern recognition problems associated with the high particle multiplicities in relativistic heavy ion physics. It aids in background rejection for particles passing into the EMCal and TOF wall. The detector system allows for systematic studies of tracking efficiency and background rejection versus multiplicity in coordination with the DC. The TEC also enhances the momentum resolution of the Central Arm at $p_T \geq 4$ GeV/c by combining with the DC to provide a long lever arm for improved track-angle resolution. In addition the TEC measures ionization energy losses (dE/dx) of charged tracks which enables particle identification, particularly electron/pion separation, over a momentum range important to the physics goals of the experiment.

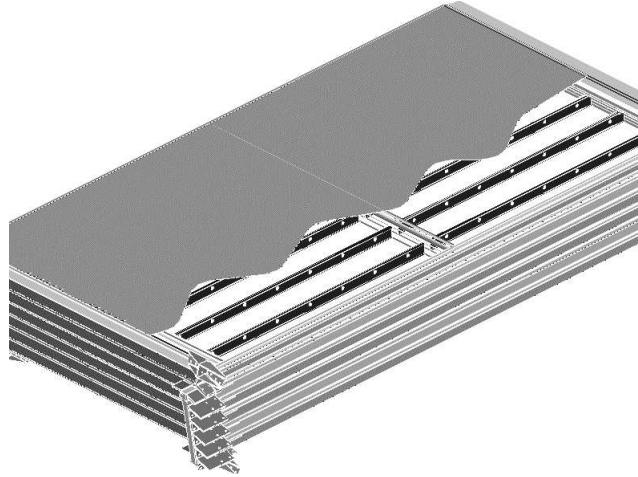


Figure 3.16: TEC six-plane sector.

3.5.5 Time Of Flight Counter (TOF)

Time-of-Flight (TOF) measurements are one of the most powerful methods for separating particle species. The particle identification can be done by comparing the particle time of flight to the measured momentum of the particle. The TOF contains 960 scintillator slats oriented along the radial di-

rection. Its timing resolution was about 100 ps in the year 2000, the first year of operation of the experiment, which provided a 4σ π/K separation up to 2.4 GeV/c. Figure 3.17 shows schematic diagram of the components of a single TOF panel, which consists of 96 plastic scintillation counters with photomultiplier tubes at both ends, light guides and supports.

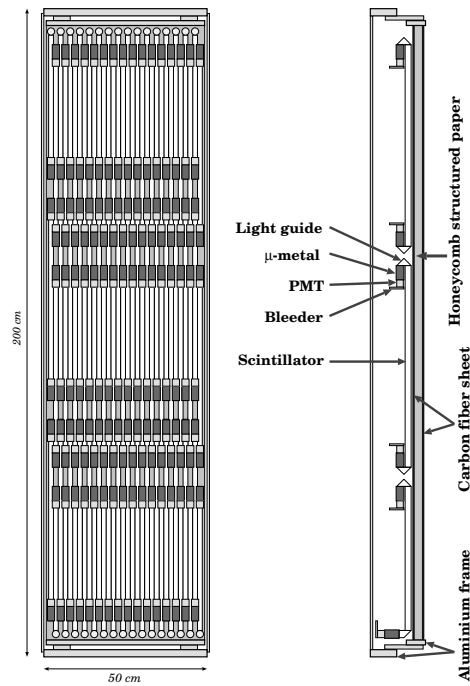


Figure 3.17: Schematic view of the components of a single TOF panel which consists of 96 plastic scintillation counters with photomultiplier tubes at both ends, light guides and supports.

3.6 ElectroMagnetic Calorimeter (EMCal)

The PHENIX EMCal is described in this section. The PHENIX EMCal detects electrons and photons in heavy ion and proton-proton collisions, therefore it is very important for this analysis.

3.6.1 Overview of EMCal

The role of the Electromagnetic Calorimeter (EMCal) in PHENIX is a measurement of the energies and spatial positions of photons and electrons produced in collisions. It also plays a major role in particle identification and

is an important part of the PHENIX trigger system. The EMCal system can trigger on rare events with high transverse momentum (p_T) photons and electrons. Its signals are incorporated in Level-1 triggers for high multiplicity or large total transverse energy (E_T) events. In addition the EMCal provides a good measurement of the hadronic energy produced at mid-rapidity and thus of the E_T produced in the reaction.

The EMCal system consists of a total of 24768 individual detector modules divided between the Pb-Scintillator(PbSc) calorimeter, which provides six sectors of azimuthal coverage and the Pb-glass(PbGl) calorimeter comprised of two sectors. Both subdetectors are read out with photomultipliers and have good energy resolution and intrinsic timing characteristics. Their design is however quite different and they will be described separately. A description of special EMCal frontend electronics is also given. The location of the EMCal relative to the rest of the PHENIX detector is shown in Figure 3.10.

The properties of the PbSc and PbGl calorimeters are very different and they have different advantages and disadvantages. The PbSc is a sampling calorimeter while the PbGl is a Cherenkov calorimeter. The two detectors have different granularity, energy resolution, linearity, response to hadrons, timing properties and shower shape at normal and non-normal impact on the face of the tower. For example the PbGl has the better granularity and energy resolution while the Pb-scintillator has the better linearity and timing and the response to hadrons is better understood. Therefore, the data analysis, particle identification cuts and the resulting systematic errors are also different and will be discussed in separate sections. Choosing two different technologies was a deliberate decision by PHENIX which has the advantage of producing independent cross checks of results within the same experiment.

3.6.2 Lead Scintillator Calorimeter (PbSc)

The PbSc electromagnetic calorimeter is a sampling calorimeter made of alternating tiles of Pb and scintillator consisting of 15552 individual towers and covering an area of approximately 48 m². The basic building block is a module consisting of four (optically isolated) towers which are read out individually. The modules were subjected to quality control procedures designed to achieve consistent large light yield in all towers (12500 photons/GeV). A high precision calibration and monitoring system has been developed to achieve an absolute energy calibration better than 5% for day one operation at RHIC, and to maintain an overall long term gain stability of the order of 1%.

Each PbSc tower contains 66 sampling cells consisting of alternating tiles of Pb and scintillator. The edges of the tiles are plated with Al. These cells

	PbSc	PbGl
Radiation Length (X_0) [mm]	21	29
Moliere Radius (R_M) [mm]	~ 30	37
Channel		
Channel Front Surface [mm ²]	55.35x55.35	40x40
Depth [mm]	375	400
[X_0]	18	14
Super-module		
Number of Channels	144(12x12)	24(4x6)
Sector		
Number of Super-modules	18(3x6)	192(12x16)
Whole System		
Number of Sectors	6	2
Number of Channels	15552	9216
η Coverage	0.7	0.7
ϕ Coverage	$\pi/2+\pi/4$	$\pi/4$

Table 3.4: Fundamental parameters of PHENIX EMCAL. Moliere radius is defined as $R_M = 21\text{MeV} \times X_0/E_c$, where E_c is the critical energy. 99% of the energy is inside a radius $3R_M$.

are optically connected by 36 longitudinally penetrating wavelength shifting fibers for light collection. Light is read out by 30 mm FEU115M phototubes at the back of the towers. Four towers are mechanically grouped together into a single structural entity called a “module” as shown in Figure 3.18. Thirty six modules are attached to a backbone and held together by welded stainless steel skins on the outside to form a rigid structure called a “supermodule”. Eighteen supermodules make a sector, a $2 \times 4 \text{ m}^2$ plane with its own rigid steel frame. All major PbSc design parameters are listed in Table 3.4. The scintillating plastic contains an organic scintillator p-bis[2-(5-Phenyloxazolyl)]-benzene (POPOP) and a fluorescent additive p-Terphenyl (PT). Figure 3.18 shows the interior view of a PbSc calorimeter module. The PbSc energy linearity obtained by beam tests at CERN and BNL is shown in Figure 3.19. The PbSc energy resolution obtained by beam test at CERN and BNL is shown in Figure 3.20. The PbSc timing resolution is shown in Figure 3.21.

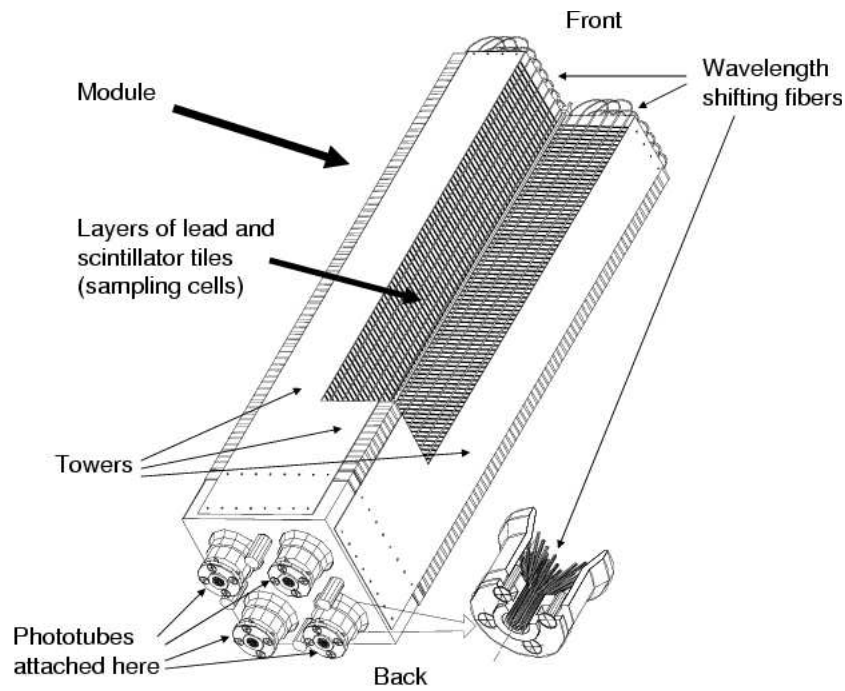


Figure 3.18: Interior view of a PbSc calorimeter module showing a stack of scintillator and lead plates, wavelength shifting fiber readout and leaky fiber inserted in the central hole.

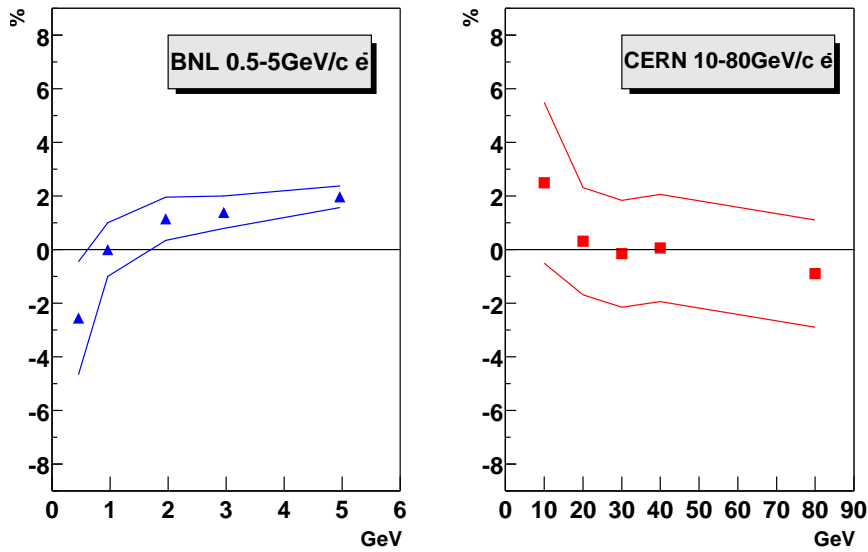


Figure 3.19: PbSc EMCAL energy linearity measured in beam tests at BNL (left) and CERN (right). The residual (calorimeter measured energy less the beam energy, divided by the beam energy) is shown for the 5x5 tower energy sum. The solid lines show total systematic uncertainties in the analysis.

3.6.3 Lead Glass Calorimeter (PbGl)

The PbGl calorimeter array comprises 9216 elements of a system previously used in CERN experiment WA98 [121]. The PbGl calorimeter occupies the two lower sectors of the East Central arm of PHENIX. The TOF is located in front of the PbGl sectors. Each PbGl sector comprises 192 supermodules (SM) in an array of 16 PbGl SM wide by 12 SM high as shown in Figure 3.22. Each PbGl SM comprises 24 PbGl modules in an array of 6 PbGl modules wide by 4 modules high. Each PbGl module is 40 mm x 40 mm x 400 mm in size. The PbGl modules within a SM are individually wrapped with aluminized mylar and shrink tube and 24 modules are glued together with carbon fiber and epoxy resin to form a self-supporting SM with a shared calibration system (see Fig 3.22). Steel sheets of 0.5 mm in thickness were used to house the phototubes and bases. The sheets were incorporated during the gluing process. An aluminized plastic foil on the front of the SM contains a hole for each PbGl module which allows entry for the LED light used for gain monitoring. A polystyrene reflective dome encloses the LED system on the front surface of the SM. Each PbGl module is read out with an FEU-84 photomultiplier. The high voltage for each photomultiplier is generated

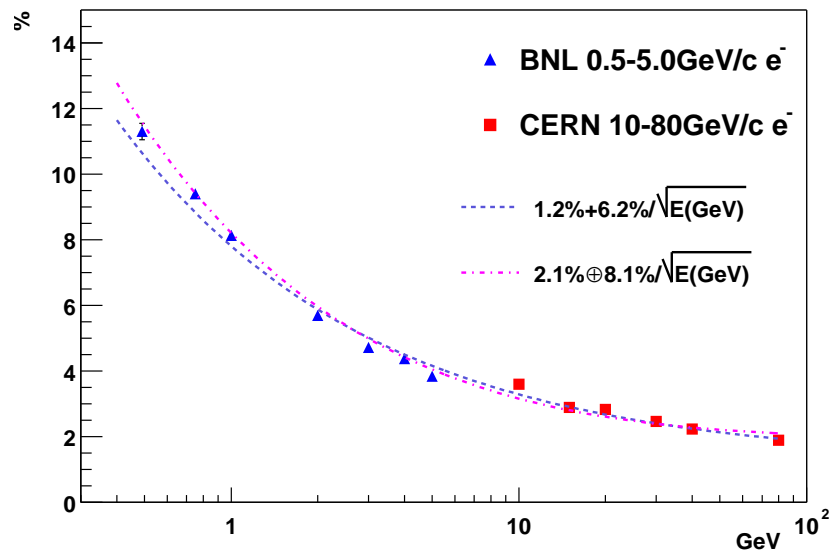


Figure 3.20: PbSc EMCAL energy resolution obtained by beam tests at CERN and BNL. The dashed line shows the fit to a linear formula ($\sigma(E)/E = 1.2\% + 6.2\%/\sqrt{E(\text{GeV})}$). The dashed dotted line shows the fit to the quadratic formula ($\sigma(E)/E = 2.1\% \oplus 8.1\%/\sqrt{E(\text{GeV})}$), where \oplus denotes a root of the quadratic sum, $a \oplus b = \sqrt{a^2 + b^2}$.

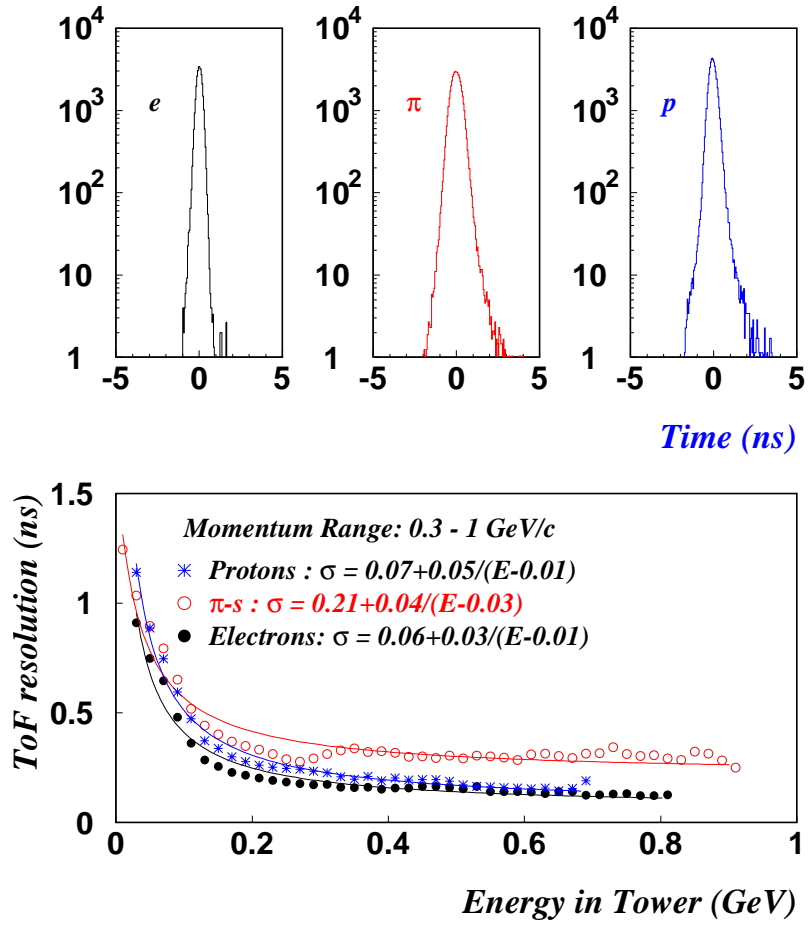


Figure 3.21: PbSc timing resolution for different particles. Top: lineshape for 1 GeV/c electrons, pions and protons. Bottom: resolution in the momentum range of 0.3-1.0 GeV/c.

in a Cockcroft-Walton type photomultiplier base. The high voltage for each module is individually controlled and read out with a custom VME based control system (HIVOC). Each HIVOC VME control module can control up to 2048 photomultipliers. Six PbG1 SMs, 2 SM wide by 3 SM high, (144 individual PbG1 modules) are read out with a single Front End Electronics (FEE) motherboard. Figure 3.22 shows an exploded view of the lead-glass detector supermodule. The PbG1 energy resolution and timing resolution are shown in Figure 3.23 and Figure 3.24, respectively. The PbG1 pion rejection factor is shown in Figure 3.25.

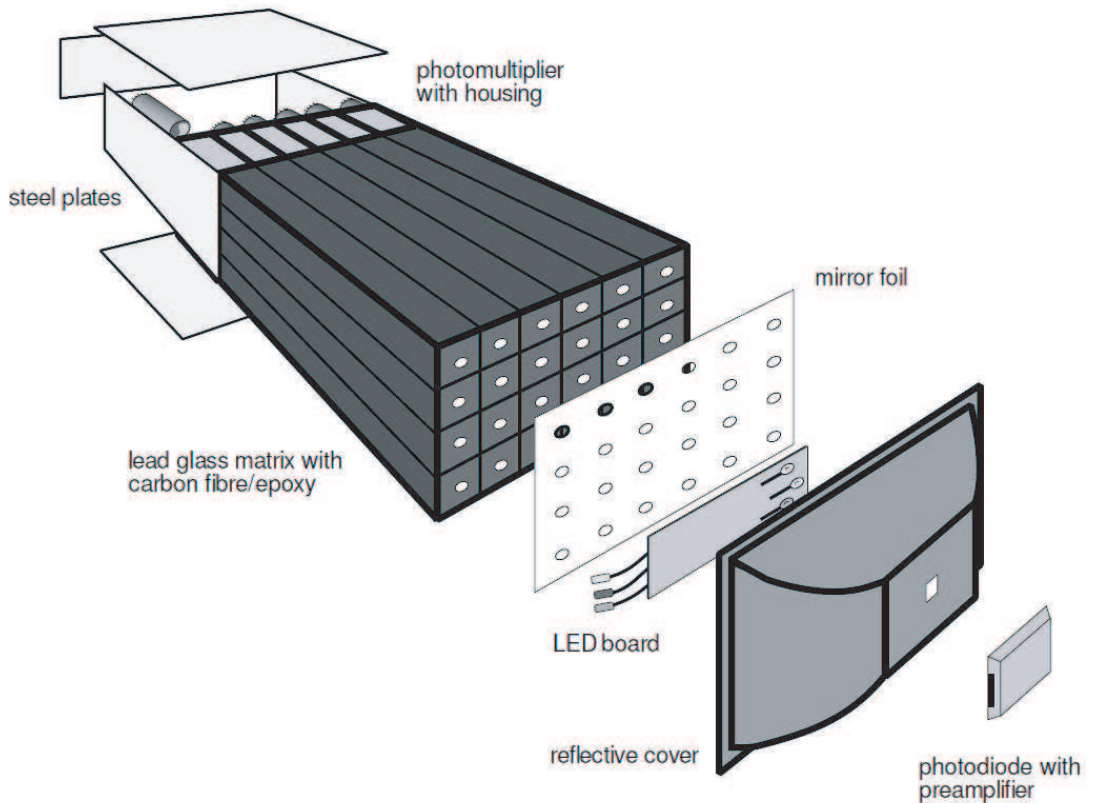


Figure 3.22: Expanded view of a lead-glass detector supermodule.

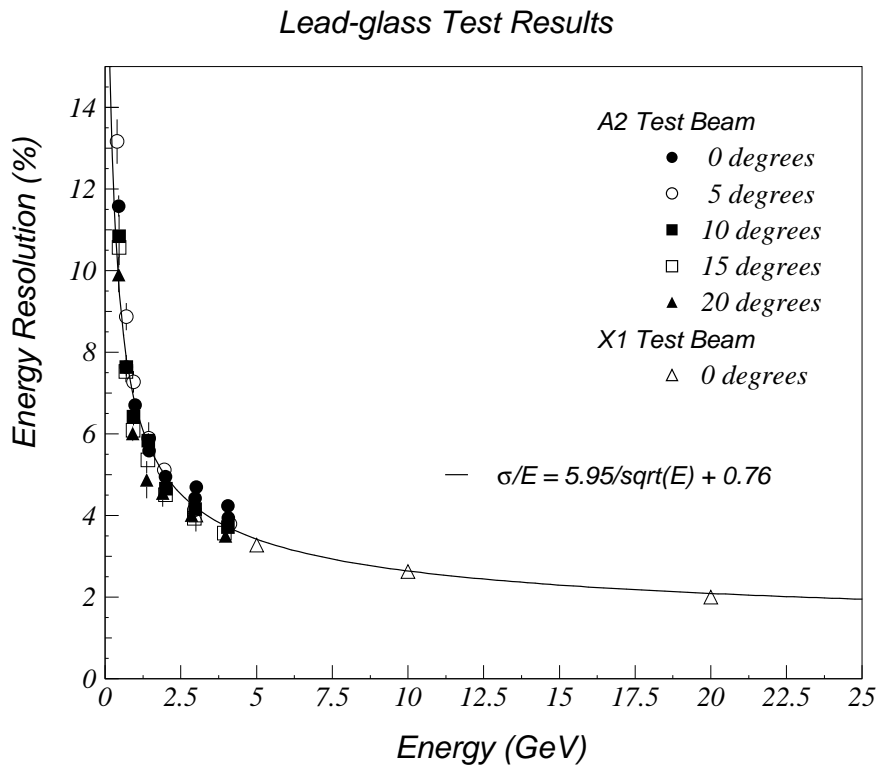


Figure 3.23: PbGl energy resolution versus incident energy.

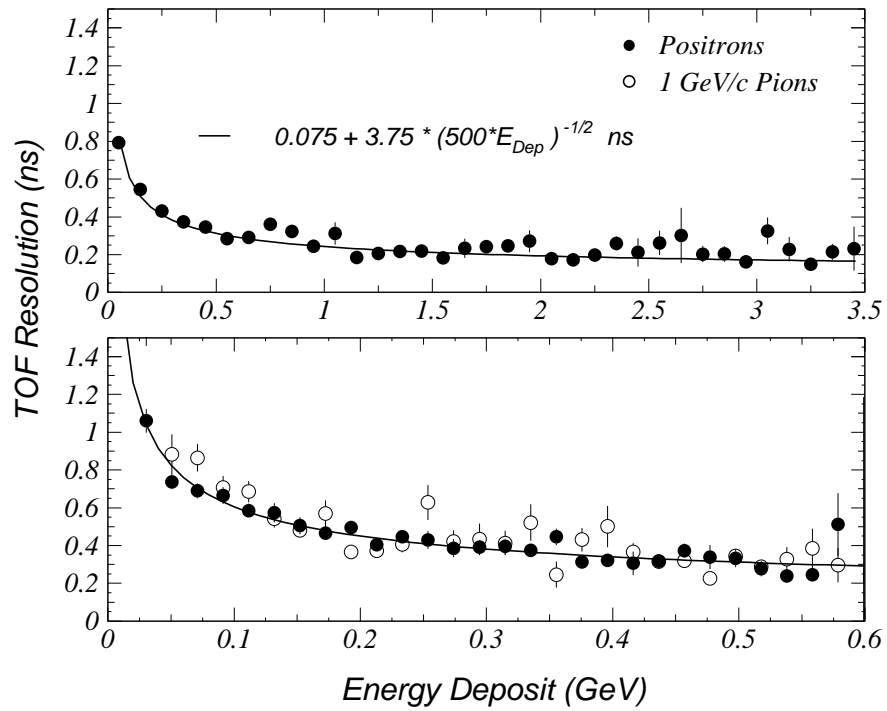


Figure 3.24: PbGl timing resolution versus energy deposit in a single module for positrons of incident momenta 0.5, 0.75, 1.0, 1.5, 2.0, 3.0, and 4.0 GeV/c and for 1.0 GeV/c pions.

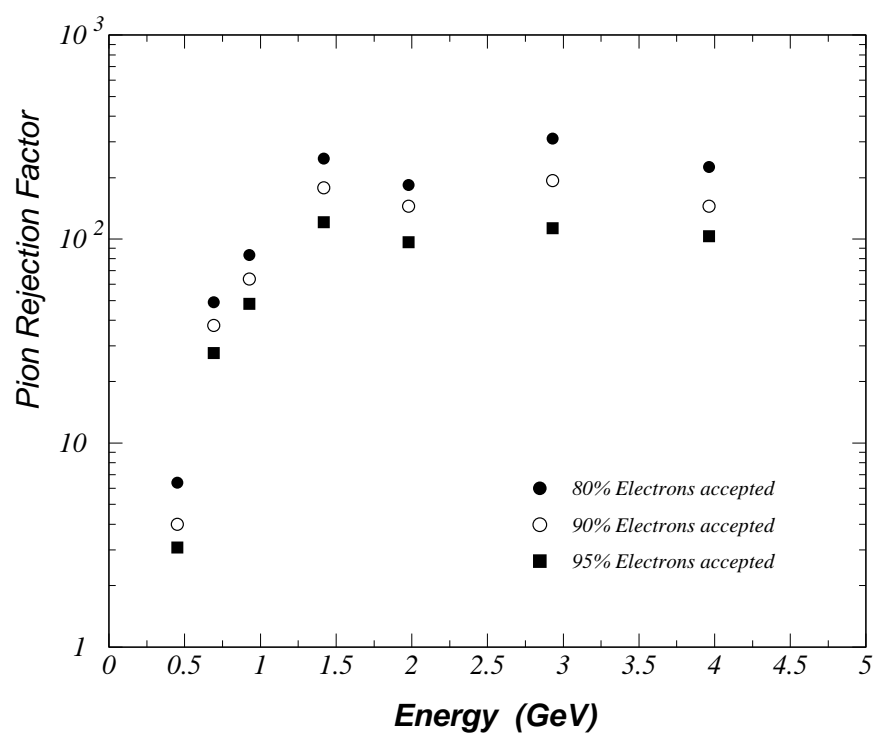


Figure 3.25: Pion rejection factor versus incident energy.

3.6.4 Shower Shape Measurement on Photon Identification

Since electromagnetic and hadronic particles produce quite different patterns of energy sharing between the calorimeter towers, second moments of the measured showers are often used to differentiate between them. However, PHENIX has introduced a model which uses an analytical parametrization of the energy sharing and its fluctuations based upon measurements of identified electrons. The parameterization is used to compute

$$\chi^2 = \sum_i \frac{(E_i^{pred} - E_i^{meas})^2}{\sigma_i^2} \quad (3.5)$$

where E_i^{meas} is the energy measured in tower i and E_i^{pred} is the predicted energy (using the parametrization and the actual measured impact point) for an electromagnetic particle of total energy $\sum_i E_i^{meas}$. This χ^2 value characterizes how “electromagnetic” a particular shower is and can be used to discriminate against hadrons. The electromagnetic shower gives a smaller χ^2 value than hadron, in general. The important new feature of this model is that the fluctuations are also parameterized. Therefore, the resulting χ^2 distribution is close to the theoretical one and it is nearly independent of the energy or the impact angle of the electron. The χ^2 distribution for 2 GeV/c electrons and pions are shown in Figure 3.26. The arrow marks the χ^2 cut corresponding to 90% electron efficiency.

The “shower profile” gives the relation between the incident position and the energy deposits in the 3x3 towers (Figure 3.27). The “shower profile” was obtained for incident electron on each tower, where the numerical values in the “shower profile” show the fractions of the energy deposits in each of the 3x3 towers of interest.

3.7 PHENIX Muon Arm

The PHENIX Muon Arms provide a means of studying vector meson production, the Drell-Yan process (via the detection of muon pairs) and heavy quark production. Z and W production will be studied at forward rapidities (via the detection of single high- p_T muons). Detection of Z and W particles produced by collisions of polarized protons will be important for determining polarization of the sea quarks $\Delta\bar{q}$.

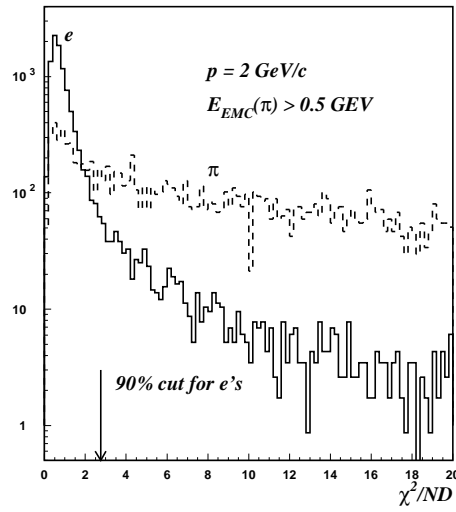


Figure 3.26: χ^2 distribution for showers induced by 2 GeV/c electrons and pions in the PbSc calorimeter.

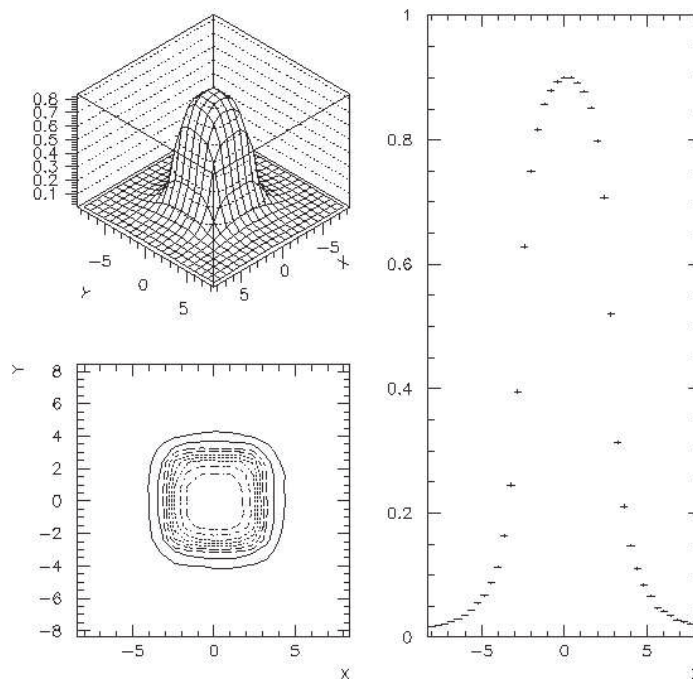


Figure 3.27: Shower profile in EMCal.

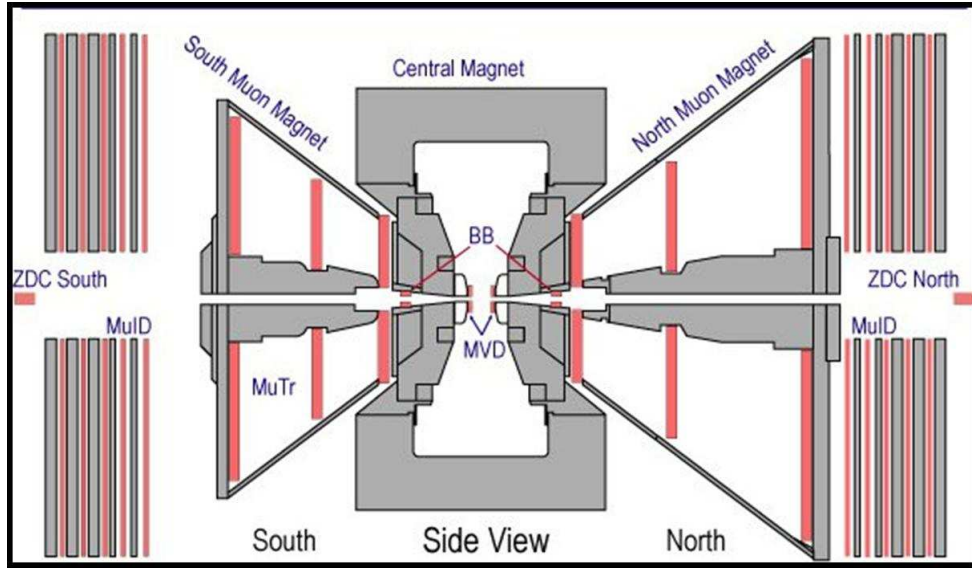


Figure 3.28: Schematic of PHENIX Muon Arm.

3.7.1 Muon Tracker (MuTr)

The relative mass resolution from the reconstruction of a muon pair is approximately given by $\sigma(M)/M = 6\%/\sqrt{M}$, where M is in GeV. This mass resolution enables a clear separation of the ρ/ω peak from the ϕ , J/ψ and ψ' , with an acceptable separation of Υ and Υ' . This is consistent with a spacial resolution of the track of $100 \mu\text{m}$. The above design requirements led to a Muon Tracker design which comprises three stations of cathode-strip read-out tracking chambers. They are mounted inside the conical-shaped muon magnets, with multiple cathode strip orientations and readout planes in each station. Test-bench measurements from production chambers and electronics combined with simulations of the full muon tracker design show that the tracker should meet the design requirements outlined above.

3.7.2 Muon Identifier (MuID)

The background of muons reaching the muon identifier (MuID) is reduced with the algorithms used to reject the larger hadron background. Of this required net μ/π separation, approximately 10^{-2} is provided by the presence of steel preceding the MuID which filters out pions. This leaves 3% as the maximum tolerable fraction of the charged pions which may subsequently be misidentified as muons.

In order to set the punch-through probability for pions of up to $4 \text{ GeV}/c$ to

be 3% or less, a total steel depth of 90 cm (5.4 hadronic interaction lengths) is required beyond the nosecone and central magnet. Subtracting the thickness of the muon magnet backplate, a total depth of 60 cm of steel is required in the MuID itself. Accordingly, a muon at the vertex must have a mean kinetic energy of at least 1.9 GeV to reach the MuID system. The mean minimum initial energy for a muon to penetrate completely through the MuID is 2.7 GeV.

Segmentation of the absorber into multiple layers improves the measurement of the trajectory in the MuID. It is desirable to have the early absorber layers be divided more finely to increase the acceptance for meson detection. The segmentation chosen is a total of four steel absorbers after the 30 cm thick muon magnet backplate of the north arm of thicknesses 10, 10, 20, and 20 cm. The 5 gaps created by the absorbers are instrumented with the MuID panels. The MuID for the south arm is identical to that for the north arm (although the muon magnet backplate is only 20 cm thick) and at the same distance from the interaction vertex.

3.8 PHENIX Data Acquisition (DAQ) System

3.8.1 DAQ Overview

PHENIX is designed to make measurements on a variety of colliding systems from p+p to Au+Au. The occupancy in the detectors varies from a few tracks in p+p interactions to approximately 10% of all the detector channels in central Au-Au interactions. The interaction rate at design luminosity varies from a few kHz for Au-Au central collisions to approximately 500 kHz for minimum bias p-p collisions. The PHENIX DAQ system [115] was designed to seamlessly accommodate improvements in the design luminosity. This was accomplished through the pipelined and deadtimeless features of the detector front ends and the ability to accommodate higher-level triggers.

In PHENIX it is necessary to measure low-mass lepton pairs and low p_T particles in a high-background environment. In order to preserve the high interaction-rate capability of PHENIX a flexible triggering system that permits tagging of events was constructed. The On-Line system has two levels of triggering denoted as LVL1 and LVL2. The LVL1 trigger is fully pipelined, therefore the On-Line system is free of deadtime through LVL1. Buffering is provided that is sufficient to handle fluctuations in the event rate so that deadtime is reduced to less than 5% for full RHIC luminosity. The LVL1 trigger and lower levels of the readout are clock-driven by beam bunch-

crossing signals from the 9.4 MHz RHIC clock. The higher levels of readout and the LVL2 trigger are data-driven where the results of triggering and data processing propagate to the next higher level only after processing of a given event is completed.

The general schematic diagram for the PHENIX On-Line system is shown in Figure 3.29. Signals from the various PHENIX subsystems are processed by Front End Electronics (FEE) that convert detector signals into digital event fragments. This involves analog signal processing with amplification and shaping to extract the optimum time and/or amplitude information, development of trigger input data and buffering to allow time for data processing by the LVL1 trigger and digitization. This is carried out for all the detector elements at every beam crossing synchronously with the RHIC beam clock. The timing signal is a harmonic of the RHIC beam clock and is distributed to the FEM's by the PHENIX Master Timing System (MTS). The LVL1 trigger provides a fast filter for discarding empty beam crossings and uninteresting events before the data are fully digitized. It operates in a synchronous pipelined mode, generates a decision every 106 ns and has an adjustable latency of some 40 beam crossings.

Once an event is accepted, the data fragments from the FEM's and primitives from the LVL1 trigger move in parallel to the Data Collection Modules (DCM). The PHENIX architecture was designed so that all detector-specific electronics end with the FEM's, so that there is a single set of DCM's that communicate with the rest of the DAQ system. The only connection between the Interaction Region (IR) where the FEM's are located and the Counting House (CH) where the DCM's are located is by fiber-optic cable. The DCM's perform zero suppression, error checking and data reformatting. Many parallel data streams from the DCM's are sent to the Event Builder (EvB). The EvB performs the final stage of event assembly and provides an environment for the LVL2 trigger to operate. In order to study the rare events for which PHENIX was designed, it is necessary to further reduce the number of accepted events by at least a factor of six. This selection is carried out by the LVL2 triggers while the events are being assembled in the Assembly and Trigger Processors (ATP) in the EvB. The EvB then sends the accepted events to the PHENIX On-line Control System (ONCS) for logging and monitoring. The technology used to control the many components that must work together to successfully accumulate the data is the Common Object Request Broker Architecture (CORBA) system. CORBA makes it possible to transparently access objects on remote computers of various types throughout the network. The main control process called Run Control (RC) accesses and communicates with remote objects which in turn control a given piece of hardware. The RC process determines the configuration of the whole DAQ

front-end.

3.8.2 Front-end Electronics Module for EMCAL

The readout electronics for the EMCAL system conform to the general PHENIX Front-End Electronics (FEE) scheme which includes periodic sampling synchronous with the RHIC RF clock and pipelined, deadtime-less conversion and readout. This section describes those features unique to the EMCAL readout electronics and the way in which they satisfy the needs of the physics measurements made with the EMCAL detector. On every event, for either physics or calibration data, each EMCAL PMT emits a negative current pulse and each of these is processed by a chain as shown in Figure 3.30. The salient features of the chain are discussed below.

There is no preamp or shaping stage other than passive integration. The 93 ohm resistor terminates the signal line from the PMT so the voltage profile at point A in Figure 3.30 simply follows the current profile from the PMT which is a pulse with rise time less than 5 nsec. The charge is collected onto the 500pF capacitor so the voltage profile at point B in Figure 3.30 follows the integral of the current. The current pulse is a step function with a ~ 100 ns rise time. The large resistor sets the quiescent voltage at this stage to +4 V to allow for negative-going pulses.

The fast voltage pulse discussed above is the “timing signal” that is used to measure the arrival time of the EM shower in the detector. During the pulse integration process a voltage step function is generated whose height is proportional to the total charge collected and thus the energy collected during the time window of the event. All of the remaining analog processing stages up to ADC conversion are carried out within an ASIC chip, as illustrated in Figure 3.30. This chip was custom designed for the EMCAL system. Each of these ASIC chips services four PMT channels and also contains the circuitry for the fast trigger function which is described below.

In the arrival time measurement the voltage pulse is discriminated, either in a leading-edge mode or a constant-fraction mode. The choice of mode, as well as the threshold voltages, are remotely selected in situ via ARCNet which is the system used for monitoring and slow control of the PHENIX FEM's. The discriminator ring starts a voltage ramp generator. The ramp is stopped on the next edge of the RHIC clock providing a common-stop mode TAC for each channel. After stopping, the ramp voltage is held for two clock cycles where it settles and is then sampled and converted in the AMU/ADC stage. The final reported ADC value then varies linearly with the pulse arrival time. The relationship between time and the resulting ADC output voltage can be adjusted by programming the ramp slope and offset voltage remotely via

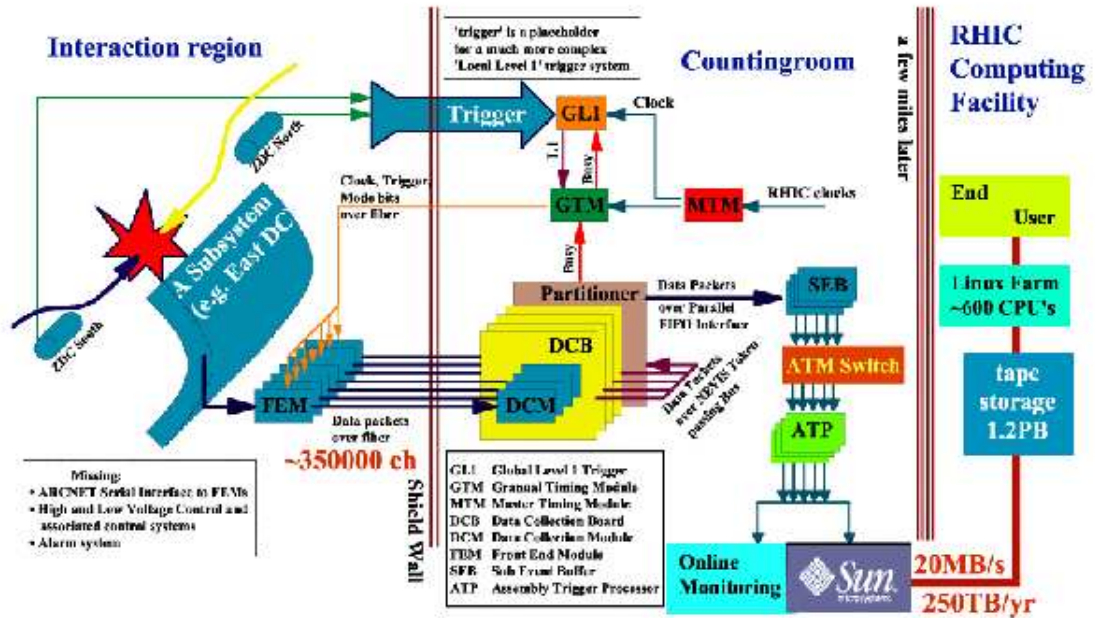


Figure 3.29: Schematic diagram of the PHENIX On-Line system.

ARCNet.

The energy signal is first put through a Variable Gain Amplifier (VGA). Each PMT channel has its own VGA and each of whose gains can be set remotely in the range $\times 4$ - $\times 12$ with 5-bit resolution. This allows the readout electronics to compensate, to within a few percent over its range, for gain variations among PMT's which share the same high voltage supply. Uniform response for the energy signal is useful in the performance of the trigger circuit. It is also useful in general for maximizing the use of the ADC dynamic range for all channels.

The dynamic range of physics signals from the EMCal is quite large and the detector is expected to resolve energy deposits from 20 MeV up to 15-30 GeV with a noise contribution from the electronics of no more than 0.1% for large signals and 5 MeV for small signals. This range is impossible to cover with a single 12-bit ADC conversion. Thus the energy signal is converted twice with two different levels of amplification. The "low gain" signal is converted straight from the VGA and the "high gain" signal is converted separately after a second stage of $\times 16$ amplification.

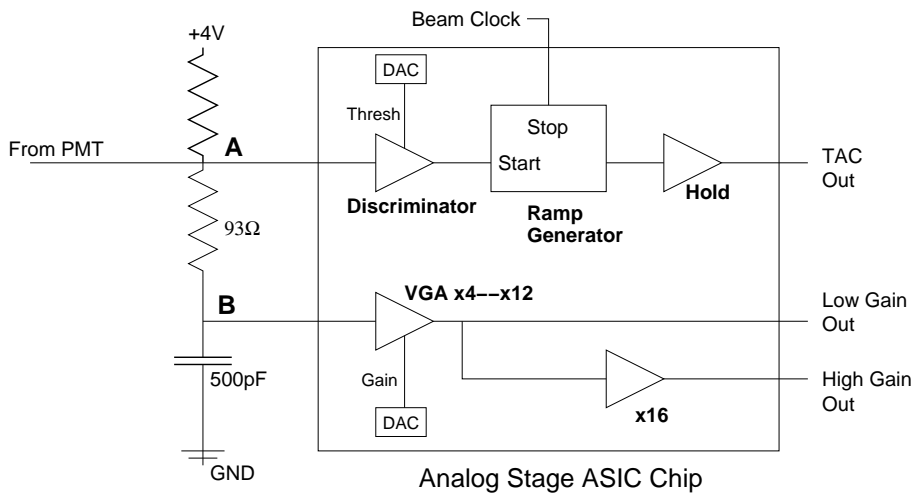


Figure 3.30: Block diagram of the energy and timing measurement circuits.

3.8.3 Level 1 Trigger

At design luminosities, the rate of basic interactions in both p-p and A-A running in RHIC is too high for PHENIX to digitize and record all events. Since it is an explicit goal of PHENIX to use the full available luminosity to measure rare processes such as the production of heavy flavors and very high

energy secondaries, an ability to trigger on such processes is necessary. The EMCAL FEE provides a fast-trigger function intended to signal the presence of a high-energy shower in the EMCAL detector. Electromagnetic showers with a large energy deposit (generally taken as above several GeV) are natural indicators of several kinds of interesting rare events, including high-energy photons and neutral mesons as well as high-energy electrons from heavy-flavor decays.

A traditional approach for a high-energy cluster trigger in a laterally segmented calorimeter is to make a fast analog sum of a group of towers and discriminate that sum against a threshold. In the simplest scheme each tower contributes to only one sum leaving the summed trigger groups disjointed. This arrangement has the drawback that the effective threshold is position dependent since showers which spread across more than one group need to have a much higher energy than those contained within one group.

The PHENIX EMCAL fast trigger avoids this problem by summing over non-disjoint overlapping groups of towers. The design is illustrated in Figure 3.31. Groups of 2x2 towers are served by one ASIC chip described above. Within each ASIC the four analog PMT signals are summed creating an array of disjoint 2x2 sums. To negate the influence of “hot” PMT’s, each channel in each ASIC can be masked out of the sum individually by remote ARC-NET control. Each ASIC relays copies of its signal generated by summing the current to three immediate neighbors. These are relayed between FEM’s at supermodule boundaries making the trigger circuitry effectively seamless. Each ASIC also receives three signals from its neighbors and combines them with its own to form a 4x4 sum. The entire circuitry then produces 36 overlapping 4x4 sums in each FEM. Within each ASIC the 4x4 sum signal is compared to three separate thresholds, each remotely programmable, to provide extra flexibility for different physics processes.

Run	ERT 4x4a	ERT 4x4b	ERT 4x4c	ERT 2x2
86768	2.1GeV	2.8GeV	1.4GeV	800MeV
87618	2.1GeV	2.8GeV	1.4GeV	400MeV
89463	2.1GeV	2.8GeV	1.4GeV	800MeV

Table 3.5: The table of ERT trigger thresholds in RUN2003.

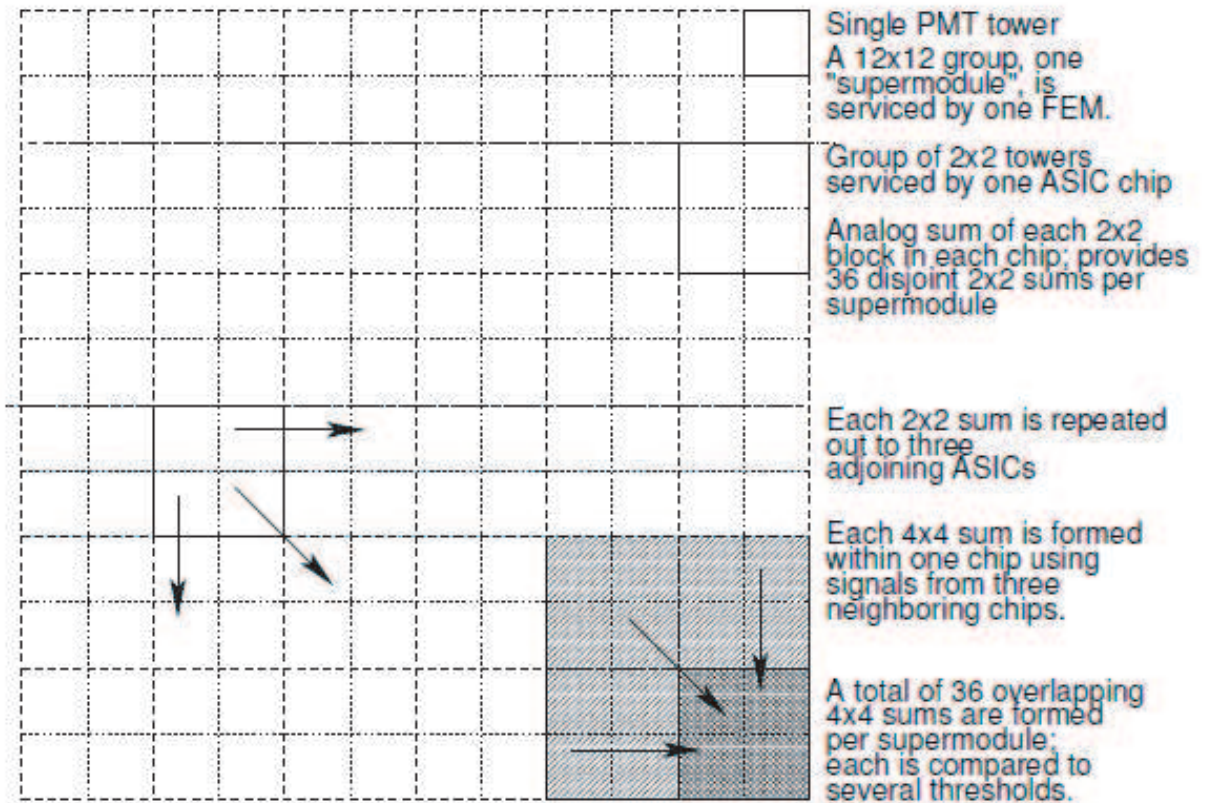


Figure 3.31: Schematic pattern of the EMCAL fast trigger summing operation.

Chapter 4

Analysis

4.1 Outline of Analysis

In this section, the outline of the analysis of prompt photon is introduced. The invariant cross section is obtained from the corrected prompt photon yield N_γ^{corr} and the luminosity L as follows:

$$E \frac{d^3\sigma}{dp^3} = \frac{1}{2\pi} \cdot \frac{1}{L} \cdot \frac{N_\gamma^{corr}}{p_T \cdot dp_T}. \quad (4.1)$$

The corrected prompt photon yield N_{gamma}^{corr} is obtained from the raw prompt photon yield N_{gamma}^{raw} as follows:

$$\begin{aligned} N_\gamma^{corr} &= N_\gamma^{raw} \\ &\times 1/\epsilon^{acc\&smearing} \\ &\times 1/\epsilon^{highp_T} \\ &\times 1/\epsilon^{BBCbias} \\ &\times 1/\epsilon^{conversion} \end{aligned} \quad (4.2)$$

Each of corrections ϵ is explained later. First, the run and trigger selection is described in Section 4.2. The energy calibration for EMCal is important for correcting the photon yield. The time of flight of photon calibration of EMCal is needed to reduce the hadron background for photon yield. Moreover, the condition of EMCal, hot and dead channels, is critical for the measurement of photon yield. They are discussed in Section 4.3. In Section 4.5, the extraction of π^0 yield is described. It is very important to discuss the details of π^0 , because the photons from π^0 decay are the main background source for prompt photon measurement. The other background sources, such as

photons from η , η' and ω decay, charged particles, neutral particles, photons from non-vertex origin are discussed in Section 4.6, Section 4.7, Section 4.8 and Section 4.9, respectively. The photon conversion correction is explained in Section 4.10. The High- p_T trigger efficiency and the trigger bias of the minimum bias trigger are described in Section 4.11 and Section 4.12. The acceptance and smearing correction are explained in Section 4.13. Finally, the prompt photon cross section and systematic errors are presented in Section 4.14.

4.2 Run and Trigger Selection

In proton-proton collisions in RUN2003, the PHENIX collected 35TByte data as a PRDF (PHENIX Raw Data File) format. The number of PRDF, whose size is 1.5GByte, is about 12000. 941 DST (Data Summary Tape) files were made from PRDF. The run number which corresponds to the DST during the proton-proton collisions in RUN2003 is from 86219 to 92446. Due to the High- p_T trigger condition, the run before 87791 cannot be used in this analysis. The ERT 4x4c trigger is chosen as a high- p_T trigger. The events which have vertex within ± 30 cm in z are chosen. Figure 4.1 shows an example of BBC z -vertex distribution in run 87991.

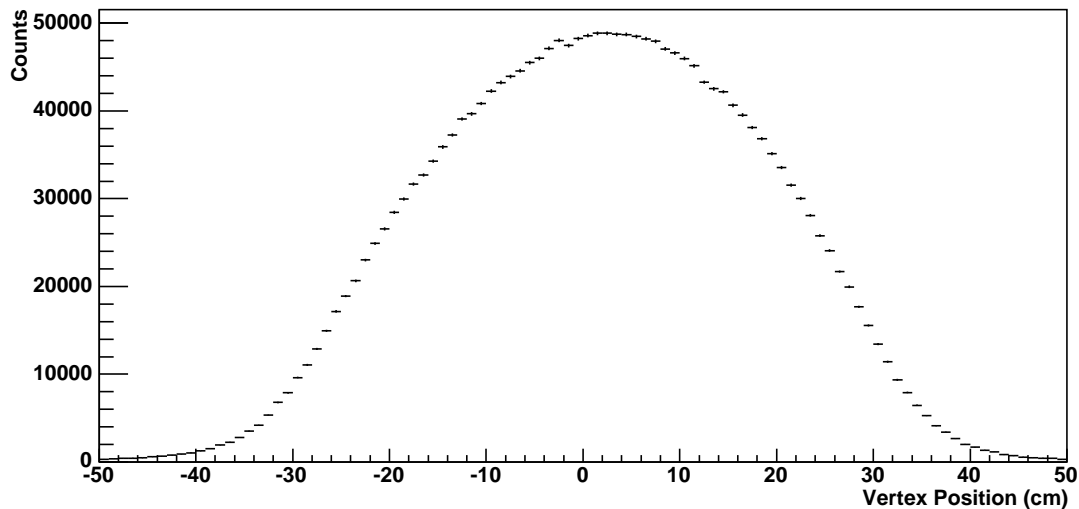


Figure 4.1: The vertex position distribution of BBC in run 87991.

4.3 Calibration of EMCal

4.3.1 Quality Assurance of EMCal

The condition of EMCal, “hot” and “dead” channels, is critical for the measurement of photon yield. The “hot” and “dead” channels are needed to be removed in this analysis. The map of “hot” and “dead” channels have a dependence on run and energy. Figure 4.2 shows an example of the number of hits for each channel in one sector for the photon energy between 3.0 GeV and 4.0 GeV (a) and for run between 87791 and 89211 (b). The fitting function used is Gaussian as follows;

$$f(x) = p[0] \exp\left(-\frac{(x - p[1])^2}{2p[2]^2}\right) \quad (4.3)$$

where x is the number of hits for each channel, $p[i]$ ($i = 0, 1, 2$) is the parameters. The condition of “hot” channel is defined as follows;

$$x > p[1] + 5 \times p[2]. \quad (4.4)$$

The “hot” channels are represented as color filled histograms in Figure 4.2. They and 3x3 channels in their neighborhood are removed in this analysis because the 3x3 channels in the neighborhood are used clustering when the photon hits in the center channel. The “dead” channels are defined such that the number of hits for each channel is 0 during the whole run period. Moreover, channels on the edge of EMCal is not used due to energy leak of clusters. As discussed in Section 4.3.3, the channels whose Time of Flight distribution is not normal are also removed. Figure 4.3 shows “hot” and “dead” map for all EMCal sectors. The colored area represents “hot” or “dead” channels. The number of removed channel is 2985, this corresponds to 12% of all the channels.

4.3.2 Energy Calibration

The EMCal energy calibration in Run2003 was done using the data sets from d-Au and p-p collisions. There are three methods which are used for PbSc calibration: the π^0 method, the MIP (Minimum Ionizing Particle) method, and the electron method. 12295 towers are calibrated using the π^0 method, 1730 towers are calibrated using the MIP method, 187 towers are calibrated using the electron method, remaining towers are not calibrated. The PbGl towers are calibrated using only the π^0 method. 8547 towers are calibrated.

When a photon deposits the energy as an electromagnetic shower or a charged particle penetrates with an ionization energy loss throughout the

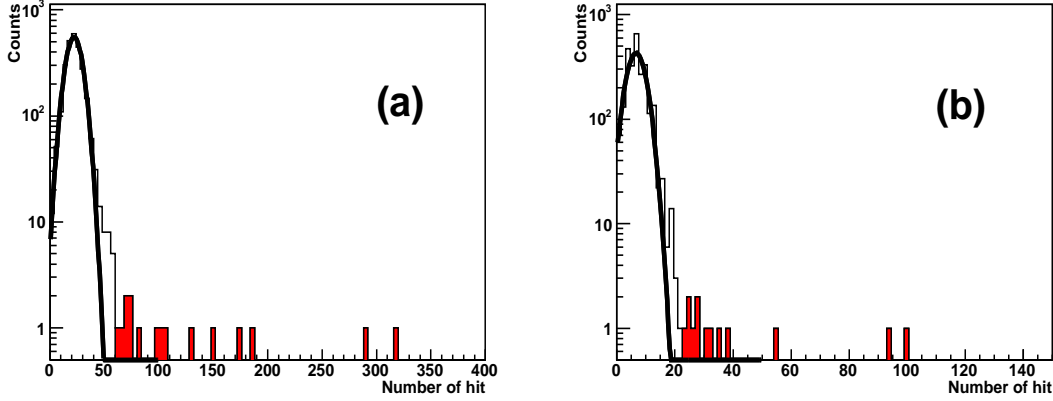


Figure 4.2: The number of hits for each channel in one sector (W0) for photon energy between 3.0 GeV and 4.0 GeV is shown in (a). The number of hits for each channel in one sector (W0) for run between 87791 and 89211 is shown in (b). The color filled bins are removed as a hot channel.

calorimeter, 80% and 60-100% of the photon energy or the ionization energy are observed only by one tower, which we call “Maximum Tower”. Tower is a module of EMCAL. The fraction of the measured energy in the “Maximum Tower” depends on the incident position and the incident angle. When the clusters were found around the “Maximum Tower”, its ionization energy or π^0 mass peak was shifted to the correct value. The correct value of ionization energy is 270 MeV and π^0 mass is 135 MeV. The shift is assumed to be due to miss-calibration of the tower. The ionization energy and π^0 mass peak are shown in Figure 4.4 and Figure 4.5, respectively. A correction for the shift into the tower is applied, and then the clustering algorithm is applied over them. This procedure is repeated. The iterative fitting and re-clustering are necessary. Figure 4.4 and Figure 4.5 show the MIP peak and π^0 mass peak in a particular tower, in W0 sector 63rd from left edge and 13th from low edge which is denoted as (63,13). Figure 4.6 shows the diagram of such iterative work. The final correction factor for towers will be the product of all correction factors, $C1 \times C2 \times \dots$. Figure 4.7 and Figure 4.8 show the deviation of the MIP peak and π^0 peak in several iterations in W0 sector. The distribution of deviations become narrow after the iteration.

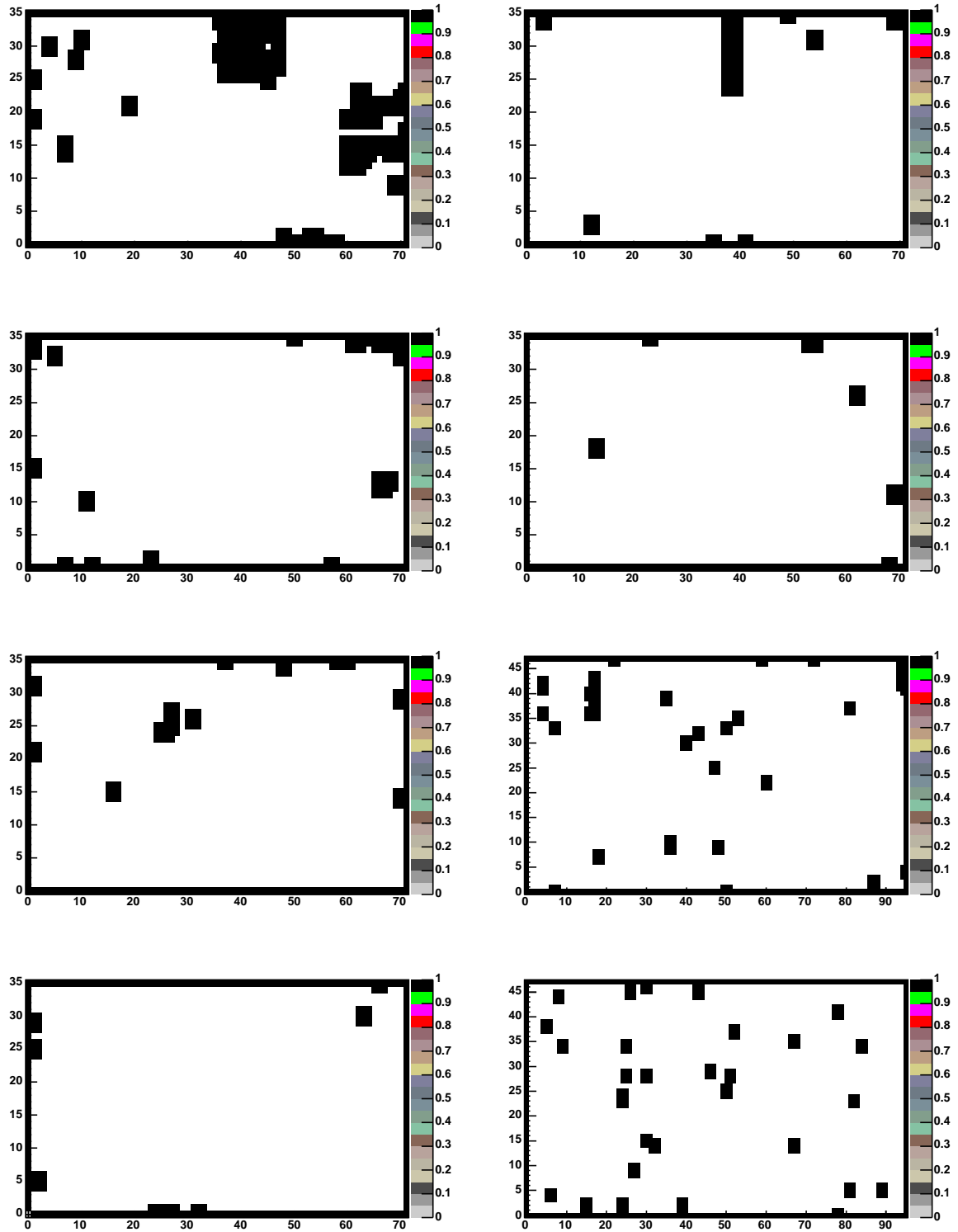


Figure 4.3: Hot and dead tower map. Top left is W3 and top left is E3. The black area is removed in this analysis.

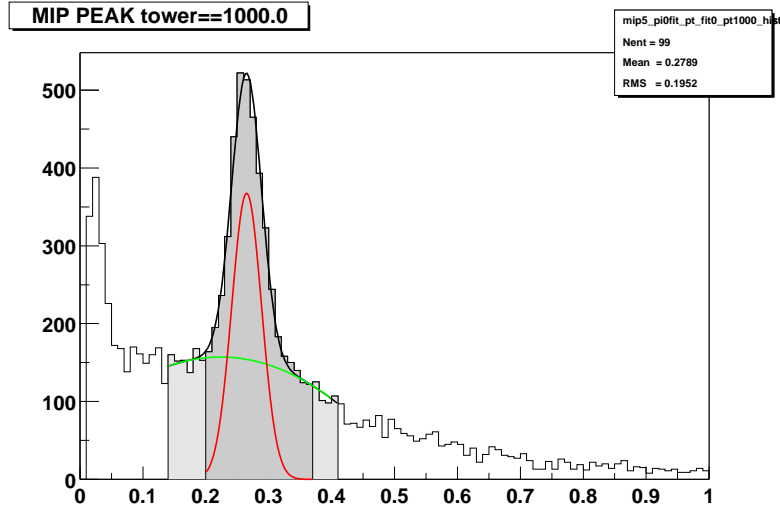


Figure 4.4: Deposited energy $\times 1/\cos(\theta)$ distribution by charged particles with more than 0.4 GeV/c, when cluster has its maximum tower in (63,12) in W0 sector.

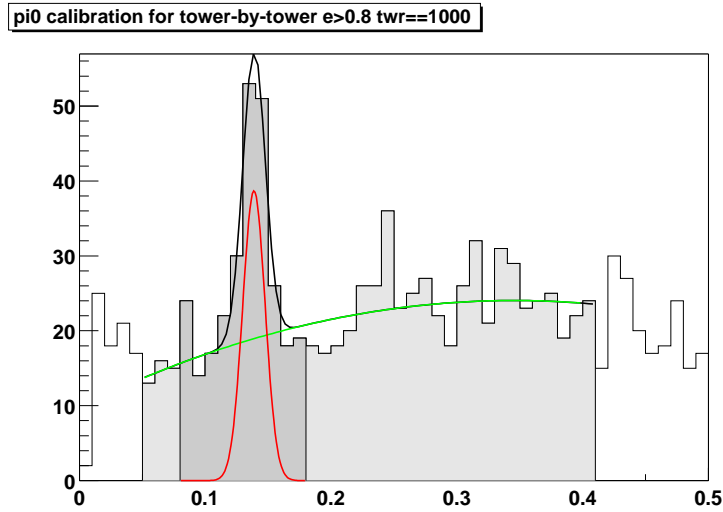


Figure 4.5: Invariant mass distribution with p_T of more than 1.0 GeV/c when one of two clusters have its maximum tower in (63,13) in W0 sector.

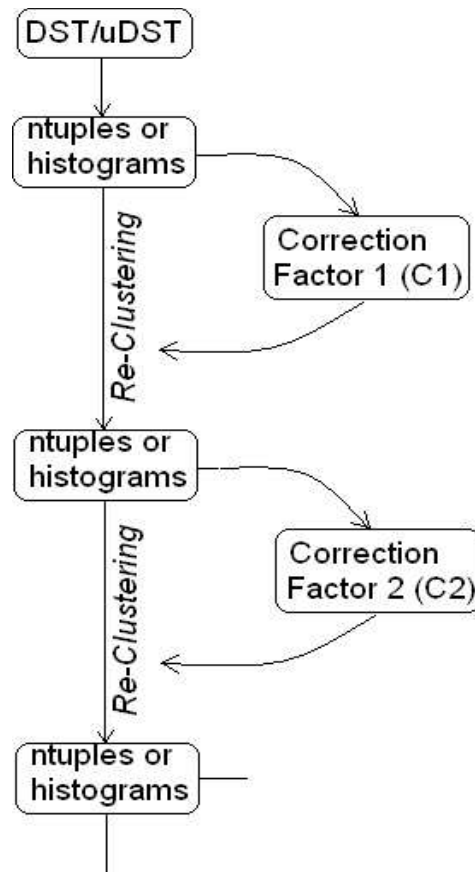


Figure 4.6: Diagram of the basic procedure of energy calibration and its iterative work. The final correction factor is the product of all the correction factor.

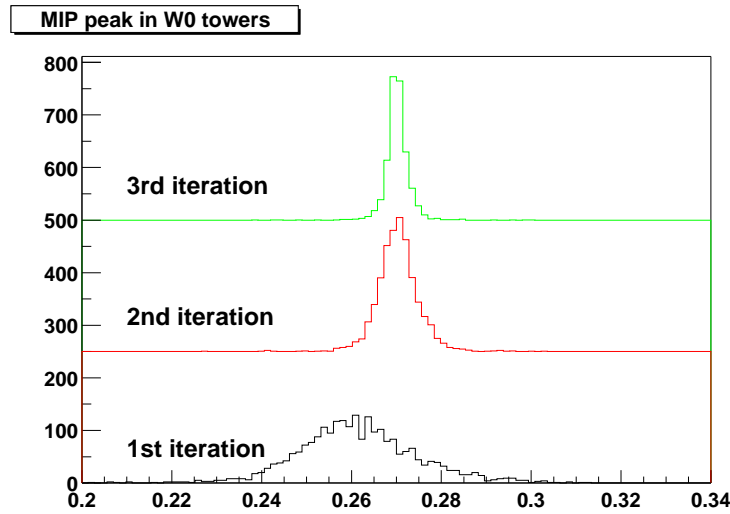


Figure 4.7: Deviation of the MIP peak in 1st (black bottom), 2nd (red middle), and 3rd (green middle) iteration in W0 sector. The correction factors for a tower, named as C1 to C3 respectively, are defined as the ratio between the expected MIP energy and the observed MIP peak. The final correction is the product of all the factors.

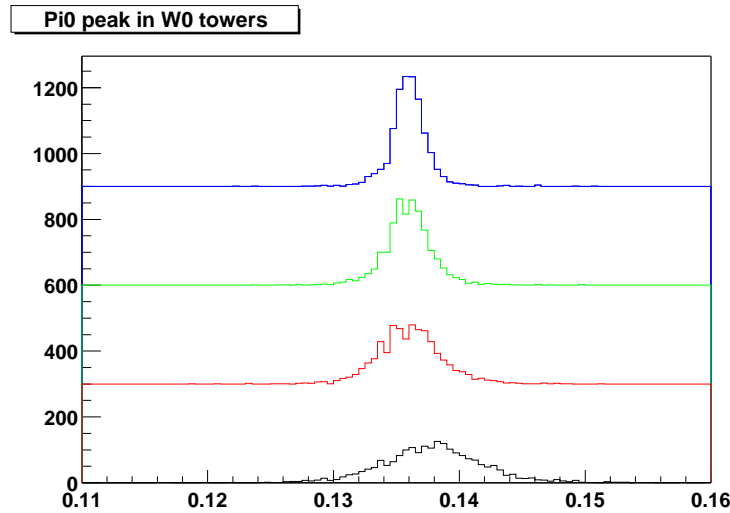


Figure 4.8: Deviation of the π^0 peak in 1st (black bottom), 2nd (red middle), 3rd (green middle), and 4th (blue top) iteration in W0 sector. The correction factors for a tower, named as C1 to C4 respectively, are defined as the ratio between the expected π^0 energy and the observed π^0 peak. The final correction is the product of all the factors.

4.3.3 Time of Flight Calibration

Before applying the TOF cuts to reject non-photon contributions, the calibration has been done. The EMCal TOF is calculated as follows;

$$EMCal\ TOF = TOF_{measured} - \frac{l}{c} \quad (4.5)$$

where $TOF_{measured}$ is real TOF, l is the distance from the vertex position to the hit position of EMCal and c is the velocity of light. Therefore, EMCal TOF distribution has a peak of photon around 0 nsec. Figure 4.9 shows an example of the distribution of TOF of one tower. When the peak value of the TOF distribution is obtained, the peak is shifted to 0 nsec. The shifted value is assumed to be due to miss-calibration. Figure 4.10 shows TOF peak distributions of each tower in PbSc and PbGl with values in DSTs. The TOF offset is evaluated for each tower. Towers whose TOF value are outside ± 10 nsec are not calibrated. In the high energy region, it is also seen that distortion depends on its energy. Figure 4.11 shows their peak position as a function of the cluster energy. A function is used to handle this dependence. The function form is as follows;

$$f(E) = p[0] - p[1] \times \exp\left(-\frac{(E - p[2])^2}{2p[3]^2}\right) \quad (4.6)$$

where $p[i](i = 1, 2, 3)$ are parameters for the fitting function. The energy dependence of TOF is corrected for by using this function.

4.4 Photon Cluster Selection

In order to select photon clusters in EMCal, TOF cut and photon shape cut are applied. TOF cut is applied for PbSc up to 10 GeV which corresponds to photon energy with the following condition;

$$|TOF| < \pm 2(\text{nsec}). \quad (4.7)$$

Because the statistics is not enough to calibrate TOF for clusters with energy more than 10 GeV, TOF cut is not applied for this energy region. There are many bad TOF towers in PbGl. TOF cut is not applied for PbGl.

Photon shape cut is then applied. Photon shape cut for PbSc is called “photon probability cut” and for PbGl is called “dispersion cut”, because of different algorithms used for both calorimeters. The photon probability

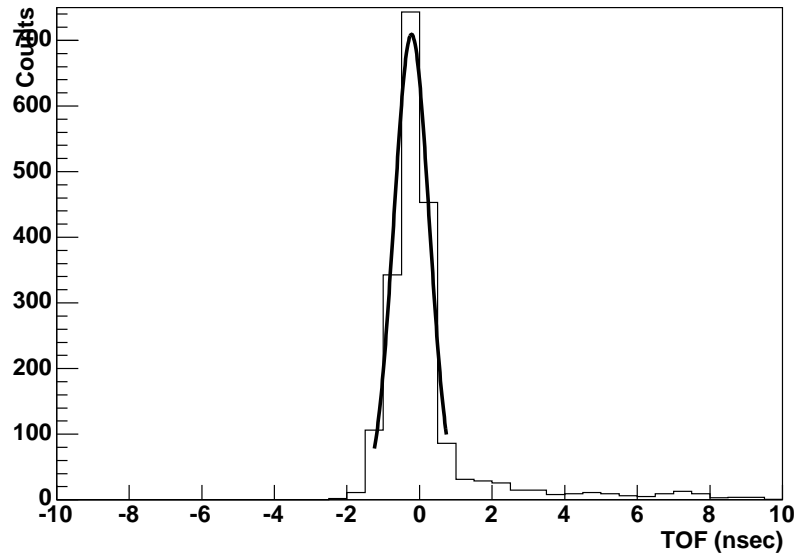


Figure 4.9: TOF distribution for one tower.

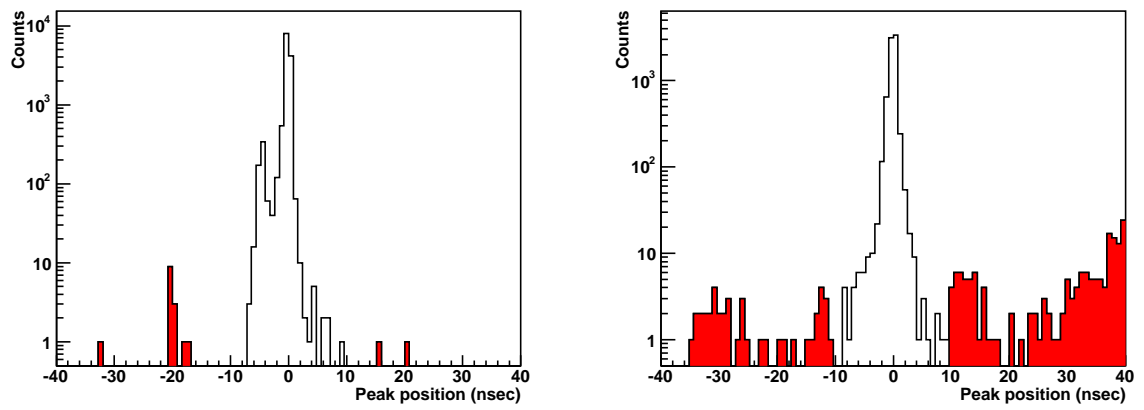


Figure 4.10: TOF peak distributions for PbSc (left) and PbGl (right). The left figure has double peak.

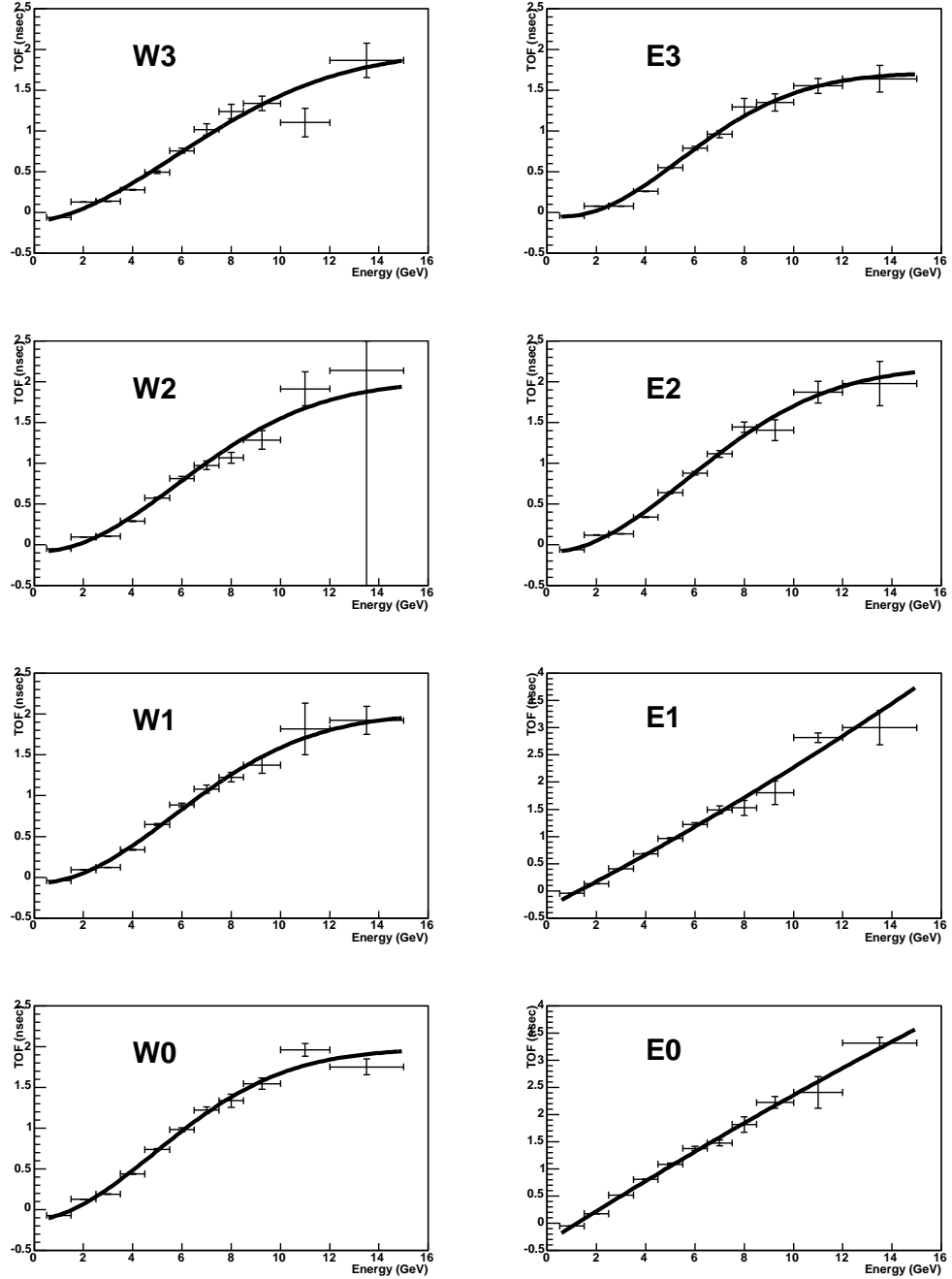


Figure 4.11: Functions to describe energy dependence of TOF.

means that χ^2 of clustering is normalized by normal χ^2 distribution. Photon shape cut is applied with the following condition;

$$\text{photon probability cut} > 0.02 \quad (4.8)$$

$$\text{dispersion cut} < 1 \quad (4.9)$$

The efficiency of this cut is checked using photons requiring its π^0 partner ($M_{\gamma\gamma} = 0.135 \pm 0.03 \text{ GeV}/c^2$, $|E_1 - E_2|/(E_1 + E_2) < 0.8$). Figure 4.12, Figure 4.13, and Figure 4.14 show the ratio of photons with the photon shape cut to those without cut in each EMCAL component. From this check, the efficiency of “photon probability cut” and “dispersion cut” is $98 \pm 1\%$ independent of p_T for both arms.

The window of the TOF cut ($\pm 2[\text{ns}]$) is large enough to contain all photon clusters. No efficiency correction is applied on this cut.

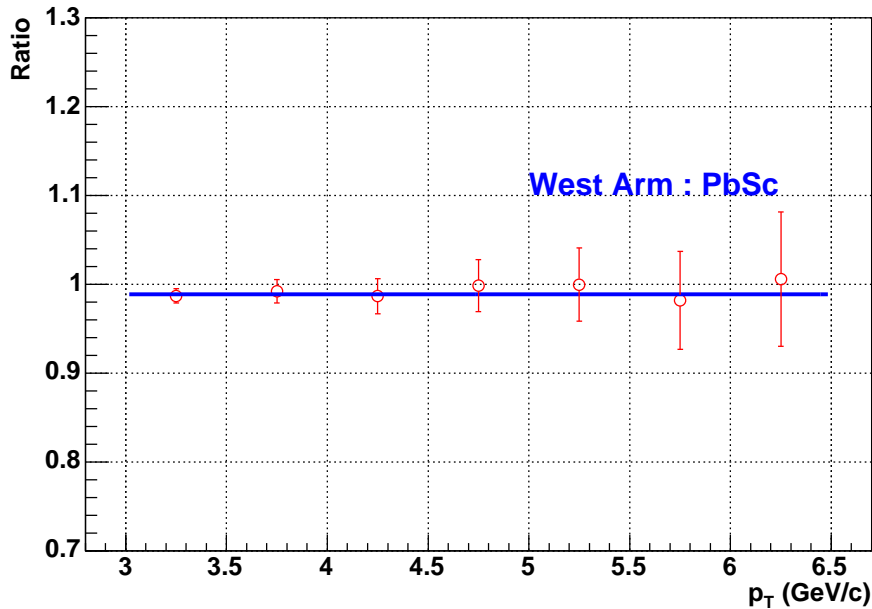


Figure 4.12: Photon shape cut efficiency in PbSc (west).

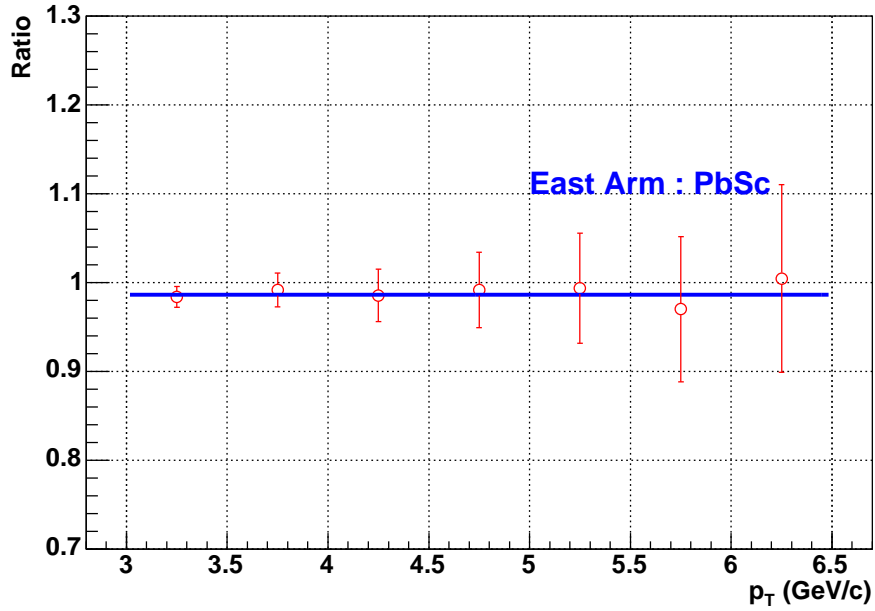


Figure 4.13: Photon shape cut efficiency in PbSc (east).

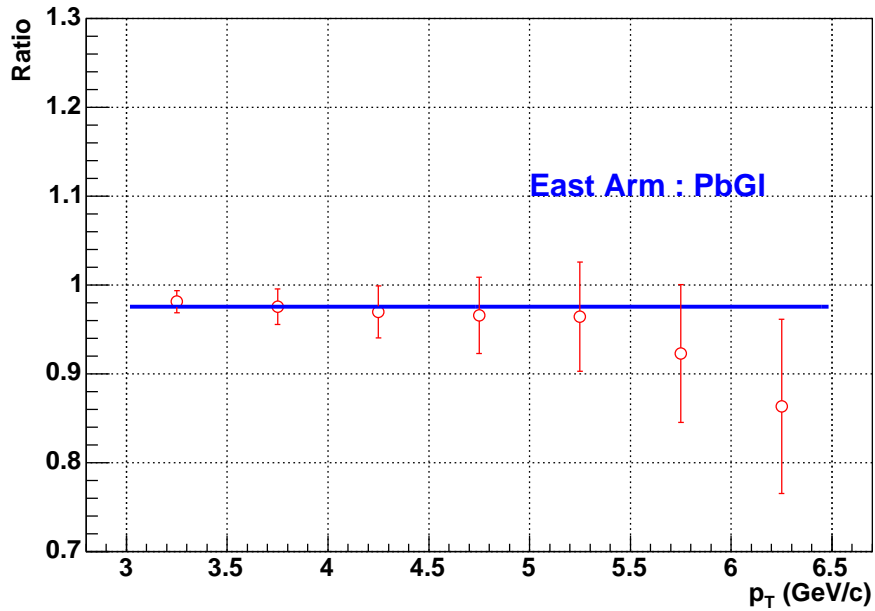


Figure 4.14: Photon shape cut efficiency in PbGl (east).

4.5 π^0 yield Extraction

4.5.1 Fiducial Area

The main background for prompt photon is from π^0 decay. To maximize the probability of reconstruction of π^0 , 12(16) of PbSc(PbGl) towers from the arm edge were used only for searching the partner of π^0 decay photon as shown in Figure 4.15. With this veto region, the second photon from π^0 decay can be found with 95% probability at 5 GeV/c.

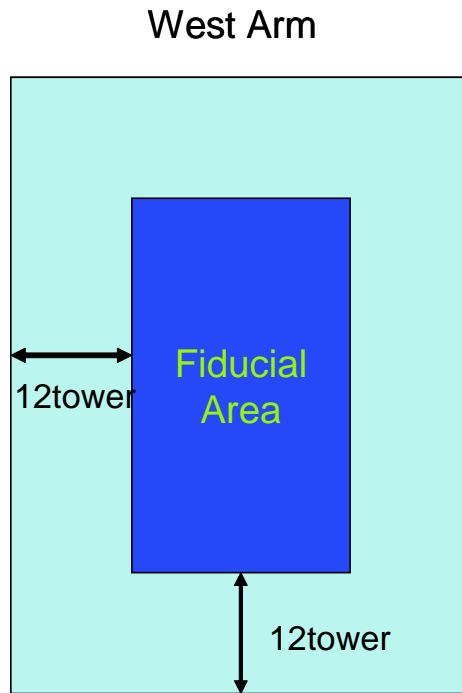


Figure 4.15: Fiducial area is shown. The towers from the arm edge is used as a veto region.

4.5.2 π^0 Reconstruction

When the two photons from a π^0 decay are detected by EMCal, π^0 mass is calculated as follows;

$$m_{\pi^0} = 2\sqrt{E_1 E_2 \sin^2\left(\frac{\phi}{2}\right)} \quad (4.10)$$

where E_1 and E_2 are the energies of the two photons from a π^0 decay, and ϕ is the opening angle between the two photons from π^0 decay. Figure 4.16 shows an example of π^0 mass distribution. The blue region is π^0 mass window. The green region is used for fitting of combinatorial background. The minimum energy of partner photon is 150 MeV. This is called E_{min} cut. The fitting function used is as follows;

$$f(x) = p[0] \exp\left(-\frac{(x - p[1])^2}{2p[2]^2}\right) + p[3] + p[4]x + p[5]x^2 \quad (4.11)$$

where $p[i](i = 0, \dots, 5)$ are the parameters of the fit. The polynomial function in this expression is used to subtract the combinatorial background. The π^0 signal is obtained after subtraction of combinatorial background inside π^0 mass window. Figure 4.17 and Figure 4.18 show π^0 mass spectrum for all p_T region. In the high p_T region ($p_T > 6.5\text{GeV}/c$), there is not enough statistics for fitting. Therefore, the signal of π^0 evaluated from the ratio of signal to background for low p_T region ($p_T < 6.5\text{GeV}/c$) was used. Figure 4.19 and 4.20 shows the fraction of π^0 photon signal in West and East Arm, respectively. The fraction is about 0.7 for both arm.

4.5.3 Tool of EMCal Detector Simulation

The π^0 partner photons can be lost as discussed in Section 4.5.4. This efficiency is obtained using a Monte-Carlo simulation of the calorimeter. This simulation is called ‘‘FastMC’’. The FastMC is not like the GEANT [122] simulation, but is a simulation in which the detector response is parameterized according to the performance during the run. The FastMC is written to simulate the initial conditions of π^0 and the calorimeter performance. This FastMC includes the following initial conditions;

- Vertex distribution ; a gaussian distribution of 80 cm width based on the measured vertex distribution and with a ± 30 cm cut.
- p_T distribution ; a formula fitted to the obtained cross section spectrum.
- Pseudo rapidity (η) and azimuthal angle (ϕ) distribution ; flat distribution within $|\eta| < 0.5$ and $0 \leq \phi \leq 2\pi$.
- π^0 decay ; isotropic decay into two photons in the rest frame of π^0 .

The FastMC includes the following effects in the EMCal: acceptance, energy scale, energy non-linearity, energy resolution, and position resolution.

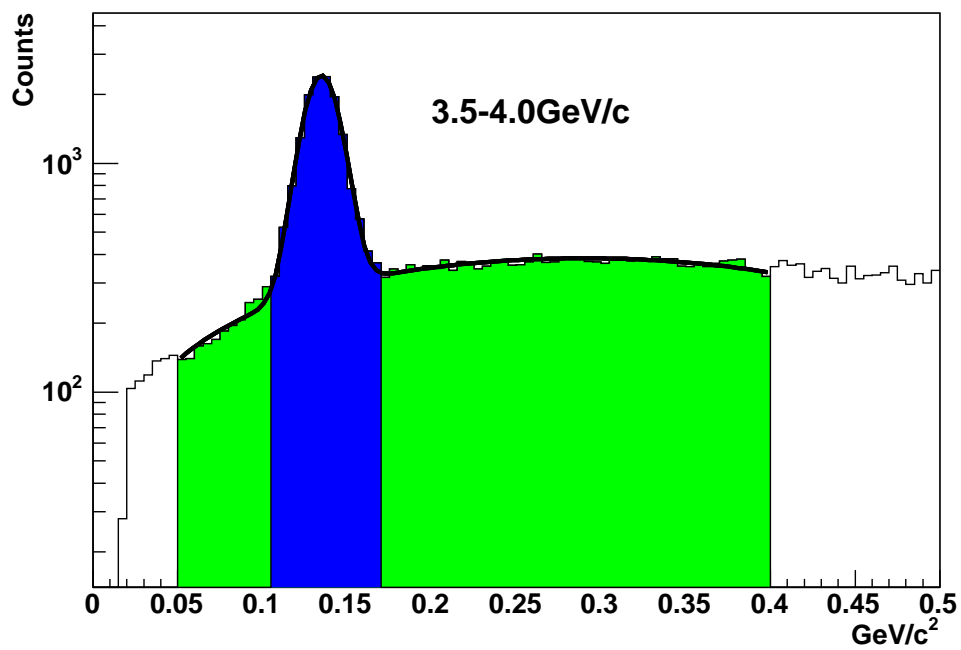


Figure 4.16: An example of π^0 mass distribution. The blue region is π^0 mass window. The green region is used for fitting of combinatorial background.

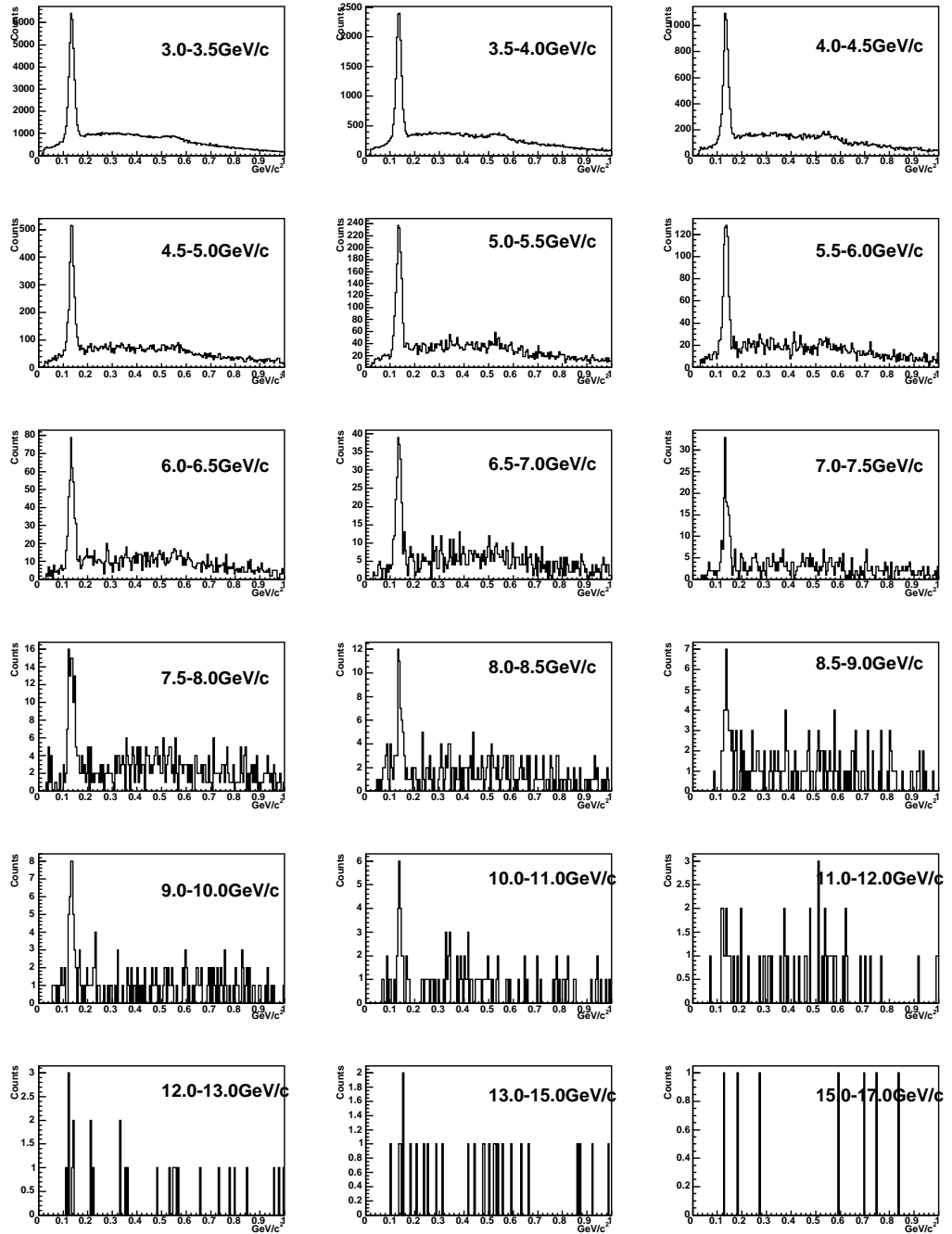


Figure 4.17: Invariant mass distribution of two photons with minimum energy cut at 150 MeV. Each panel corresponds to a certain photon p_T (West Arm).

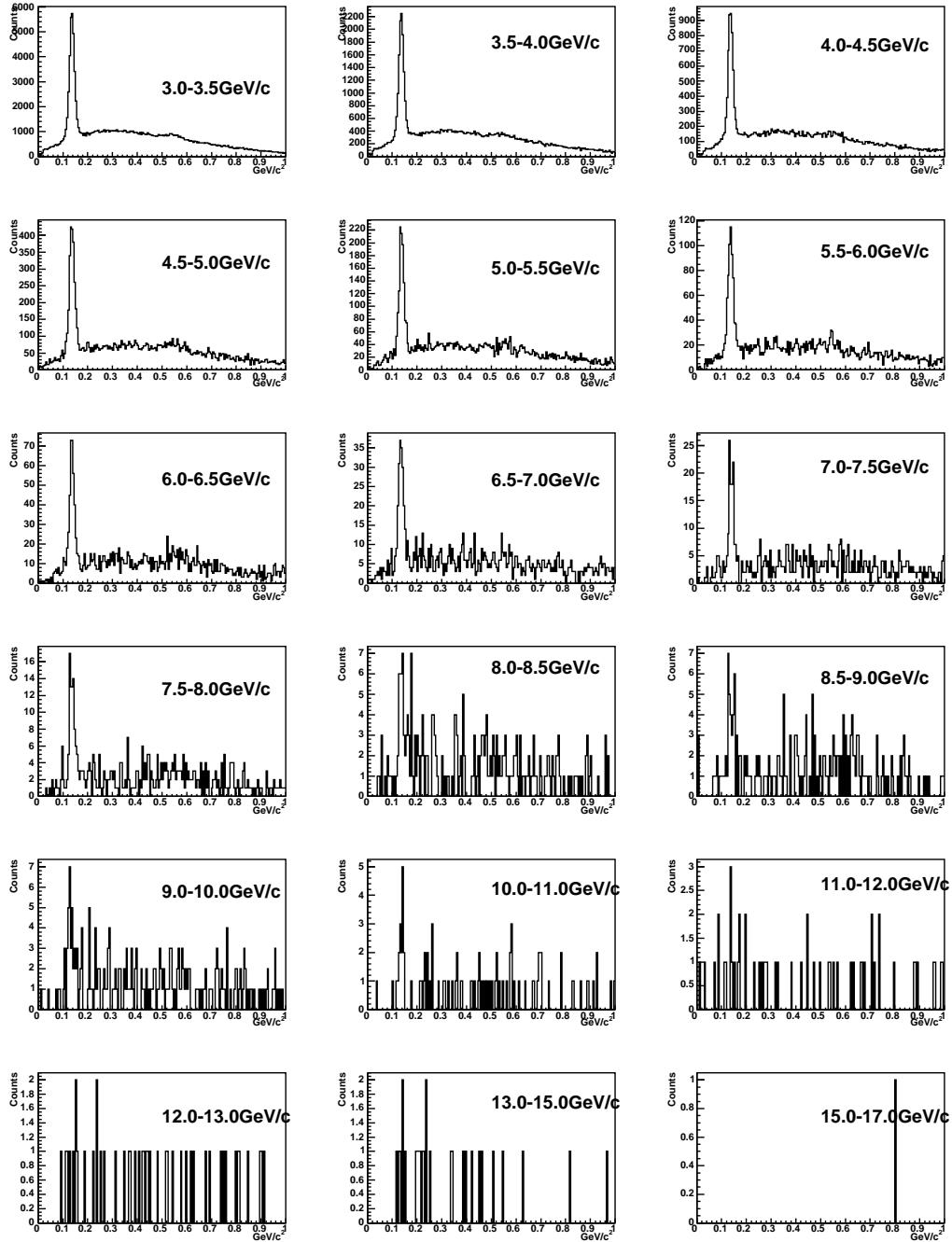


Figure 4.18: Invariant mass distribution of two photons with minimum energy cut at 150 MeV. Each panel corresponds a certain photon p_T (East Arm).

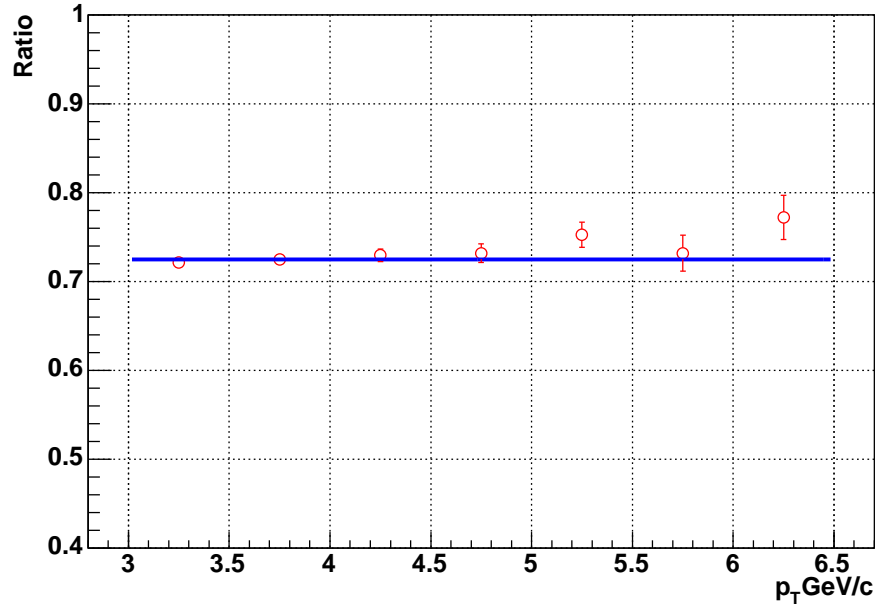


Figure 4.19: The fraction of π^0 photon signal in West Arm.

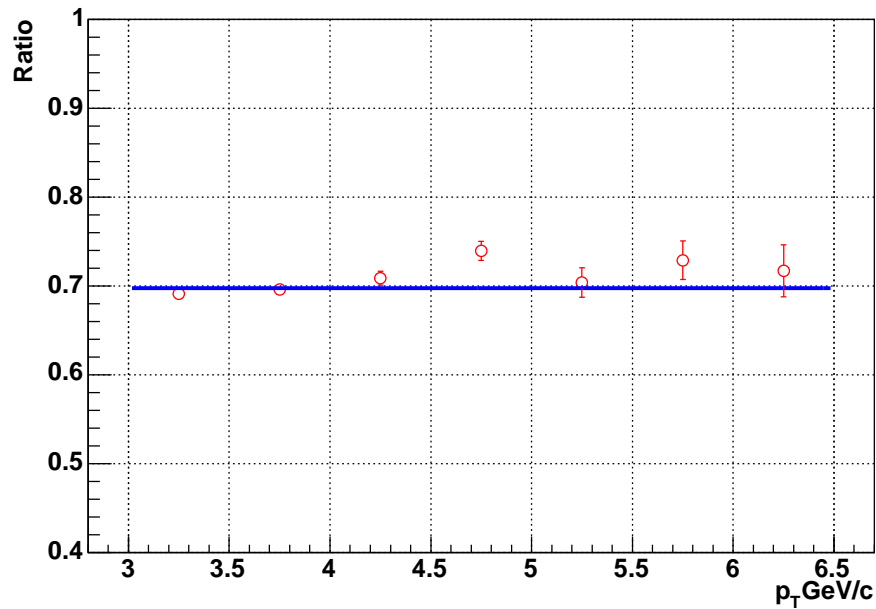


Figure 4.20: The fraction of π^0 photon signal in East Arm.

4.5.4 π^0 Missing Ratio

The π^0 partner photons can be lost due to EMCAL hot/dead mask, minimum Energy cut (=Emin cut), edge-cut, or two photon merging. When the angle of two photons from π^0 decay is small, two photons are detected as one cluster. Such a case is called 'two photon merging'. A photon cluster from π^0 is categorized depending on the case with its partner photon in the acceptance, with its partner missing, or merged with its partner. With its partner photon in acceptance, this condition is called "2tag". With its partner missing, this condition is called "1tag". All the merged photons are rejected with the photon probability cut in our energy region. The missing ratio R value is defined as follows;

$$R = \frac{1\text{tag}}{2\text{tag}} \quad (4.12)$$

The number of photons of 2tag is obtained by the procedure shown in Section 4.5.2, the number of all photons from π^0 decay can be obtained if R can be calculated. The R is calculated with FastMC. In the MC, π^0 's are produced according to the function as follows;

$$y = 393 p_T \left(\frac{1.212}{p_T + 1.212} \right)^{9.97} \quad (4.13)$$

This function was obtained by Run2002 π^0 analysis [124]. The η and ϕ distributions are explained in Section 4.5.3.

Figure 4.21 shows the obtained R . In the low p_T region, the R is large because the angle between two photons from π^0 decay is large. Figure 4.22 and 4.23 show the error of $(1 + R)$ for West Arm and East Arm, respectively. Figure 4.24 and Figure 4.25 show π^0 photon fraction which hit the EMCAL west and east, respectively. The green line represents merged photon and the red line represents merged photon + 1tag.

4.6 Contribution of η , η' , ω

In order to evaluate other photon contributions from decay of hadron such as η , ω , and η' , the ratio of η , ω , and η' production to π^0 production is used. Production and branching ratio of other hadrons compared to π^0 is listed in Table 4.1. The A_0 is calculated using the the ratio of η , ω , and η' production to π^0 production and those branching ratio as shown in Table 4.1. However it should be modified in high p_T regions where π^0 photon merges. This is because photons from heavier hadrons rarely merge, so that they are unlikely

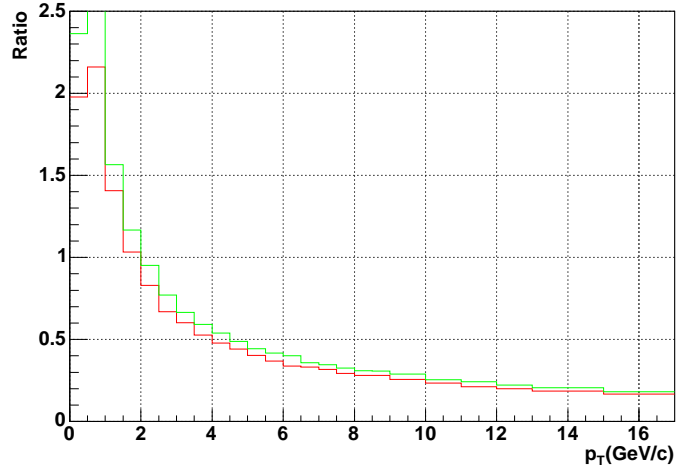


Figure 4.21: π^0 missing ratio R . Red line is for West arm and green line is for East arm.

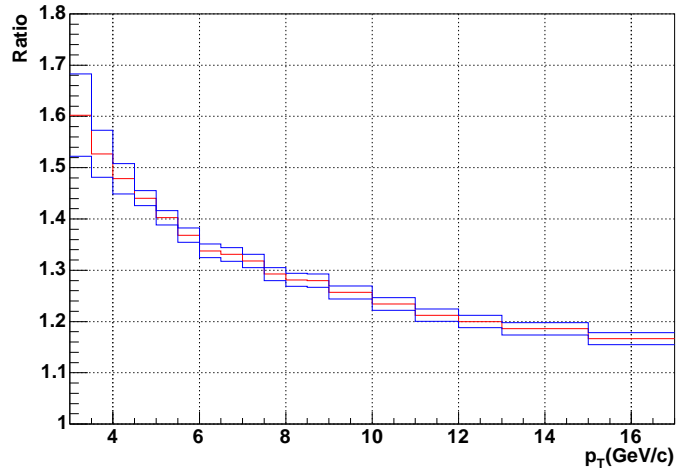


Figure 4.22: The error of π^0 missing ratio $\Delta(1 + R)$ for West Arm is shown. Red line is $(1 + R)$ and blue line is $(1 + R) \pm \Delta(1 + R)$.

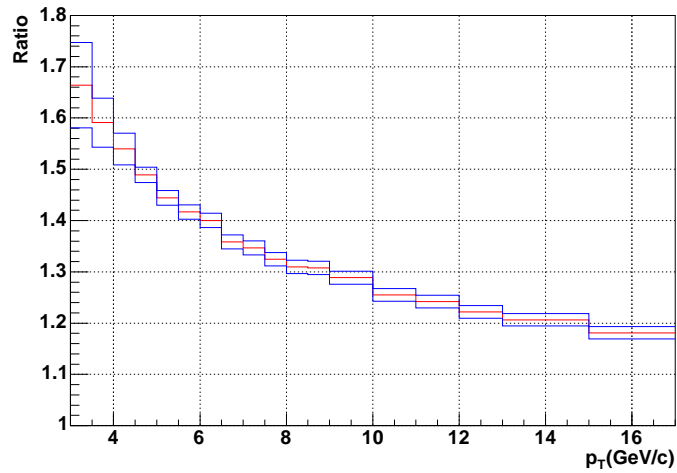


Figure 4.23: The error of π^0 missing ratio $\Delta(1 + R)$ for East Arm is shown. Red line is $(1 + R)$ and blue line is $(1 + R) \pm \Delta(1 + R)$.

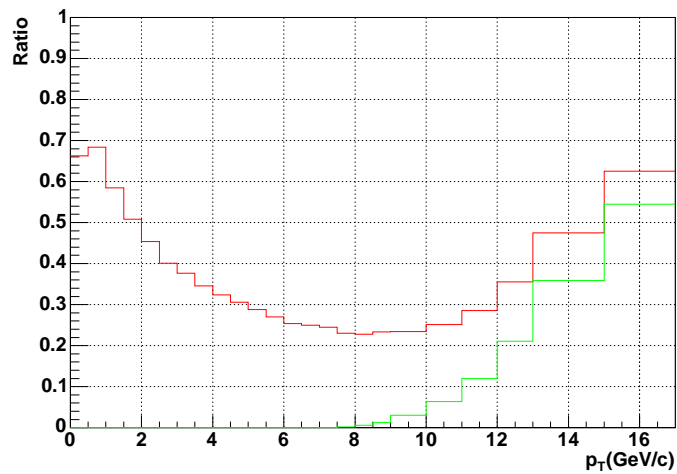


Figure 4.24: The fraction of 1tag and merged photon for π^0 photon which hits the EMCAL west. The fraction is normalized to all the photon originating from π^0 decay. The green line represents merged photon and the red line represents merged photon + 1tag.

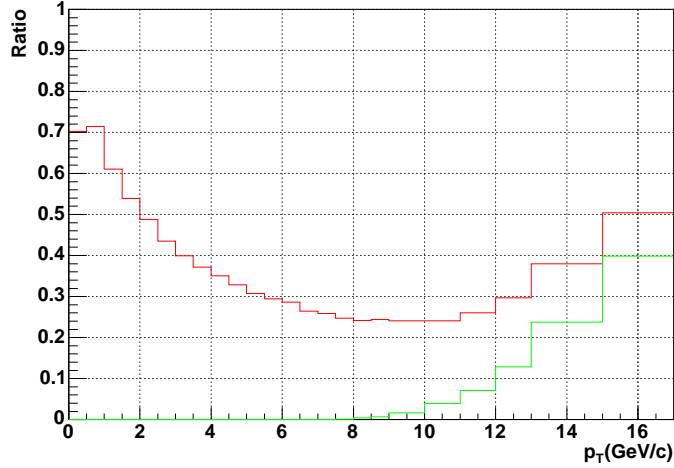


Figure 4.25: The fraction of 1tag and merged photon for π^0 photon which hits the EMCal east. The fraction is normalized to all the photon originating from π^0 decay. The green line represents the fraction of merged photon and the red line represents the fraction of merged photon + 1tag.

to be rejected by the photon probability cut. There is the distortion of $(A_0 - 1)$ due to π^0 photon merge. $A_0 - 1$ is the ratio of η, ω , and η' production to π^0 production without the distortion due to π^0 photon merge. Therefore, the A_0 should be modified as follows:

$$A = 1 + (A_0 - 1) \nu, \quad (4.14)$$

where ν is the correction factor of the distortion. The A is shown in Figure 4.26 and 4.27.

4.7 Charged Particle Background

The DC live ratios are evaluated to be 94% in the west and 99% in the east. The DC live ratio means that the ratio of the DC working area to all area of the DC. The typical value of the veto by DC track to the total clusters is 4%. Therefore, the contamination of charged hadrons is expected to be at most

$$R \times (1 - \epsilon_{DC}) = 0.04 \times (1 - 0.94) = 0.0024 \quad (4.15)$$

One concern might be raised about the ϕ coverage of DC tracks since the magnetic field bends the trajectory. Figure 4.32 gives a rough idea for the

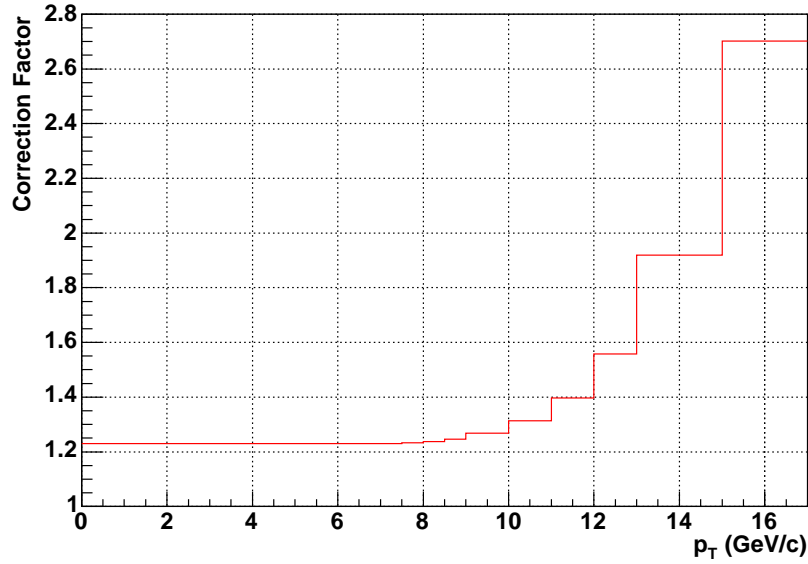


Figure 4.26: The distortion of factor of non- π^0 hadronic decay contribution by the π^0 merge in the West arm.

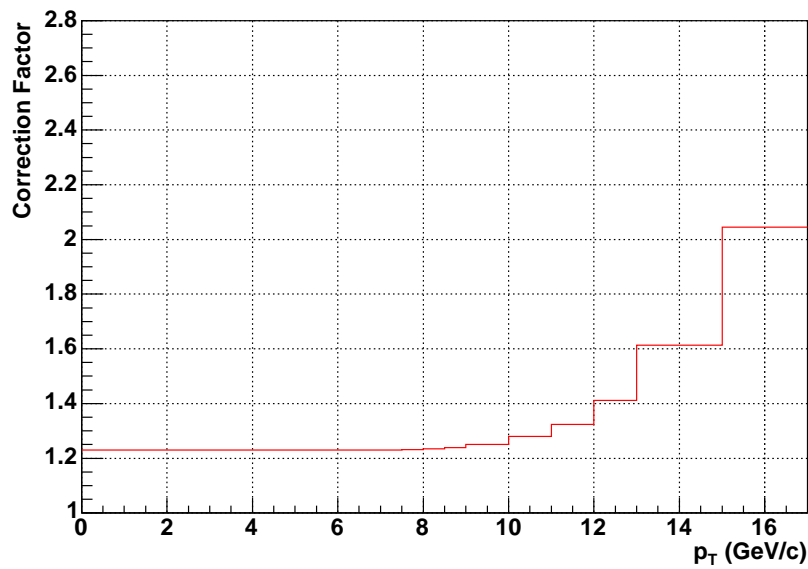


Figure 4.27: The distortion of factor of non- π^0 hadronic decay contribution by the π^0 merge in the East arm.

Particle	Production ratio	Branching ratio	γ ratio ($A_0 - 1$)
η/π^0	0.45 ± 0.1	$\frac{Br(\eta \rightarrow 2\gamma)}{Br(\pi^0 \rightarrow 2\gamma)} = 39.4/98.8$	0.18 ± 0.04
ω/π^0	1.0 ± 0.3	$\frac{Br(\omega \rightarrow \pi^0 \gamma)}{Br(\pi^0 \rightarrow 2\gamma)} \times 0.5 = 8.9/98.8 \times 0.5$	0.045 ± 0.014
η'/π^0	0.25 ± 0.08	$\frac{Br(\eta' \rightarrow 2\gamma)}{Br(\pi^0 \rightarrow 2\gamma)} = 2.1/98.8$	0.0053 ± 0.0017
Sum	-	-	0.23 ± 0.05

Table 4.1: Production and branching ratio of other hadrons to π^0 [125].

bend. In this figure, the difference between ϕ and ϕ_{PC3} is inversely proportional to p_T . Since the EMCAL cluster energy is above 3 GeV, it is sufficient to think about 2 GeV/c tracks. For 2 GeV/c tracks, $\Delta\phi = (\phi - \phi_{PC3})$ is $0.055/2 = 0.028$ [rad], which corresponds to 14 cm at the EMCAL. This is safe enough, since the fiducial cut rejects 63 cm around the arm.

The ϕ distribution of DC track occupancy is shown in Figure 4.28 and Figure 4.29. Track matching of direction in z and ϕ of EMCAL with DC track is shown in Figure 4.30 and Figure 4.31, respectively. These distributions are normalized by deviation of the matching distribution. Therefore ± 3 in these distributions correspond to $\pm 3\sigma$, where σ represents the deviation of the DC track matching to EMCAL cluster. The region within ± 3 is tagged as a charged track.

4.8 Neutral Particle Background

In this section, the contamination from neutral hadron interactions is considered.

The strategy to evaluate the contribution (in PbSc) is basically shown in the following.

- Input spectra of neutral hadrons from charged hadron measurements
- The EMCAL response function from PISA (GEANT)
- A fine tuning of the response function with charged hadron clusters
- Calculate the product

Since our measurements of identified charged hadrons are limited in the p_T range, methods to extrapolate to higher p_T are needed. Figure 4.33 shows

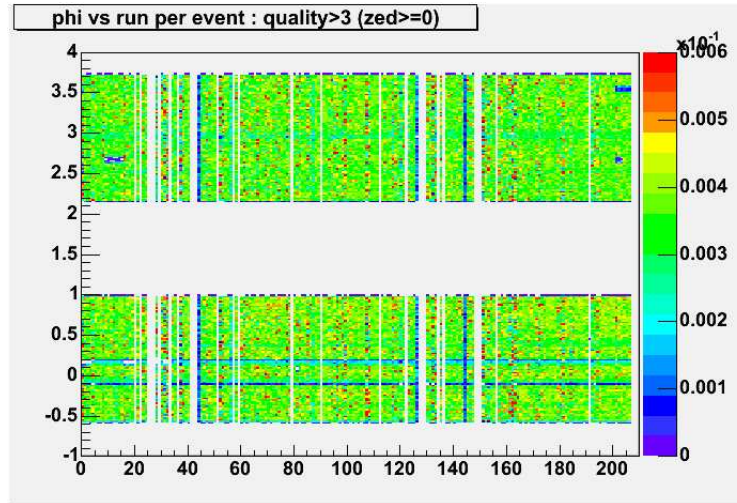


Figure 4.28: DC track occupancy ($z \geq 0$) of ϕ (rad) along the run sequence. The top part corresponds to the east arm. The bottom part corresponds to the west arm.

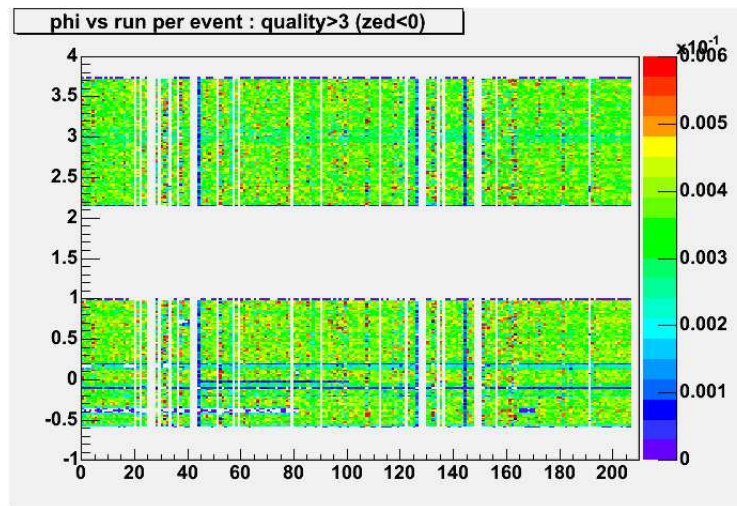


Figure 4.29: DC track occupancy ($z < 0$) of ϕ (rad) along the run sequence. The top part corresponds to the east arm. The bottom part corresponds to the west arm.

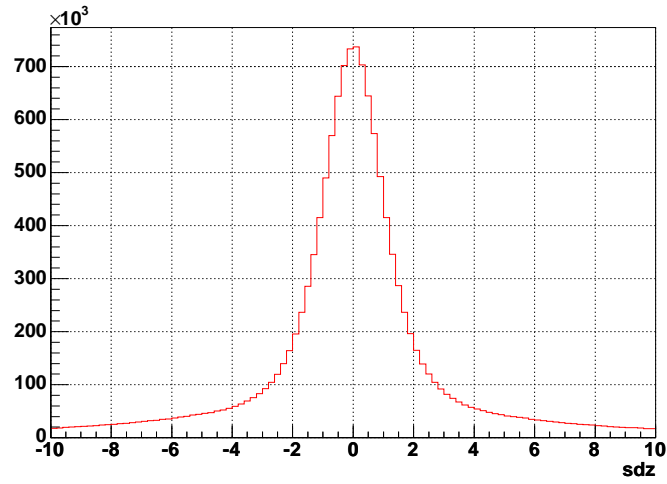


Figure 4.30: Track matching of direction in z of EMCAL with DC track.

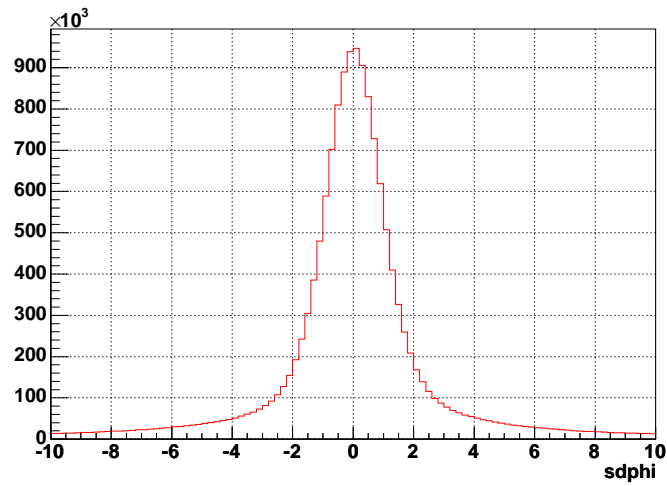


Figure 4.31: Track matching of direction in ϕ of EMCAL with DC track.

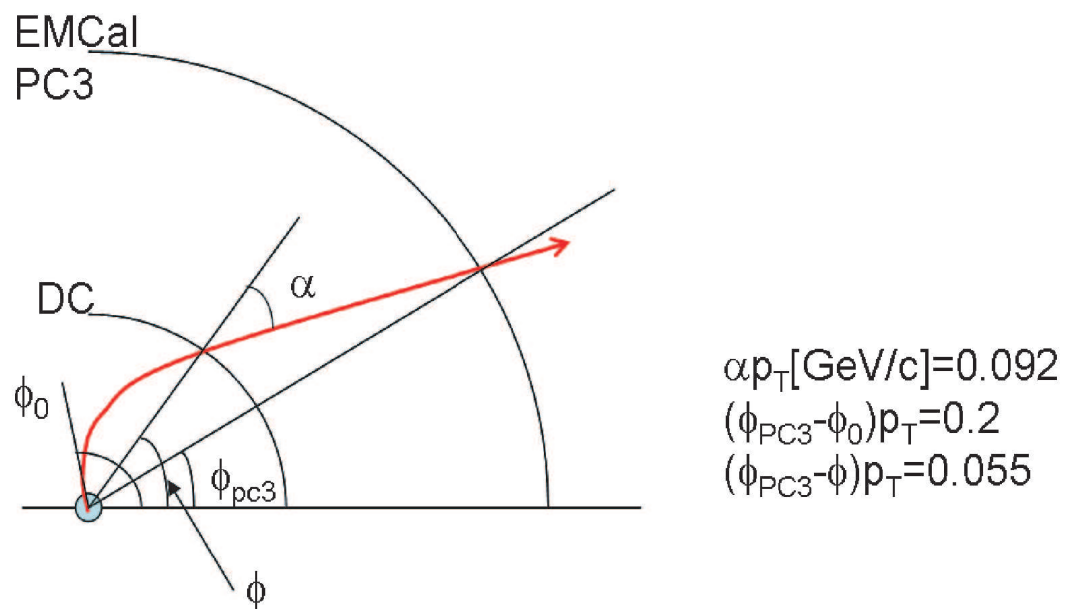


Figure 4.32: A rough sketch of the trajectory of a charged hadron.

two ways of extrapolation. An exponential functions are shown with dotted curves. Figure 4.34 shows ratios of input spectra to pion's spectra. Measurements are shown by black squares, blue points show outputs of PYTHIA. In this analysis, the extrapolation is done with a smooth connection of measurements and PYTHIA spectra. Three curves indicate systematic error range. Neutrons, anti-neutrons and K_L^0 's are assumed to have the same spectra as protons, anti-protons and K^\pm , respectively.

The EMCal response function obtained by PISA was checked with the real data. Figure 4.35 shows this procedure for anti-protons. Because of lack of knowledge about the EMCal response for hadrons in Monte Carlo, it is needed to scale the response function by 0.85 ± 0.10 to reproduce the data. The bottom panel in Figure 4.35 shows the difference between energy deposits in the EMCal and the calculation from the momentum. This factor is found to be universal for all the species.

However, it was found that the photon shape was not reproduced well in PISA for anti-protons. The data show more reduction with the photon probability cut by a factor of 1.6. Figure 4.36 shows this tuning.

Now there are input spectra and response functions, so the neutral hadron contributions can be calculated. Figure 4.37 shows an estimation for anti-neutrons. By comparing the total "photon" clusters (black line) and estimated anti-neutron clusters (blue line), the contributions to the total is calculated (shown in the bottom panel). Three blue lines correspond to the upper and lower assumptions of the input spectra.

Figure 4.38 and Figure 4.39 show the contributions of three kinds of neutral hadrons. The error bar indicates the upper and the lower assumptions of the input spectra (the energy scale factor uncertainty) in Figure 4.38 (Figure 4.39).

From Figure 4.38 and Figure 4.39, the total contribution of neutral hadrons are about 1% at $p_T = 3 \sim 4$ GeV/ c , it is about 0.5% up to 10GeV/ c , and it is about 0.1% at more than 10 GeV/ c . The uncertainty of the energy scale correction of the response matrix is more significant than the one of input spectra.

4.9 Non-Vertex Origin Background

To estimate backgrounds not originated from the collision vertex, the simulation study with PYTHIA [123] + PISA (PHENIX Integrated Simulation Application) was done. Total 10M events were produced and went through PISA. Figure 4.40 shows origins of EMCal clusters in $r - z$ projection. Many of those are due to photon to e^+e^- pair conversions which took place in dif-

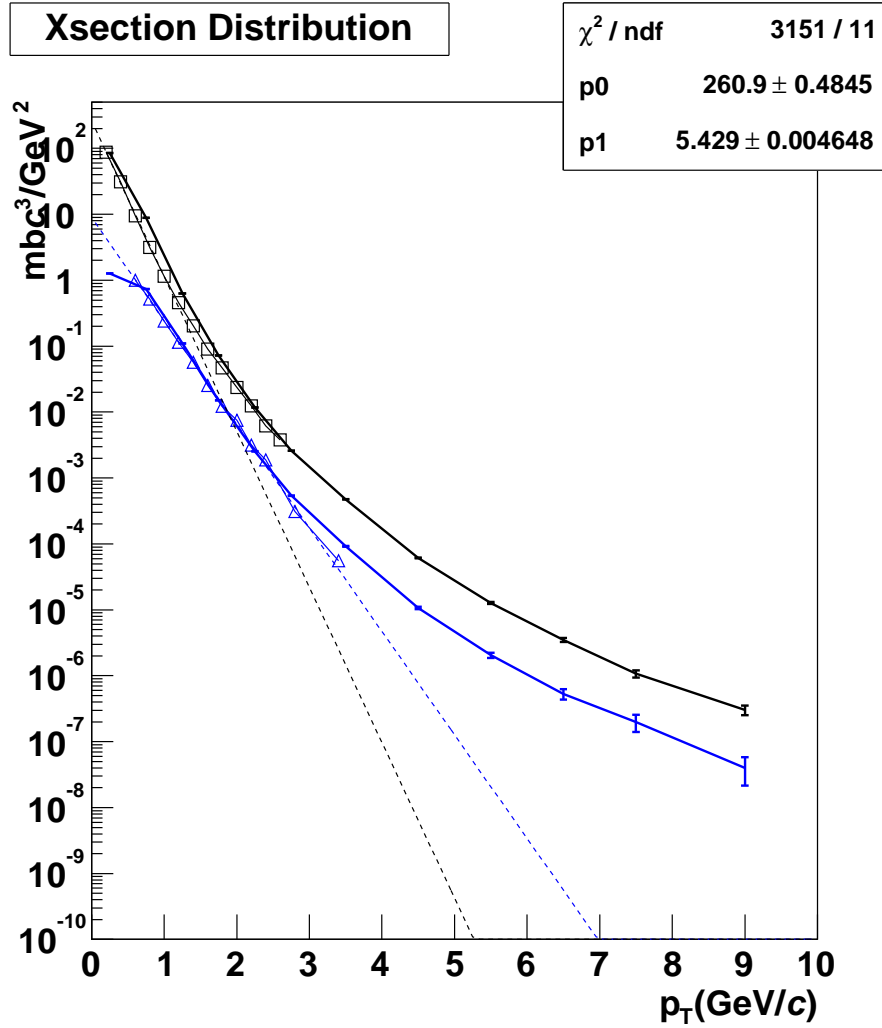


Figure 4.33: Extrapolations of the spectra. Pions are from the measurement of identified charged hadrons, Dotted lines: extrapolation, solid curves: used in this analysis. Black represents π^- . Blue represents \bar{p} .

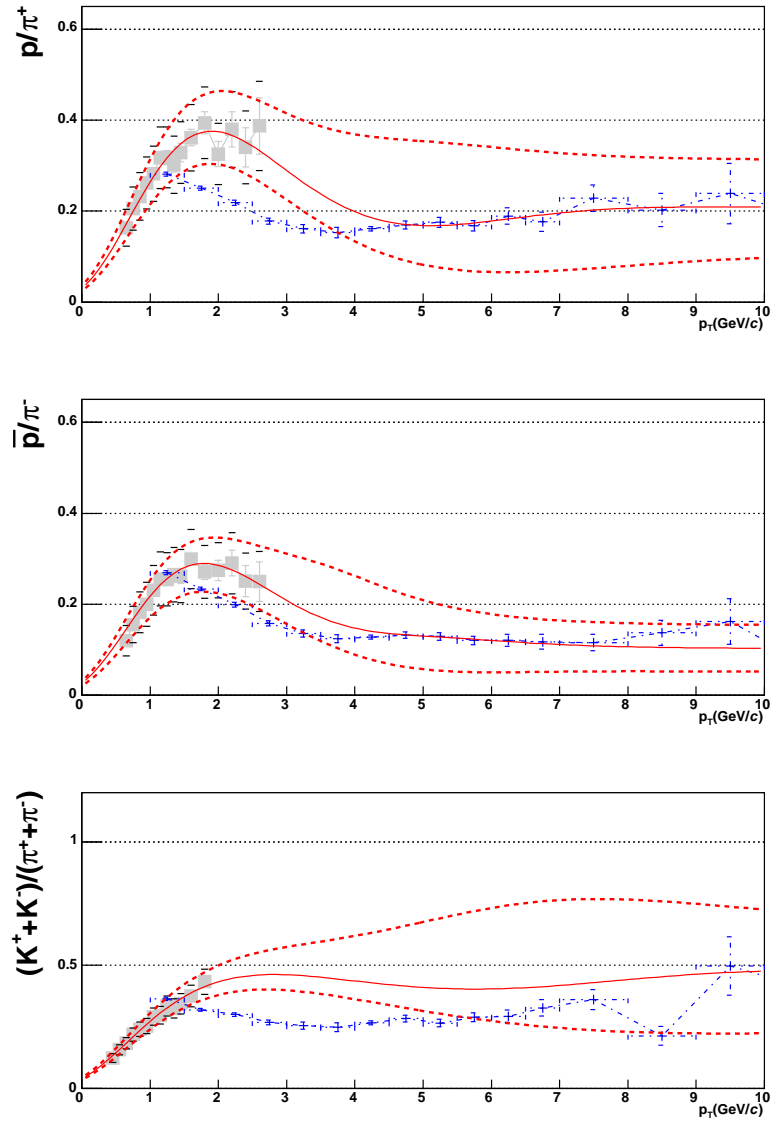


Figure 4.34: Input spectra compared to the pion spectra. Extrapolation to high p_T region is done with the combination of measured spectra and a PYTHIA output. Black squares are from PHENIX measurements. Blue line is from PYTHIA. Red line shows a connection of data (low p_T) and PYTHIA (high p_T). Red dotted lines show a systematic error bands.

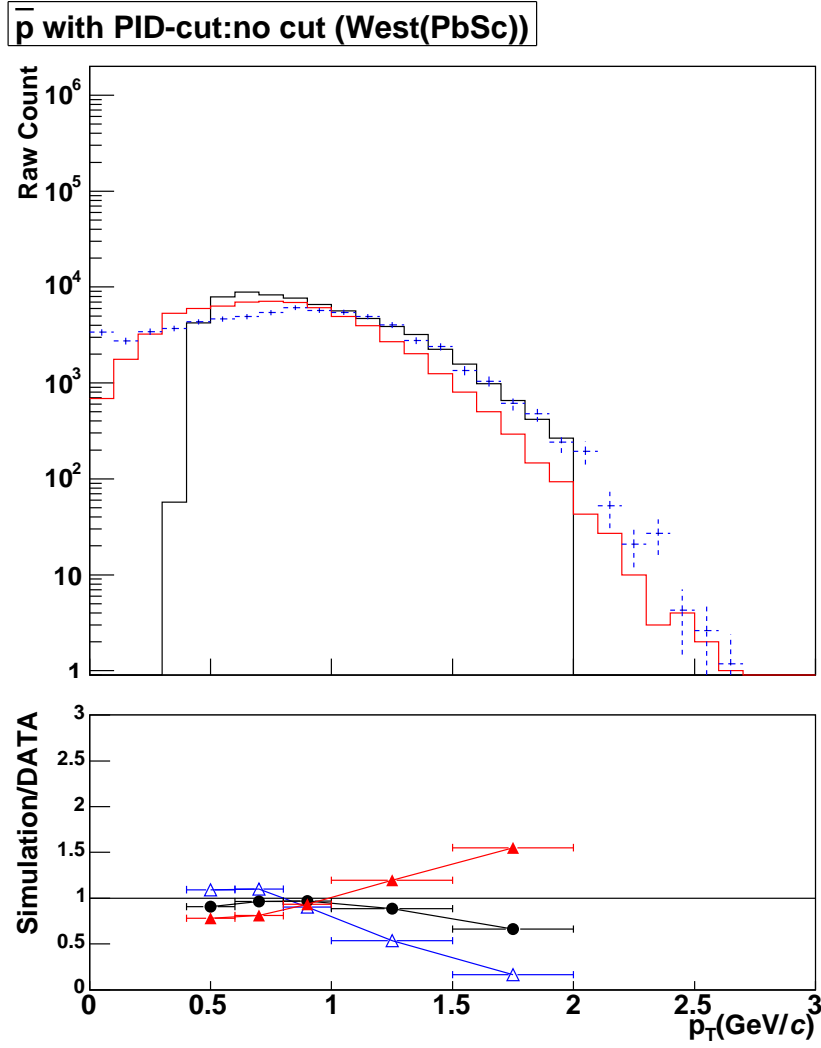


Figure 4.35: Comparison of the EMCAL response with \bar{p} data. An additional scale factor 0.85 ± 0.10 is needed to adjust them. The bottom panel shows the difference between the measurement and the calculation after this tuning. Three lines show the energy scale uncertainty. Black represents the momentum of particles. Red represents $ecore \times \cos(\theta)$. Blue is Black \times response matrix.

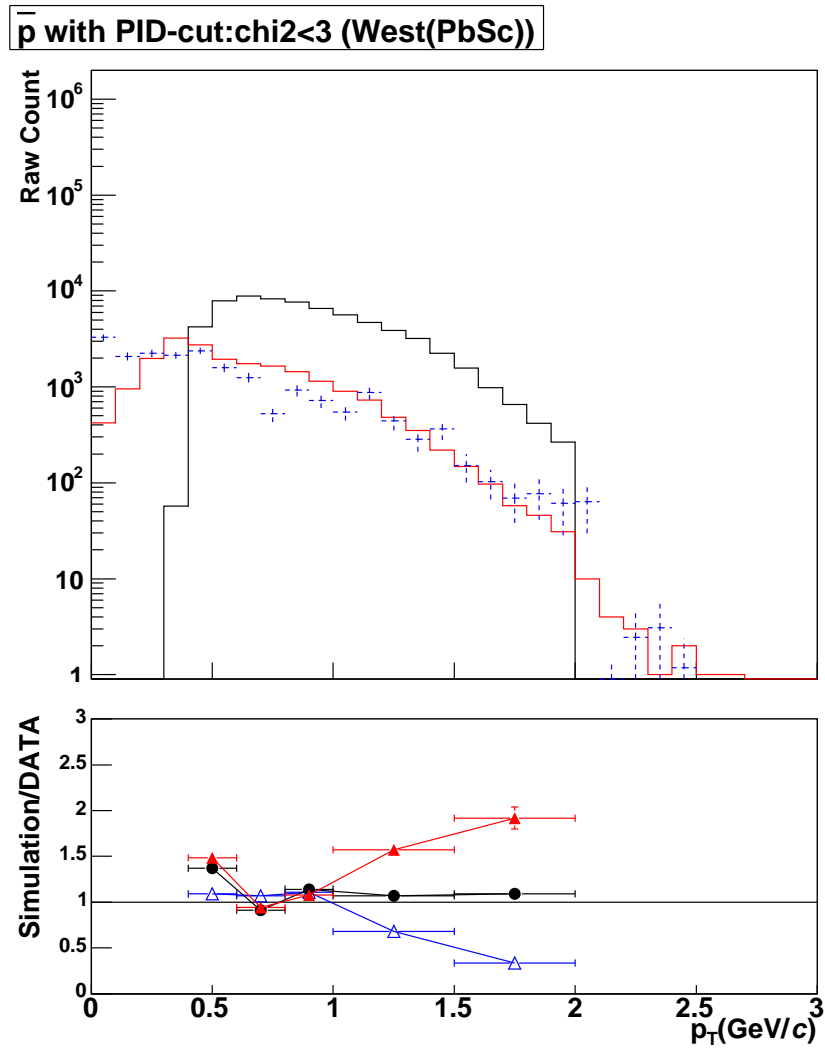


Figure 4.36: Comparison of the EMCAL response with \bar{p} data with a photon shape cut. Only for \bar{p} , an additional factor of 1.6 is needed. The bottom panel shows the difference after the tuning. Three lines show the energy scale uncertainty. Black represents the momentum of particles. Red represents $ecore \times \cos(\theta)$. Blue is $\text{Black} \times \text{response matrix}$.

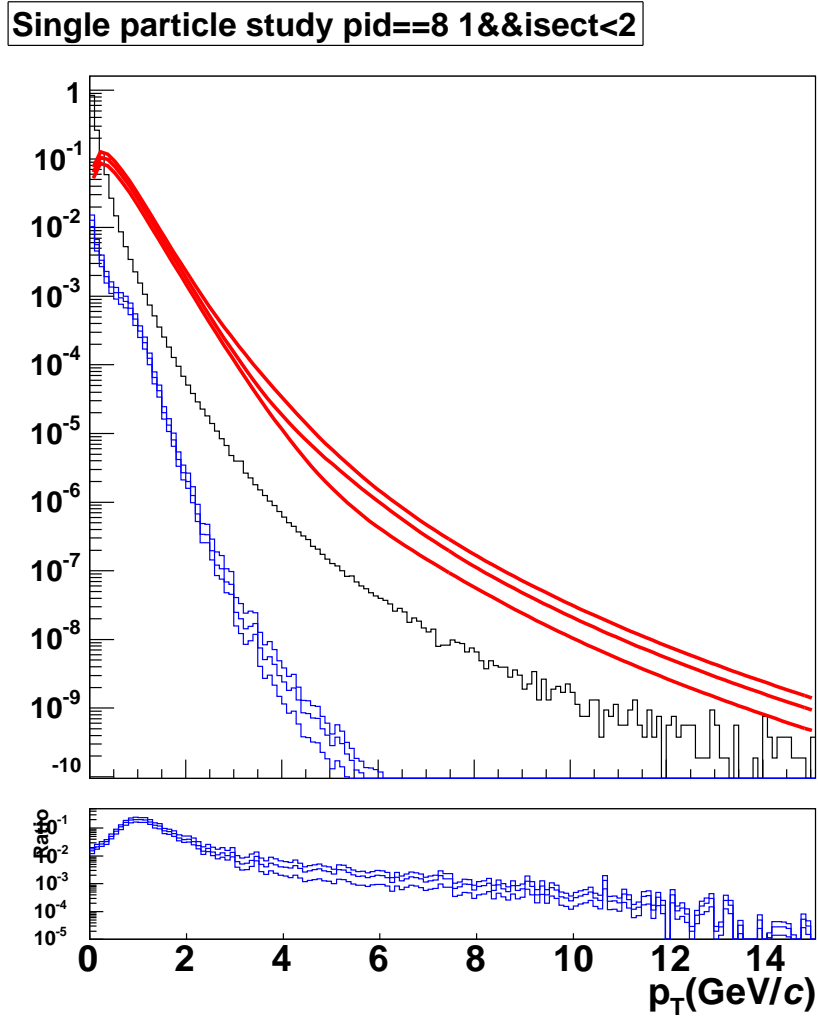


Figure 4.37: Estimation of anti-neutron contributions. Black represents photon cluster. Red represents the estimated anti-neutron spectra. Blue represents $\text{red} \times \text{response matrix} \times \text{factor}$. The contributions to the total photon clusters are shown in the bottom panel.

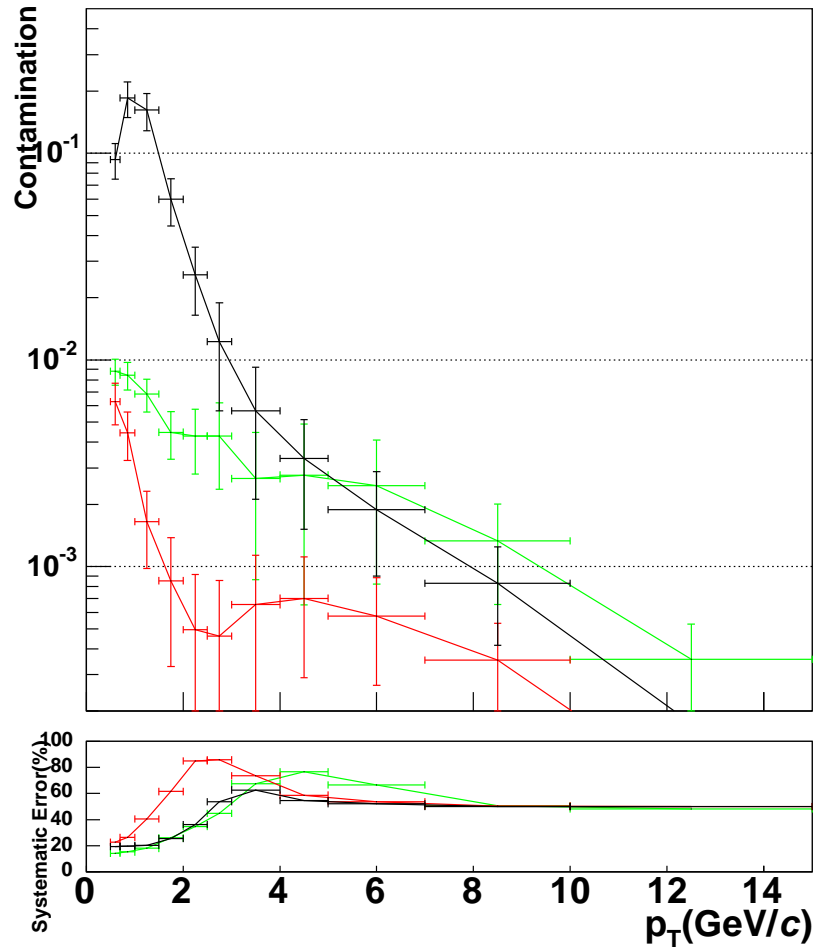


Figure 4.38: Error in contamination evaluation due to variations of the input spectra. Black represents anti-neutron. Green represents K_L^0 . Red represents neutron.

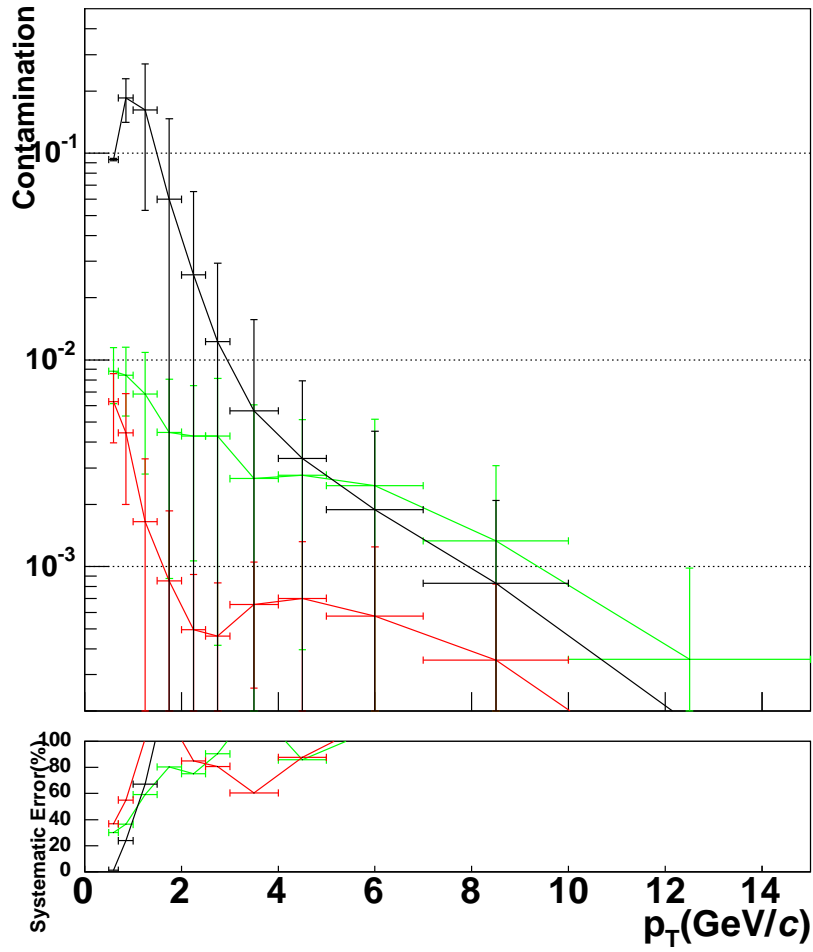


Figure 4.39: Error in contamination evaluation due to variations of the correction factors of the energy scale. Black represents anti-neutron. Green represents K^{0L} . Red represents neutron.

ferent places. The θ_r is used in Figure 4.40 to separate conversions (In case $\cos \theta > 0.9$, those are conversions). Figure 4.41 shows the energy distribution of all EMCal clusters and those from secondary interactions. Since slopes are similar for more than 2 GeV clusters, the secondary backgrounds is negligible at higher energies.

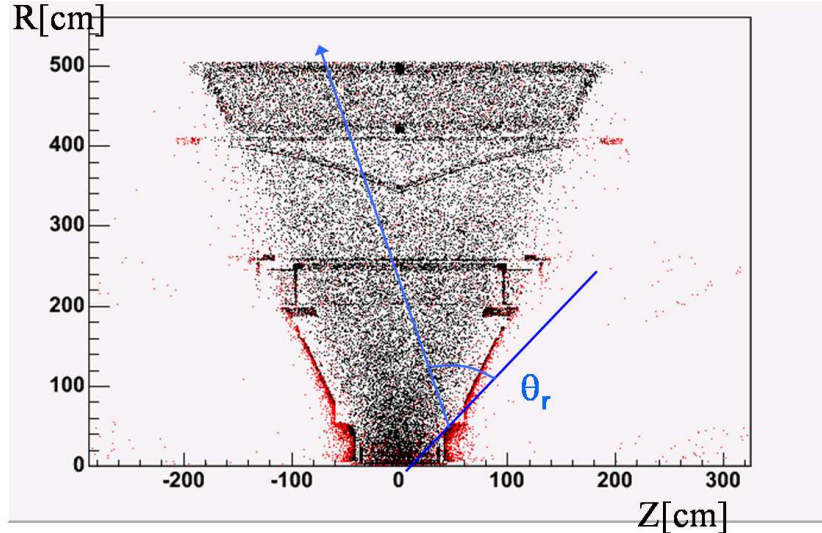


Figure 4.40: Origins of EMCal clusters in $r - z$ plane. Definition of θ_r is also shown. Red points are taken as secondary sources because of large θ_r .

4.10 Correction for Photon Conversion

To measure the prompt photon cross section, one has to carefully analyze photon yield with the subtraction of backgrounds and various corrections. By photon conversion, both the signal and the background of prompt photons can be reduced and need to be corrected for. However, not all converted photons are lost. Most conversions occur near EMCal and the cluster produced by converted e^+e^- have the similar energy and the position as the original photon. When a conversion occurs near the collision point, the cluster(s) produced by e^+e^- would be discarded due to a charge veto cut. Even when a conversion happens after DC, passing a charge veto cut, the reconstructed energy from e^+e^- could be smaller than that of the original photon, and may not contribute to the direct photon yield significantly because of a steep p_T distribution. This is also the case for π^0 reconstruction, where π^0 is one of the

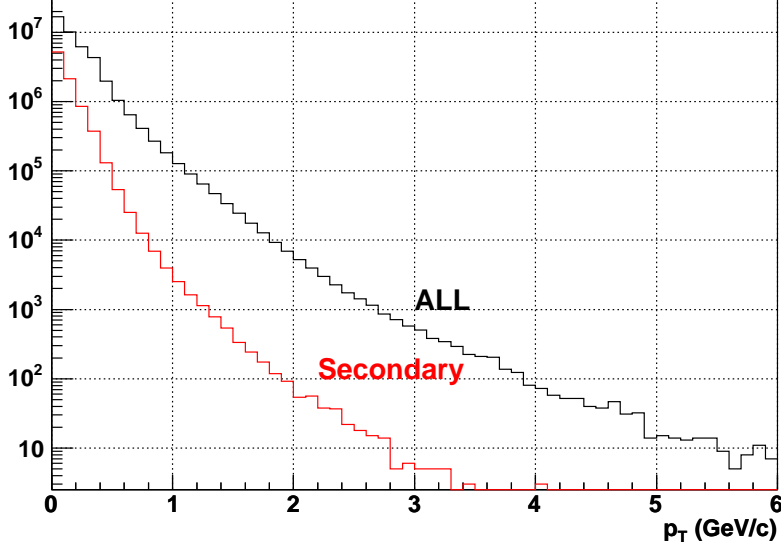


Figure 4.41: Energy distribution of all and non-vertex origin secondary clusters from data.

dominant sources of prompt photon background. Due to photon conversion, π^0 might not be reconstructed. Even when it is reconstructed, its mass could be outside the mass windows. In this study the conversion correction factors for single photons and π^0 are evaluated. The PISA simulation outputs are used.

With a photon in a good event, there are three possibilities;

1. A photon is not converted, and hits EMCal.
2. A photon is converted, and e^+ or e^- or both hits EMCal.
3. A photon is converted, and dose not hit EMCal.

1 is called a photon track, and 1-3 is called full track. The correction factor relative to photon tracks is the value of interest. The correction factor is defined by taking a double ratio;

$$\epsilon^{conversion} = \frac{n_{photon}/n_{full}}{N_{photon}/N_{full}} \quad (4.16)$$

where n_{photon} is the number of reconstructed clusters by photon tracks, n_{full} is the number of reconstructed clusters by full tracks, N_{photon} is the number

of the input photons from photon tracks, and N_{full} is the number of the input photons from full tracks. The value of $\epsilon^{conversion}$ is listed in Table 4.2.

Similarly, π^0 loss correction factor for conversion is defined as follows:

$$\epsilon_{\pi^0}^{conversion} = \frac{n_{photon}^{\pi^0}/n_{full}^{\pi^0}}{N_{photon}^{\pi^0}/N_{full}^{\pi^0}} \quad (4.17)$$

where n_{photon} is the number of reconstructed π^0 in photon events, n_{full} is the number of reconstructed π^0 in full events, N_{photon} is the number of the input π^0 that are reconstructed as photons, and N_{full} is the number of the input π^0 in full tracks. The value of $\epsilon_{\pi^0}^{conversion}$ is listed in Table 4.3.

	PbSc (West)	PbSc (East)	PbGl (East)
$1/\epsilon^{conversion}$	103.1 ± 1.0	102.9 ± 1.0	103.9 ± 1.0

Table 4.2: Single photon conversion correction factors. The errors are evaluated systematic errors of energy smearing, vertex cut, and acceptance.

	PbSc (West)	PbSc (East)	PbGl (East)
$1/\epsilon_{\pi^0}^{conversion}$	101.2 ± 1.2	102.0 ± 1.7	103.3 ± 1.9

Table 4.3: π^0 conversion correction factors. The errors are evaluated systematic errors of energy smearing, vertex cut, and acceptance.

4.11 Photon Efficiency with High- p_T Trigger

The photon efficiency with high p_T trigger is not 100% because some of the high p_T trigger tiles did not work. One high- p_T trigger tile is made of 12x12 tower. Several high- p_T trigger tiles were masked during the run. The masked tiles cannot trigger for photons. Therefore, the photon efficiency is reduced by the trigger mask. In other words, reduction of photon efficiency can be described as a reduction of acceptance. Therefore, the photon efficiency of high- p_T trigger can be calculated with the acceptance correction factor. This is discussed in Section 4.13.

4.12 Trigger Bias of Minimum Bias Trigger

In PHENIX, minimum bias trigger which fires only when there are charged particles at forward and backward rapidity is used as a basic trigger for all cross section measurement to normalize the measurement. This property of the minimum bias trigger affects the normalization of measurement. Furthermore, this property could distort the prompt photon measurement because it biases the physics process which generates observed prompt photons. The correction for this bias can be determined using another trigger which is independent of minimum bias trigger, for example ERT 4x4 trigger. The correction factor for this bias, $\epsilon^{BBCbias}$, is evaluated to be 0.785 in RUN2003.

4.13 Acceptance and Smearing Correction

Acceptance and smearing correction is calculated using the fast MC tuned by π^0 mass and width. Smearing means that the slope of cross section for prompt photon production is smeared by energy resolution. Photons are generated according to the function of $(0.1506/p_T^{6.047})$ which is obtained by fitting the Run3pp prompt photon data from 3 to 17 GeV. The fast MC determines whether it is accepted or not. Figure 4.42 shows an example of this input and output functions. The correction factor ($\epsilon^{acc\&smearing}$) can be obtained by those two. Since it did not have p_T dependence, a parameters obtained from a constant fit is used in this analysis. The smearing factor depends on the input slope and the energy uncertainty. The energy scale uncertainty is set to 1.5%. From the deviation of those results, the uncertainty in $\epsilon^{acc\&smearing}$ is determined to be 10%. Table 4.4 shows the $\epsilon^{acc\&smearing}$ for each trigger mask periods.

4.14 Cross Section and Systematic Errors

4.14.1 Evaluation of Cross Section

The invariant cross section for prompt photon production can be written as follows;

$$E \frac{d^3\sigma}{dp^3} = \frac{1}{2\pi} \cdot \frac{1}{p_T} \cdot \frac{d^2\sigma}{dp_T dy} \quad (4.18)$$

$$\approx \frac{1}{2\pi} \cdot \frac{1}{p_T} \cdot \frac{d^2\sigma}{dp_T d\eta} \quad (4.19)$$

Trigger mask period	Runs	events ($ z < 30cm$)	West	East
0	87790 - 87828	5140408	0.1014540	0.0823610
1	87828 - 87926	266576844	0.0987966	0.0823610
2	87926 - 88257	94243023	0.0966388	0.0823610
3	88257 - 88350	18385129	0.0966388	0.0823610
4	88350 - 88579	102536538	0.0966388	0.0810839
5	88579 - 89462	1215641043	0.0966388	0.0799663
6	89462 - 91211	863588019	0.0966388	0.0799663
7	91211 - 91318	153935982	0.0966388	0.0792497
8	91318 - 91984	1578354607	0.0966388	0.0787002
9	91984 - 92446	1151821811	0.0966388	0.0787002
Average	-	-	0.0967489	0.0795017

Table 4.4: The acceptance and smearing correction for each trigger mask period.

where rapidity y and pseudo-rapidity η are explained in Appendix A. The approximation of $y \sim \eta$ involves 1% correction at p_T of 1 GeV/c, 0.25% at 2 GeV/c.

The invariant cross section is evaluated as follows:

$$E \frac{d^3\sigma}{dp^3} = \frac{1}{2\pi} \cdot \frac{1}{p_T} \cdot \frac{N_\gamma^{corr}}{p_T \Delta p_T} \quad (\text{mbGeV}^{-2}\text{c}^3) \quad (4.20)$$

with

$$N_\gamma^{corr} = \frac{N_\gamma^{raw}}{\epsilon^{acc\&smearing} \cdot \epsilon^{highp_T} \cdot \epsilon^{BBCbias} \cdot \epsilon^{conversion}} \quad (4.21)$$

$$N_\gamma^{raw} = N_\gamma^{all} - (1 + (A_0 - 1)\nu)(1 + R)N_\gamma^{\pi^0} \quad (4.22)$$

$$L = \frac{N_{trig}^{mini}}{23.0} \quad (\text{mb}^{-1}) \quad (4.23)$$

where Δp_T is the width of the p_T bin, N_γ^{raw} is the detected prompt photon in the real data, $\epsilon^{acc\&smearing}$ is the acceptance and smearing correction factor, ϵ^{highp_T} is the photon efficiency of high p_T trigger, $\epsilon^{BBCbias}$ is the trigger

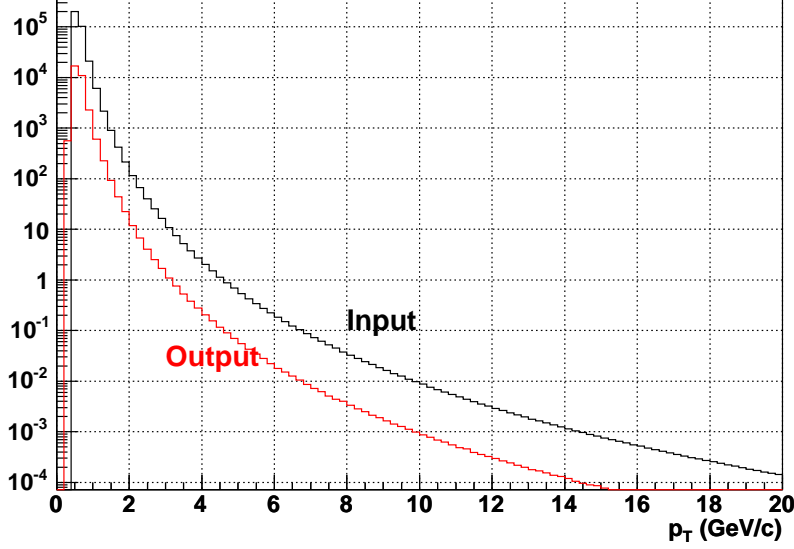


Figure 4.42: p_T spectra of input and output (FastMC). Black represents input spectra, while red represents output spectra after acceptance cut and smearing effect.

efficiency of photon in the minimum bias trigger, $\epsilon^{conversion}$ is the conversion correction, N_γ^{all} is all the photon in the acceptance, A_0 is the ratio of the number of photon from π^0 decay to η, η', ω decay, ν is the distortion of A_0 by merged photon of π^0 decay, R is the missing π^0 ratio, $N_\gamma^{\pi^0}$ is the π^0 decay photon which can be reconstructed. The value of 23.0 mb is the BBC trigger absolute cross section which are measured with Van der Meer scan.

Figure 4.43 and Figure 4.44 show the invariant cross section in West Arm and East Arm, respectively, with statistical error only. The weighted average of the cross section is obtained as follows:

$$\bar{N}(p_T) \pm \Delta\bar{N}(p_T) = \frac{\sum_i w_i(p_T) N_i(p_T)}{\sum_i w_i(p_T)} \pm \left(\sum_i w_i(p_T) \right)^{-1/2} \quad (4.24)$$

$$w_i(p_T) = 1/(\Delta N_i(p_T))^2 \quad (4.25)$$

where N_i and ΔN_i are the measured value and the statistical error respectively by $i = 1$ (West arm), $i = 2$ (East arm).

Finally, because the cross section is shifted by binning, it is corrected for such the effect. To calculate the correction factor, the data points are fitted

with following function:

$$f(p_T) = C \times p_T(1 + p_T/p_0)^{-n}, \quad (4.26)$$

where C , p_0 and n is the constants. The correction factor $C(p_T)$ is determined as follows:

$$C(p_T) = f(p_T)/f'(p_T) \quad (4.27)$$

$$f'(p_T) = \int_{p_{T1}}^{p_{T2}} f(p_T)/(p_{T2} - p_{T1}) \quad (4.28)$$

The weighted average of the cross section after the correction of the bin shift is shown in next chapter.

4.14.2 Systematic errors

The systematic error strongly depends on $1/W$, where $1/W$ is defined as the ratio of prompt photon signal to all photon ($N_\gamma^{raw}/N_\gamma^{all}$) in Equation 4.23. W is from about 8 at $p_T = 3$ GeV/c and 2 at $p_T = 16$ GeV/c as seen in Figure 4.45. The p_T dependence of W is represented by a second polynomial function as in,

$$1/W = c_1 + c_2 \times p_T + c_3 \times p_T^2, \quad (4.29)$$

where c_i , ($i = 1, 2, 3$) is the fit parameters. Figure 4.45 shows $1/W$ as a function of p_T .

Sources of systematic error and its estimation is listed below. Table 4.5 and Table 4.6 show the estimation. In case of the group A, this group does not depend on W . The group B depends on W . The group C, D, and E depend on $(W - 1)$.

- A1** When the energy is calculated by the ADC of EMCAL tower, the coefficient has an uncertainty. This is called energy scale error. This uncertainty is evaluated as 10%
- A2** The errors of acceptance and smearing correction factor are negligible.
- A3** The errors of normalization due to the luminosity and BBC trigger bias is 10% ($9.6\% \oplus 3\%$)
- A4** The errors of photon shape cut (4.4) and conversion correction 4.10 are negligible.
- A5** Due to photon conversion, the photon energy is shifted. However, this error is negligible.

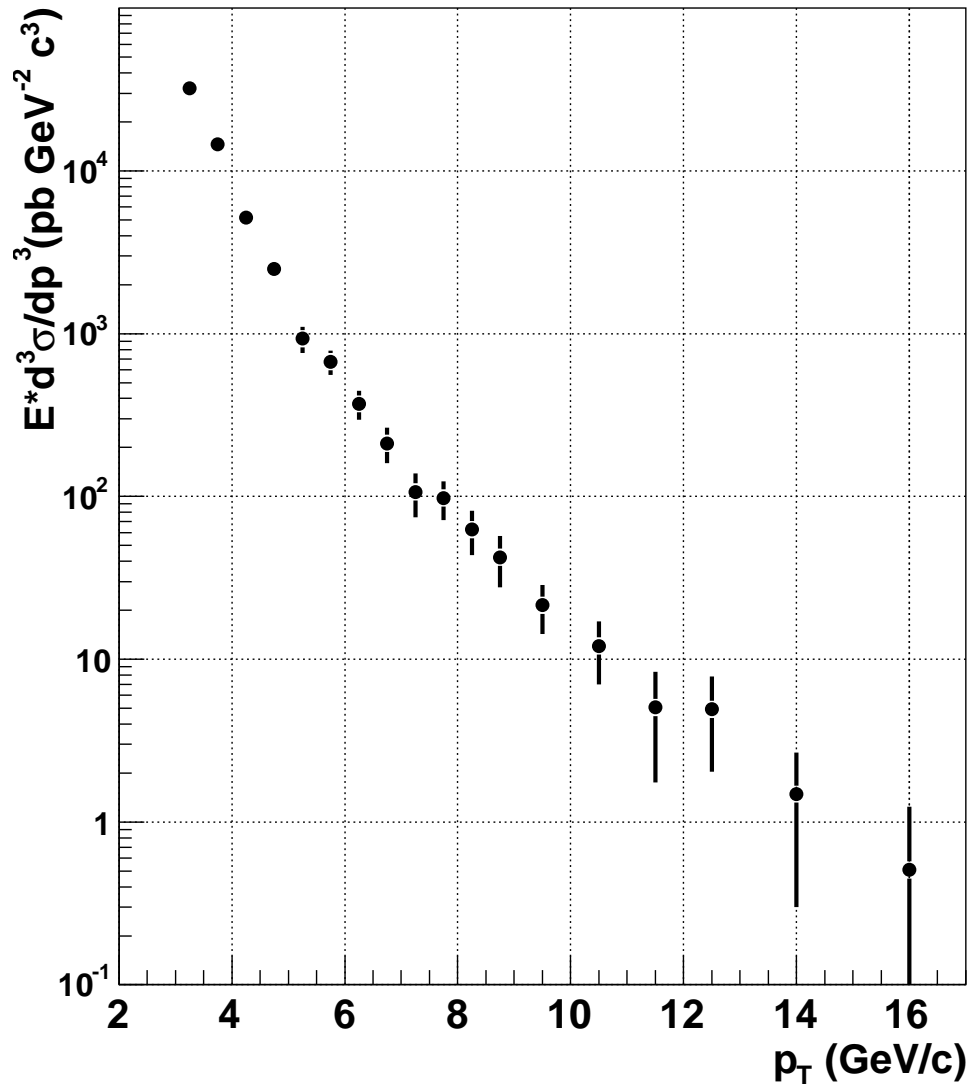


Figure 4.43: Invariant cross section in West Arm with statistical error only.

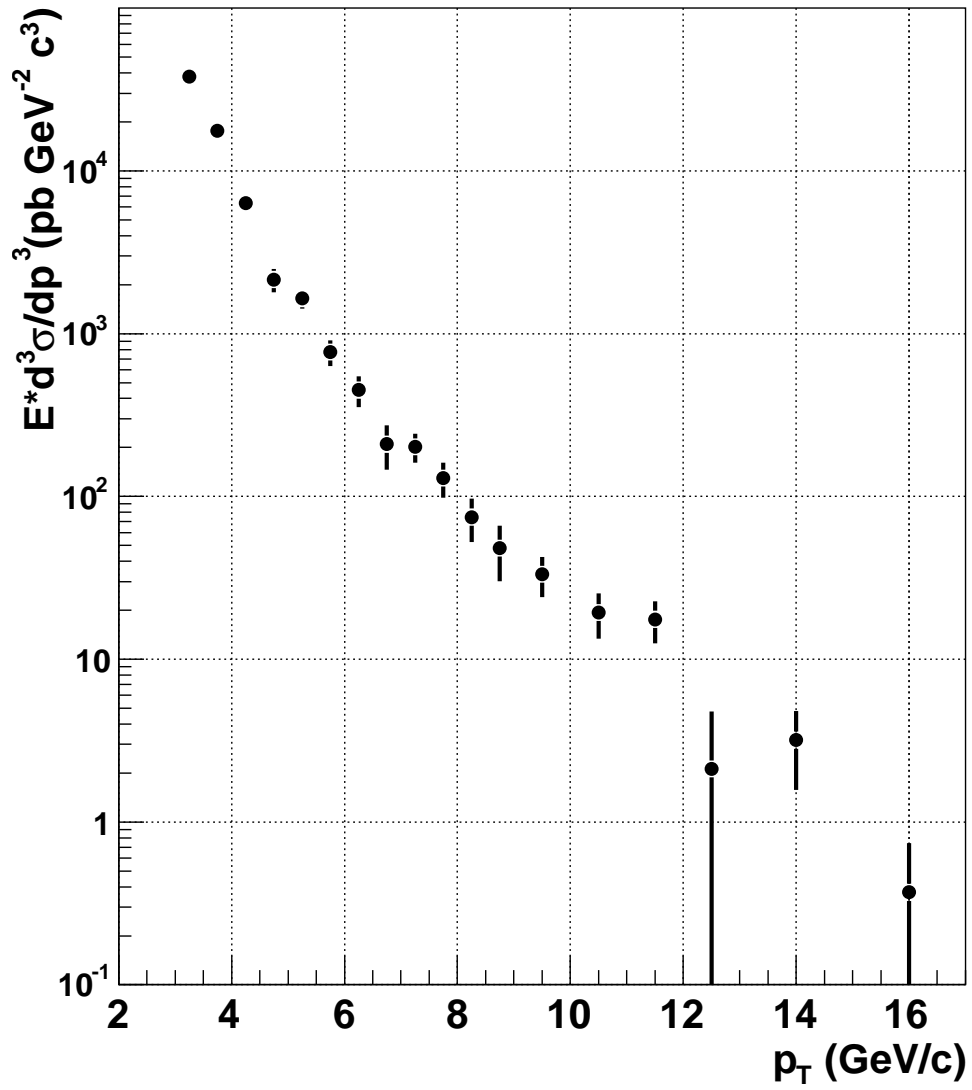


Figure 4.44: Invariant cross section in East Arm with statistical error only.

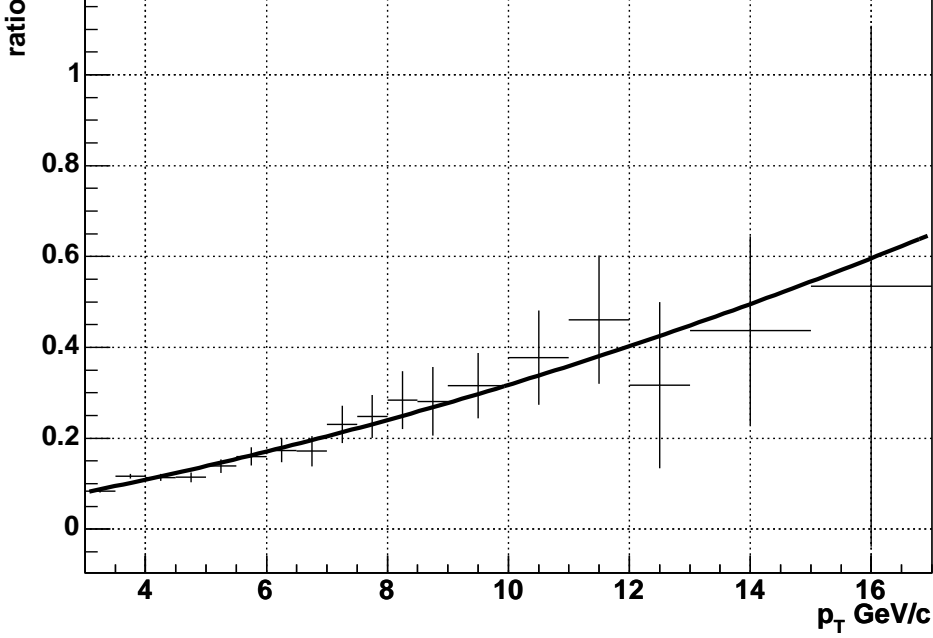


Figure 4.45: Ratio of prompt photon signal to all photon ($N_{\gamma}^{raw}/N_{\gamma}^{all}$). The black line shows a second polynomial function fit to the signal fraction.

The systematic error sources in group B are for all photons ($\Delta N_{\gamma}^{all}/N_{\gamma}^{all}$) and are proportional to W .

B1 The contamination of non-vertex (Section 4.9) and neutral hadron (Section 4.8) is 1%. Those effects are proportional to the W .

The systematic error sources in group C are for π^0 decay photons ($\Delta N_{\gamma}^{\pi^0}/N_{\gamma}^{\pi^0}$) and are proportional to $(W - 1)$.

C1 The error of combinatorial background subtraction is 3%.

C2 The error of conversion and Dalitz correction is 1%.

The systematic error sources in group D are for missing π^0 photon ratio ($\Delta(1 + R)/(1 + R)$) and are proportional to $(W - 1)$.

D1 When the π^0 mass is calculated, the minimum partner photon energy is fixed as 150 MeV. This effect of error is 5% at 3GeV/ c .

D2 When the missing ratio is calculated using the π^0 production function, the error of parameter of this function is propagated to the missing ratio. This error is 5% at 3GeV/c.

D3 The error of π^0 merge effect is about 1%, only for $p_T > 12$ GeV/c.

D4 The errors of geometry and trigger mask are about 1%.

The systematic error sources in group E are for η, ω, η' contribution ($\Delta A/A$) and are proportional to $(W - 1)$.

E1 The error of η, ω, η' contribution 4.6 is calculated as $\Delta A/A = 0.05/(1 + 0.23) = 4\%$.

p_T (GeV/c)	1/W	A1	A3	A*1	B1	B*W	C1	C2	C*(W-1)
3.25	0.0877	10	10.1	14.2	1	11.4	3	1	32.9
3.75	0.102	10	10.1	14.2	1	9.84	3	1	27.9
4.25	0.116	10	10.1	14.2	1	8.61	3	1	24.1
4.75	0.131	10	10.1	14.2	1	7.63	3	1	21.0
5.25	0.146	10	10.1	14.2	1	6.83	3	1	18.4
5.75	0.162	10	10.1	14.2	1	6.16	3	1	16.3
6.25	0.179	10	10.1	14.2	1	5.59	3	1	14.5
6.75	0.196	10	10.1	14.2	1	5.11	3	1	13.0
7.25	0.213	10	10.1	14.2	1	4.69	3	1	11.7
7.75	0.231	10	10.1	14.2	1	4.33	3	1	10.5
8.25	0.249	10	10.1	14.2	1	4.01	3	1	9.52
8.75	0.268	10	10.1	14.2	1	3.73	3	1	8.63
9.5	0.297	10	10.1	14.2	1	3.36	3	1	7.47
10.5	0.338	10	10.1	14.2	1	2.96	3	1	6.19
11.5	0.381	10	10.1	14.2	1	2.63	3	1	5.15
12.5	0.425	10	10.1	14.2	1	2.35	3	1	4.28
14.0	0.495	10	10.1	14.2	1	2.02	3	1	3.22
16.0	0.596	10	10.1	14.2	1	1.68	3	1	2.14

Table 4.5: Table of systematic errors.

p_T (GeV/c)	1/W	D1	D2	D3	D4	D*(W-1)	E1	E*(W-1)	Sum(%)
3.25	0.0877	5	5	0	1	74.3	4	41.6	93.1
3.75	0.102	5	3	0	1	52.3	4	35.3	71.1
4.25	0.116	5	2	0	1	41.7	4	30.4	59.3
4.75	0.131	5	1	0	1	34.5	4	26.5	50.9
5.25	0.146	4	1	0	1	24.7	4	23.3	41.7
5.75	0.162	4	1	0	1	21.9	4	20.6	37.6
6.25	0.179	3	1	0	1	15.2	4	18.4	31.8
6.75	0.196	3	1	0	1	13.6	4	16.4	29.2
7.25	0.213	2	1	0	1	9.05	4	14.8	25.7
7.75	0.231	2	1	0	1	8.16	4	13.3	24.0
8.25	0.249	2	1	0	1	7.38	4	12.0	22.5
8.75	0.268	2	1	0	1	6.69	4	10.9	21.3
9.5	0.297	2	1	0	1	5.79	4	9.45	19.8
10.5	0.338	2	1	0	1	4.80	4	7.84	18.3
11.5	0.381	2	1	0	1	3.99	4	6.51	17.1
12.5	0.425	2	1	1	1	3.58	4	5.41	16.4
14.0	0.495	2	1	1	1	2.69	4	4.07	15.5
16.0	0.596	2	1	1	1	1.79	4	2.71	14.8

Table 4.6: Table of systematic error (continued).

Chapter 5

Results and Discussion

5.1 Results

The invariant cross section of the prompt photon production in the proton-proton collisions at \sqrt{s} of 200 GeV and its statistical and the systematic errors are listed in Table 5.1. Figure 5.1 shows the invariant cross section as a function of p_T with the statistical error and the systematic error.

It can be seen that the wide p_T range from 3.25 GeV/ c to 16 GeV/ c is covered. The 4 orders of magnitude on the invariant cross section is obtained. The spectrum(Figure 5.1) shows a smooth curve as a function of p_T . The slope of this function in lower p_T is steeper than that in higher p_T . This shape is very typical in particle production in high energy particle collisions. The shape of invariant cross section is discussed using the ' x_T scaling' in Section 5.3.

The total systematic error in the cross section is between 14.8% to 93.1% depending on the measured p_T . The main source of the systematic error is uncertainty in the evaluation of the fraction of the missing π^0 photon. The uncertainty of normalization due to luminosity error is 9.7%. In p_T higher than 8.5GeV/ c , the statistical error is larger than the systematic error. The statistical error at the highest p_T is about 43%.

The structure of this chapter is as follows. The obtained invariant cross section is compared with the results from other experiments, which is discussed in Section 5.2. In Section 5.3, the x_T scaling property of the present result is discussed. The comparison of the obtained invariant cross section with NLO pQCD calculation is discussed in Section 5.4. The ratio of the obtained cross section of prompt photon to the cross section of π^0 is discussed in Section 5.5.

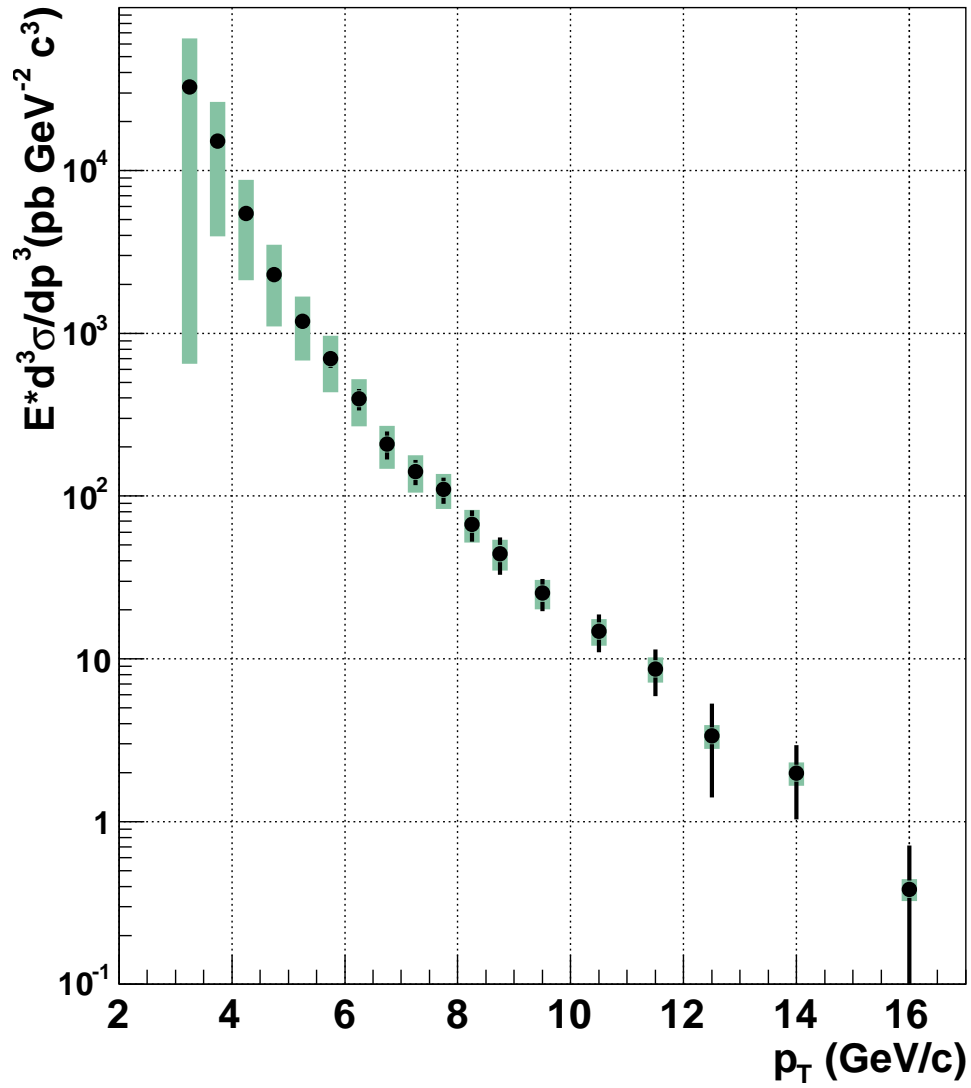


Figure 5.1: Invariant cross section for prompt photon production with statistical error and systematic error. Black line represents statistical error. Color filled band represents systematic error.

5.2 Comparison with Other Experiments

In this section, the present result of the prompt photon production is compared with those from other experiments in different \sqrt{s} at pseudo-rapidity (η) of around 0. The prompt photon production at $\eta \approx 0$ was measured in proton-proton collisions at \sqrt{s} varying from 19.4 to 63 GeV and in proton-anti-proton collisions at \sqrt{s} varying from 546 to 1800 GeV. All the data of other experiments are obtained from the published papers, preprints and HEP data base [126].

Figure 5.2 shows the comparison of the obtained invariant cross section at $\sqrt{s} = 200$ GeV with the results of other proton-proton collision experiments at \sqrt{s} from 19.4 to 63 GeV. Figure 5.3 shows the results of proton-anti-proton collision experiments at \sqrt{s} from 24.3 to 1800 GeV. The data from other experiments are listed in Appendix D. The invariant cross section increases systematically as the energy increases. The local slope at p_T from 1 to 8 GeV/c does not change for the lowest $\sqrt{s} \approx 20$ GeV. But the distributions of invariant cross section show a slight bend at p_T of around 5 GeV/c as \sqrt{s} goes higher, especially for \sqrt{s} more than 200 GeV. The slope at the higher p_T than the bend point becomes flatter than that at lower p_T in those \sqrt{s} regions. This can be described by the hard interaction in hadrons.

5.3 x_T Scaling

In this section, the x_T scaling of the present data together with other experimental results are examined. The fundamental formalism of the particle production from hadron collisions is written as Equation 2.7 in Section 2.1.4. The invariant cross section can be approximated as follows for the particle production at $\eta = 0$ [127];

$$E \frac{d^3\sigma}{dp^3} \approx (\sqrt{s})^{-n} \times F(x_T) \quad (5.1)$$

where n is a constant named as power index. $F(x_T)$ does not depend on \sqrt{s} . x_T is defined as $x_T = 2p_T/\sqrt{s}$. The naive parton model predicts $n = 4$ in the Leading-order and $n = 4 + \alpha$ in the Next-to-leading-order because the dimension of $E \frac{d^3\sigma}{dp^3}$ is GeV^{-4} in the natural system of units. α is the arbitrary constant. There are two assumptions in this approximation. One is that the parton distribution function and fragmentation function is independent of Q^2 , the other is the coupling constant (α_s) is independent of Q^2 . As discussed in Section 2.1, they do depend on Q^2 . Therefore the assumptions are not rigorous. The power index n is expected to decrease as the running coupling constant decreases.

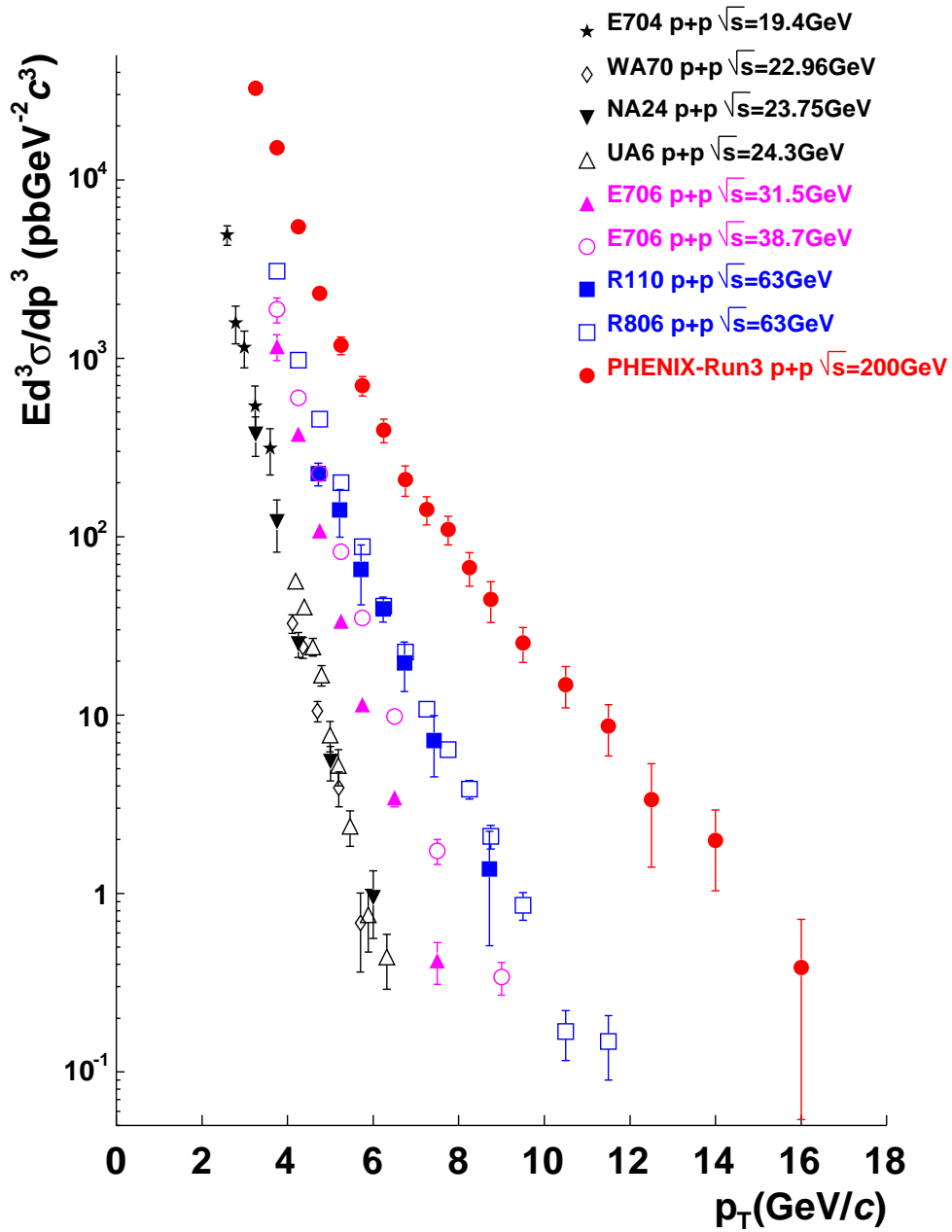


Figure 5.2: Comparison of the obtained invariant cross section at $\sqrt{s} = 200$ GeV with the results of other experiments at \sqrt{s} between 19.4 and 63 GeV in proton-proton collisions.

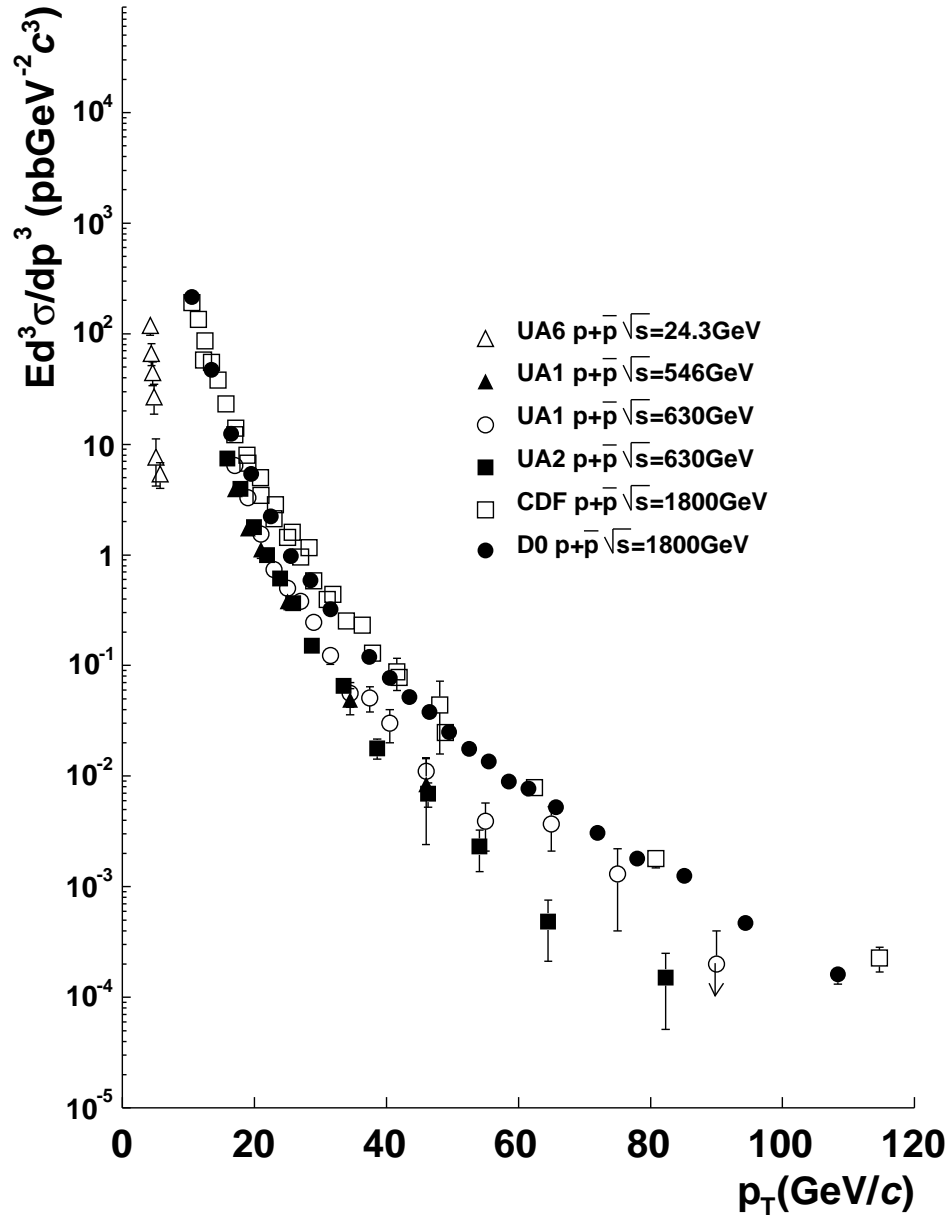


Figure 5.3: The results of other experiments at \sqrt{s} between 24.3 and 1800 GeV are shown.

Figure 5.4 shows a comparison of the obtained invariant cross section with other experimental results at \sqrt{s} from 19.4 to 1800 GeV. The figure shows good agreements in the measured x_T range from 0.015 to 0.5 and in \sqrt{s} range from 19.4 to 1800 GeV at $n = 5.0$.

Figure 5.5 shows cross sections of π^0 production at \sqrt{s} from 62 to 540 GeV. The figure shows good agreements in the measured x_T range from 0.015 to 0.5 and in \sqrt{s} range from 19.4 to 1800 GeV at $n = 6.3$. The n in case of π^0 is larger than the n in case of prompt photon. This indicates that the effect of fragmentation for π^0 production is larger than the prompt photon. Therefore, $n = 5$ is appropriate for the prompt photon production. This scaling property indicates that the obtained result are dominated by the point-like interactions.

5.4 Comparison with NLO pQCD Calculation

The obtained invariant cross section is compared with an NLO pQCD calculation using the CTEQ6M parton distribution function. Figure 5.6 shows the comparison of present data with NLO pQCD calculation. The three solid lines represent the calculation results of NLO pQCD with different scales. The top solid line is calculated with $\mu = 0.5p_T$, the middle one is calculated with $\mu = 1.0p_T$, and the bottom one is calculated with $\mu = 2.0p_T$. The present data are consistent with NLO pQCD calculation within their systematic errors. It can be concluded that the NLO pQCD calculation can describe the obtained invariant cross section. The theoretical curves are slightly less steep than experimental data as a function of p_T . This is an open subject for future theoretical studies.

5.5 Comparison with π^0 cross section

The obtained invariant cross section is compared with the cross section of π^0 [124]. Figure 5.7 shows the ratio of the obtained cross section to the cross section of π^0 . Black line represents statistical error. Color filled band represents systematic error. The ratio increases continuously with increasing p_T . It indicates that the contribution of the prompt photon production to the all photons at high p_T is larger than that at low p_T .

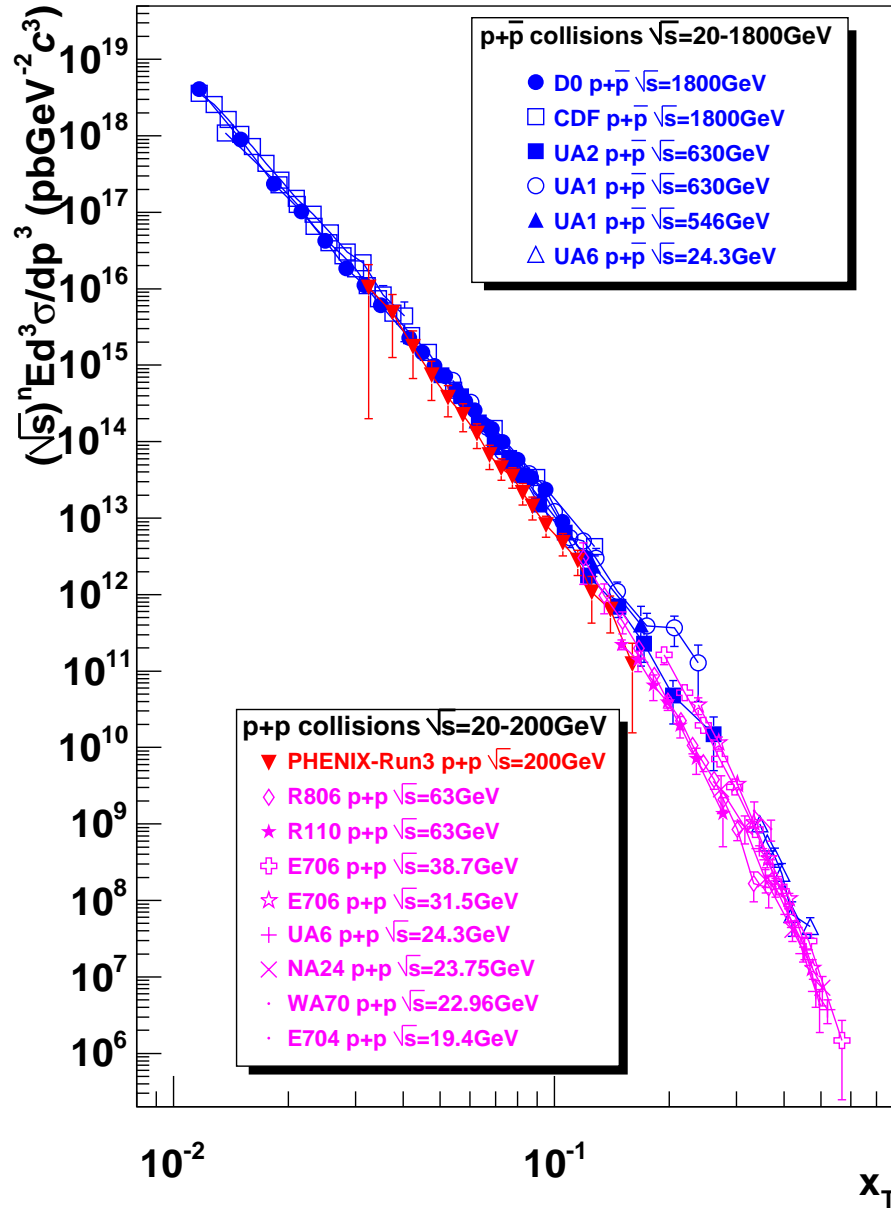


Figure 5.4: Cross section for prompt photon production $(\sqrt{s})^{5.0} \times E \frac{d^3\sigma}{dp^3}$ at \sqrt{s} between 19.4 and 1800 GeV.

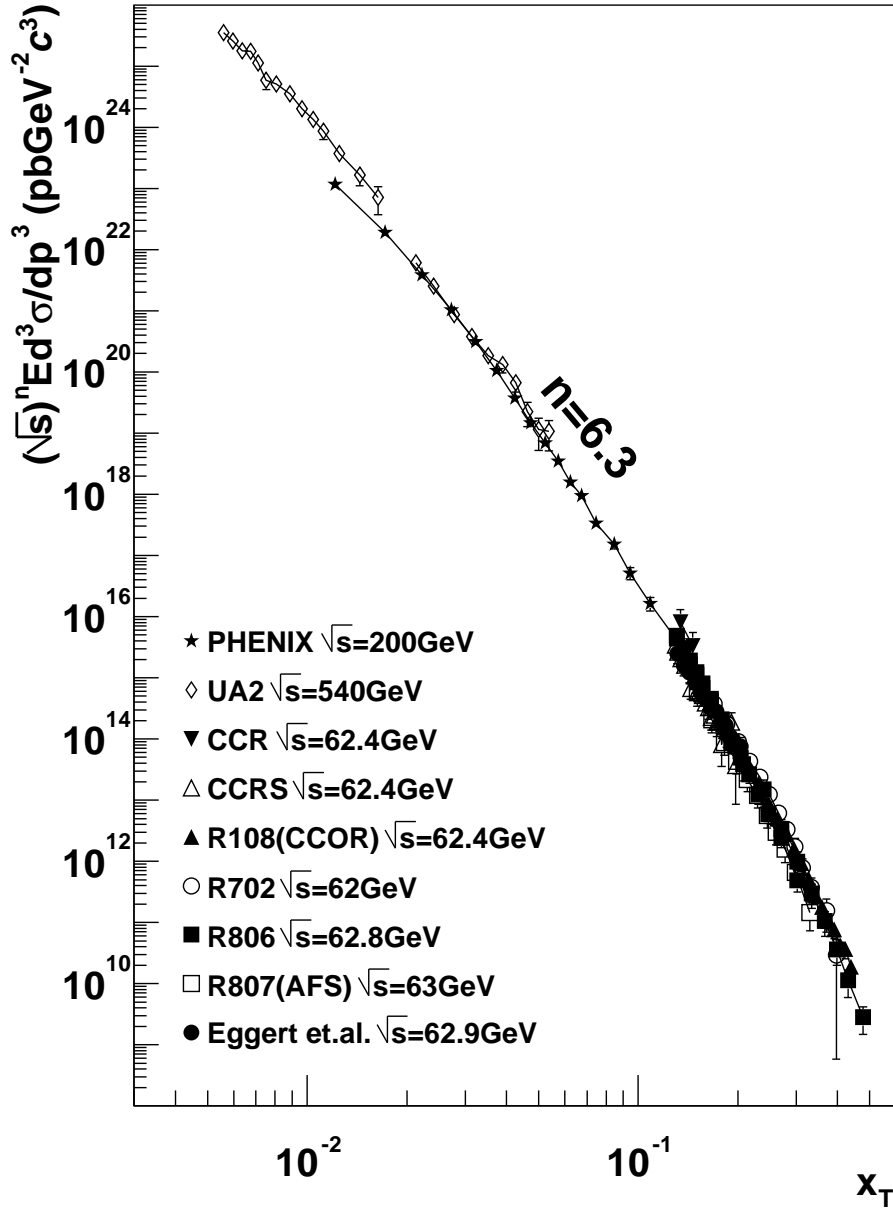


Figure 5.5: Cross section for π^0 production $(\sqrt{s})^{6.3} \times E \frac{d^3\sigma}{dp^3}$ at \sqrt{s} between 62 and 540GeV.

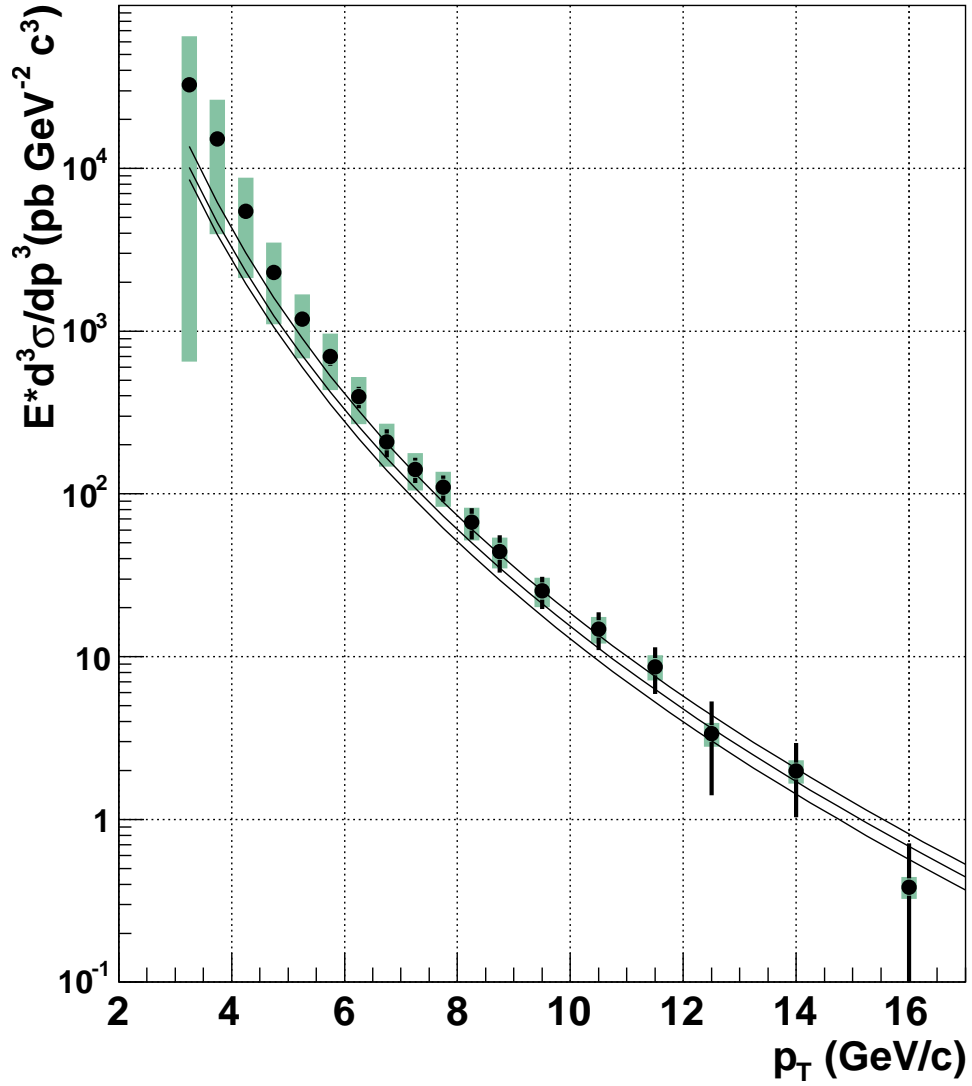


Figure 5.6: Comparison of invariant cross section for prompt photon production at $\sqrt{s} = 200$ GeV with NLO pQCD calculations. The three curves represent NLO calculations with different scales of $0.5p_T$ (top), p_T (middle) and $2p_T$ (bottom).

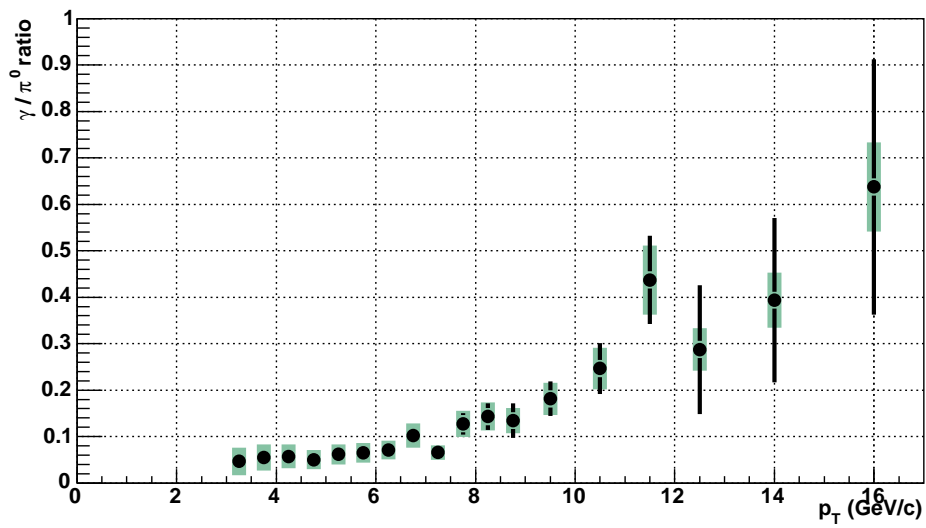


Figure 5.7: The ratio of the obtained cross section for the prompt photon production to the cross section for π^0 . Black line represents statistical error. Color filled band represents systematic error.

p_T (GeV/c)	$Ed^3\sigma/dp^3$ (pb · GeV ⁻² · c ³)	statistical error	systematic error
3.25	32639.8	1378.37	31989.2
3.75	15140.2	696.673	11200.4
4.25	5447.80	379.386	3333.05
4.75	2300.89	220.919	1200.18
5.25	1181.85	134.839	503.407
5.75	700.760	88.7904	267.658
6.25	395.641	59.8011	127.789
6.75	208.500	40.3305	61.6543
7.25	141.583	25.1096	36.7785
7.75	109.847	20.2504	26.6027
8.25	67.0572	14.4147	15.2436
8.75	44.3528	11.4192	9.52345
9.5	25.3371	5.6732	5.14438
10.5	14.8211	3.86247	2.76329
11.5	8.67818	2.76784	1.51313
12.5	3.36185	1.95723	0.558376
14.0	1.98648	0.954647	0.322621
16.0	0.384433	0.330452	0.0590897

Table 5.1: Invariant cross section for prompt photon production in proton-proton collisions at $\sqrt{s} = 200$ GeV with the statistical uncertainty, and the systematic uncertainty for each p_T bin.

Chapter 6

Conclusion

Cross section for production of prompt photon in proton-proton collisions at $\sqrt{s} = 200$ GeV at the PHENIX experiment is reported. This is the prompt photon measurement at the highest energy in the world in the proton-proton collisions. In PHENIX, data with an integrated luminosity of 0.35pb^{-1} have been collected in the run of year 2003 at $\sqrt{s} = 200$ GeV. The analyzed sample consists of 56M events with the high- p_T trigger. The measured p_T range is from 3.25 GeV/c to 16 GeV/c. Prompt photons and photons from hadron decay are detected by the PHENIX Electro-Magnetic Calorimeter (EMCal). The EMCal consists of six sectors of lead scintillator calorimeter and two sectors of lead glass calorimeter. It is located at a radial distance of approximately 5m from the beam axis. Each of these sectors covers the pseudo-rapidity range of $|\eta| < 0.35$ and the azimuthal angle of $\phi = 0.4$ rad.

The conclusions of this thesis are listed as follows:

- The invariant cross section for prompt photon production over 4 order of magnitude in proton-proton collisions at $\sqrt{s} = 200$ GeV is obtained for the wide p_T range from 3.25 to 16 GeV/c. This is the result of prompt photon measurement at the highest energy in the world in the proton-proton collisions. The total systematic error in the cross section is 14.8 % at the highest p_T bin and 93.1 % at the lowest p_T bin. The main source of the systematic error is uncertainty in the estimation of the fraction of the missing π^0 photons. The uncertainty of normalization due to the luminosity error is 9.7%. At p_T higher than 8.5 GeV/c, the statistical error is larger than the systematic error. The statistical error at the highest p_T is about 86%.
- The obtained invariant cross section is compared with the results from other experiments in proton-proton collisions and proton-anti-proton collisions in wide range of \sqrt{s} between 19.4 and 1800 GeV. The present

result as well as those from other experiments are examined in terms of the x_T scaling property. These results can be described by a function of x_T at $n = 5.0$. The scaling property indicates the point-like interaction dominates in the collisions.

- The obtained result is compared with a Next-to-leading-order(NLO) pQCD calculation using the CTEQ6M parton distribution function. The obtained invariant cross section is consistent with NLO pQCD calculation within the systematic error. The NLO pQCD calculation can describe the obtained invariant cross section. The theoretical curves are slightly less steep than experimental data as function of p_T , which is an open subject for future theoretical studies.
- The obtained invariant cross section is compared with the cross section of π^0 . The ratio increases continuously with increasing p_T . It indicates that the contribution of the prompt photon production to the all photons at high p_T is larger than that at low p_T .
- This work provides basis for the study of the polarized gluon distribution in the nucleon. The polarized gluon distribution function will be measured by prompt photon production at RHIC in near future as the luminosity and the beam polarization are being improved.
- This work provides a reference data for Quark Gluon Plasma search in heavy ion collision. One of the possible signal of QGP is jet quenching effect. The parton loses its energy with strong interaction when it goes through the QGP, which is predicted with the QCD calculation. The jet produced in heavy ion collisions are therefore reduced with strong interaction in the QGP matter, while prompt photon produced in heavy ion collisions is not reduced because it dose not interact with strong interaction. That is the jet quenching scenario. Therefore, the prompt photon production in proton-proton collisions is a good reference for QGP study.

Acknowledgement

First of all, I would like to thank Prof. Toshi-Aki Shibata for being my supervisor. He initiated my interest in spin physics and suggested me to participate in the RHIC spin group. His advice on my thesis was essential. Without his support, I could not finish this work.

I wish to thank PHENIX collaboration. I would like to appreciate PHENIX EMCal group which helped my EMCal energy calibration work. I would like to appreciate prompt photon analysis group, Dr. Yasuyuki Akiba, Dr. Yuji Goto, Dr. Alexander Bazilevsky, Dr. Kensuke Okada, and Dr. Hisayuki Torii. Dr. Yasuyuki Akiba invited me to prompt photon analysis first and provided the basic idea of this analysis. Dr. Kensuke Okada and Dr. Hisayuki Torii carried out independent prompt photon analysis, therefore the discussion with them is very useful for me. Dr. Alexander Bazilevsky helped me with his useful photon Monte Carlo simulation tool. Dr. Yuji Goto helped me for the π^0 analysis as a preparation of prompt photon analysis. The work of Optical Alignment system would not be carried out without help of PHENIX Muon group, and especially I wish to thank Dr. Hideyuki Kobayashi and Dr. Atsushi Taketani. Their suggestions and help are very instructive for my analysis.

I would like to thank Dr. Hideto Enyo of RIKEN for his support. Dr. Gerry Bounce, helped me in my research at BNL. This thesis work was supported in part by RIKEN and RIKEN BNL Research Center.

I am grateful to all staff and secretaries, T. A. Heinz, P. Esposito, Taeko Ito, Noriko Kiyama, Machiko Muroi, Chiharu Shimoyamada, and Jun Nakamura, for all their heartfelt support. Without their support, I could not have a joyful time at BNL.

Sharing the house at BNL with a few people from Japanese institutes has enabled me to spend a joyful time. I appreciate to all my colleagues and friends. I would like to thank Dr. Kyoichiro Ozawa. He always helped me and strongly encouraged me. I would like to thank people of RIKEN Radiation Laboratory. The cheerful and friendly talk with them is very interesting for me.

I would like to thank people of Shibata Laboratory of Tokyo Institute of Technology, Dr. Yoshiyuki Miyachi and graduate students, Tomohiro Kobayashi, Kenichi Nakano, Taiki Hasegawa, Hiroki Kanou, Hideyuki Takei, Imazu Yoshimitsu, Kouichi Sakashita, Taisuke Koroku, Yutaka Fujiwara and Tetsuya Ishikura. The discussion with them is very useful and interesting for me. They helped me to write the doctor thesis.

I would like to thank my family, Masanori and Yae, for their support to my continuing this work. I could not finish this work without their support.

Appendix A

PHENIX Coordinate System

The PHENIX coordinate system is shown in Figure A.1. The Z axis is defined as a direction of the beam line. The direction from the vertex point to the north Muon Arm is defined as positive. The X and Y axis are defined as Figure A.1. The direction from the vertex point to the west Central Arm is defined as positive. The angle ϕ is defined in X-Y plane as follows at (x,y,z);

$$\phi = \tan^{-1} \left(\frac{y}{x} \right) \quad (\text{A.1})$$

The angle θ is defined in Y-Z plain as follows at (x,y,z);

$$\theta = \tan^{-1} \left(\frac{y}{z} \right) \quad (\text{A.2})$$

The direction of particle is determined with ϕ and θ . In the high energy reaction, y is often used. y is called rapidity and is defined as follows;

$$y = \frac{1}{2} \ln \frac{E + p_z}{E - p_z} \quad (\text{A.3})$$

where E is the energy of particle and p_z is the momentum of z-component. When the particle energy is large, the mass of particle is negligible. In this case,

$$y = \frac{1}{2} \ln \frac{1 + p_z/E}{1 - p_z/E} \quad (\text{A.4})$$

$$= \frac{1}{2} \ln \frac{1 + \cos \theta}{1 - \cos \theta} \quad (\text{A.5})$$

$$= \frac{1}{2} \ln \frac{\cos^2(\theta/2)}{\sin^2(\theta/2)} \quad (\text{A.6})$$

$$= -\ln \left(\tan \left(\frac{\theta}{2} \right) \right) \quad (\text{A.7})$$

The pseudo-rapidity is defined as:

$$\eta = -\ln\left(\tan\left(\frac{\theta}{2}\right)\right) \quad (\text{A.8})$$

The rapidity y can be approximated with pseudo-rapidity η when E is large.

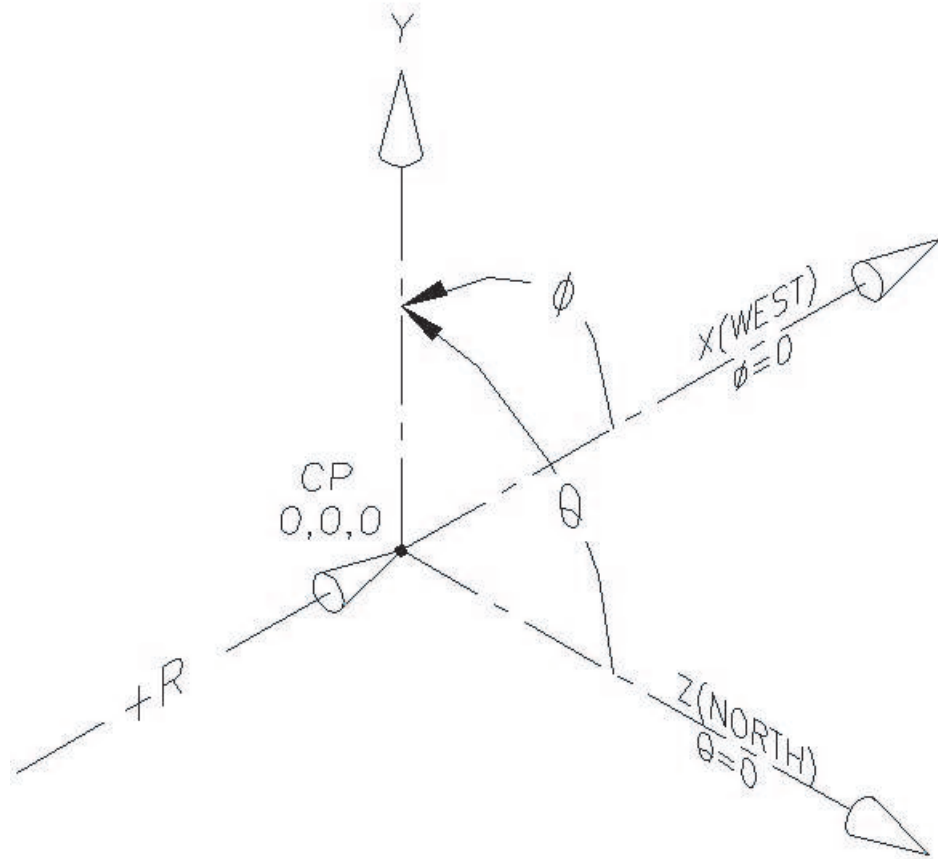


Figure A.1: The PHENIX coordinate system.

Appendix B

Kinematics of π^0 Decay

In the center of mass system of π^0 two photons from π^0 decay are emitted in the opposite direction. The photon energy E_γ^* and photon momentum p_γ^* are equal to $(1/2)m_{\pi^0}$, where m_{π^0} is mass of π^0 . When the angle of photon in the center of mass system is θ^* , the energy of photon in the laboratory system is expressed with Lorentz transformation;

$$E_1 = \gamma_0(E_\gamma^* + \beta_0 p_\gamma^* \cos\theta^*) \quad (\text{B.1})$$

$$= \frac{1}{2}m_{\pi^0}\gamma_0(1 + \beta_0 \cos\theta^*) \quad (\text{B.2})$$

where β_0 is the π^0 velocity in the laboratory system. Because the π^0 decay in the center of mass system is isotropic, the distribution of emitted angle of photon $dN/d\cos\theta^*$ is constant, where N is the number of photon. Therefore, the distribution of photon energy in the laboratory system is written as follows;

$$\frac{dN}{dE_1} = \frac{dN}{d\cos\theta^*} \cdot \frac{d\cos\theta^*}{dE_1} \quad (\text{B.3})$$

$$= \frac{dN}{d\cos\theta^*} \cdot \frac{1}{\gamma_0 E_\gamma^* \beta_0} \quad (\text{B.4})$$

$$= \text{const.} \quad (\text{B.5})$$

The maximum and minimum energy of photon in the laboratory system are written as follows;

$$E_{1max} = \frac{1}{2}m_{\pi^0}\gamma_0(1 + \beta_0) \quad (\text{B.6})$$

$$E_{1min} = \frac{1}{2}m_{\pi^0}\gamma_0(1 - \beta_0) \quad (\text{B.7})$$

$$(\text{B.8})$$

The angle of photon in the laboratory system is written as follows;

$$\sin\theta_1 = \frac{\sin\theta^*}{\gamma_0(1 - \beta_0\cos\theta^*)} \quad (\text{B.9})$$

The θ_1 becomes minimum with $\theta^* = \pi/2$. Therefore the angle between two photon from π^0 decay in the laboratory system ϕ also becomes minimum. The minimum value of ϕ is written as follows;

$$\sin\left(\frac{\phi_{\min}}{2}\right) = 1/\gamma_0 \quad (\text{B.10})$$

The ϕ can be written using the two photon energy in the laboratory by Equation 4.10 as follows;

$$\sin\left(\frac{\phi}{2}\right) = \frac{m_{\pi^0}}{2\sqrt{E_1 E_2}} \quad (\text{B.11})$$

Appendix C

Prompt Photon Production at Leading Order

The quark gluon Compton Scattering process ($gq \rightarrow \gamma q$) is described in this chapter. This process is very similar to photon electron Compton scattering in QED, therefore $\gamma e^- \rightarrow \gamma e^-$ is described first.

The wave function of electron is written as $ue^{-ip \cdot x}$ and the wave function of photon is written as $\epsilon_\mu e^{-ik \cdot x}$. The amplitude can be written by Feynman rule as follows;

$$-iM_1 = \bar{u}^{s'}(p') \left[\epsilon_\nu'^* (ie\gamma^\nu) \frac{i(\not{p} + \not{k} + m)}{(p+k)^2 - m^2} (ie\gamma^\mu) \epsilon_\mu \right] u^{(s)}(p) \quad (\text{C.1})$$

$$-iM_2 = \bar{u}^{s'}(p') \left[\epsilon_\nu (ie\gamma^\mu) \frac{i(\not{p} - \not{k}' + m)}{(p-k')^2 - m^2} (ie\gamma^\nu) \epsilon_\nu'^* \right] u^{(s)}(p) \quad (\text{C.2})$$

where p, s and p', s' represent the momentum and spin state of the coming electron and the outgoing electron, k, ϵ and k', ϵ' represent the momentum and polarization vector of the coming photon and the outgoing photon. Here Mandelstam variables are defined as follows;

$$s = (k+p)^2 = 2k \cdot p = 2k' \cdot p' \quad (\text{C.3})$$

$$t = (k-k')^2 = -2k \cdot k' = -2p \cdot p' \quad (\text{C.4})$$

$$u = (k-p')^2 = -2k \cdot p' = -2p \cdot k' \quad (\text{C.5})$$

$$(\text{C.6})$$

By trace theorem, the spin averaged amplitude of Compton Scattering can be written as follows;

$$\overline{|M|^2} = \overline{|M_1 + M_2|^2} = -32\pi^2\alpha^2 \left(\frac{u}{s} + \frac{s}{u} \right) \quad (\text{C.7})$$

Here, to write the amplitude of the quark gluon Compton Scattering process ($gq \rightarrow \gamma q$), α^2 is replaced with $e_q^2 \alpha \alpha_s$ and multiply Equation C.7 by color factor, where e_q is the electric charge of quark and α_s is the coupling constant of strong interaction. Thus the amplitude of the quark gluon Compton Scattering process is obtained.

Appendix D

Cross Section from Other Experiments

In this chapter, the cross sections from other experiments are listed.

p_T	cross section (pb GeV ⁻² c ³)	statistical error	systematic error
3.25	375	93.0	170.0
3.75	121	39.0	29.0
4.25	25.0	4.0	7.5
5.00	5.48	1.20	1.10
6.00	0.950	0.390	0.060

Table D.1: Data table of invariant cross sections of prompt photon by NA24 collaboration at the beam momentum of 300 GeV ($\sqrt{s} = 23.75$ GeV) [82].

p_T	cross section (pb GeV ⁻² c ³)	statistical error	systematic error
4.72	225	33	0
5.22	141	42	0
5.72	65.6	24.2	0
6.23	39.4	6.3	0
6.73	19.6	6.1	0
7.42	7.21	2.72	0
8.72	1.37	0.86	0

Table D.2: Data table of invariant cross sections of prompt photon by R110 collaboration at $\sqrt{s} = 63$ GeV [80].

p_T	cross section (pb GeV ⁻² c ³)	statistical error	systematic error
3.75	3070	0	1690
4.25	977	0	410.0
4.75	454.0	5.0	145.0
5.25	200.0	3.0	54.0
5.75	87.8	2.2	21.9
6.25	40.8	1.5	9.7
6.75	22.6	1.1	5.1
7.25	10.8	0.7	2.4
7.75	6.41	0.60	1.42
8.25	3.84	0.46	0.84
8.75	2.09	0.32	0.46
9.50	0.858	0.153	0.196
10.50	0.168	0.052	0.048
11.50	0.148	0.058	0.035

Table D.3: Data table of invariant cross sections of prompt photon by R806 collaboration at $\sqrt{s} = 63$ GeV.

p_T	cross section (pb GeV ⁻² c ³)	statistical error	systematic error
17.00	3.91	0.37	0.44
19.00	1.74	0.24	0.17
21.00	1.12	0.19	0.10
25.00	0.38	0.06	0.03
34.50	0.049	0.013	0.002
46.00	0.0084	0.0060	0.0002

Table D.4: Data table of invariant cross sections of prompt photon by UA1 collaboration at $\sqrt{s} = 546$ GeV [84].

p_T	cross section (pb GeV ⁻² c ³)	statistical error	systematic error
17.00	6.42	0.57	1.12
19.00	3.30	0.33	0.52
21.00	1.54	0.20	0.22
23.00	0.74	0.07	0.09
25.00	0.50	0.05	0.06
27.00	0.381	0.047	0.038
29.00	0.246	0.037	0.022
31.50	0.123	0.021	0.010
34.50	0.056	0.014	0.004
37.50	0.051	0.013	0.003
40.50	0.030	0.010	0.002
46.00	0.0111	0.0035	0.0004
55.00	0.0039	0.0018	0.0001
65.00	0.0037	0.0016	0.0000
75.00	0.0013	0.0009	0.0000
90.00	0.0002	0.0002	0.0000

Table D.5: Data table of invariant cross sections of prompt photon by UA1 collaboration at $\sqrt{s} = 630$ GeV [84].

p_T	cross section (pb GeV ⁻² c ³)	statistical error	systematic error
15.9	7.46	0.410	1.41
17.9	3.97	0.251	0.671
19.9	1.79	0.156	0.299
21.9	0.992	0.0713	0.159
23.9	0.615	0.0500	0.0793
25.9	0.366	0.0362	0.0451
28.7	0.151	0.0160	0.0182
33.5	0.0657	0.00728	0.00769
38.6	0.0179	0.00367	0.00168
46.3	0.00694	0.00171	0.000750
54.1	0.00231	0.000936	0.000349
64.5	0.000484	0.000272	0.0000576
82.3	0.000151	0.0000999	0.0000145

Table D.6: Data table of invariant cross sections of prompt photon by UA2 collaboration at $\sqrt{s} = 630$ GeV [85].

p_T	cross section (pb GeV ⁻² c ³)	statistical error	systematic error
4.19	56.3	4.9	0
4.39	40.3	3.7	0
4.59	24.1	2.7	0
4.79	16.7	2.2	0
4.99	7.7	1.5	0
5.19	5.2	1.2	0
5.46	2.37	0.53	0
5.89	0.76	0.29	0
6.32	0.44	0.15	0
7.07	0.00	0.03	0

Table D.7: Data table of invariant cross sections of prompt photon by UA6 collaboration at the beam momentum of 315 GeV ($\sqrt{s} = 24.3$ GeV) [77].

p_T	cross section (pb GeV ⁻² c ³)	statistical error	systematic error
4.2	55.5	13.7	11.1
4.4	28.9	8.8	5.8
4.6	16.3	6.6	3.3
4.8	9.6	4.8	1.9
5.1	6.0	2.0	1.2
5.7	1.2	0.5	0.2

Table D.8: Data table of invariant cross sections of prompt photon by UA6 collaboration at the beam momentum of 315 GeV ($\sqrt{s} = 24.3$ GeV) [78].

p_T	cross section (pb GeV ⁻² c ³)	statistical error	systematic error
4.11	32.612	3.930	8.481
4.36	23.988	3.254	5.712
4.70	10.540	1.375	2.139
5.20	3.920	0.867	0.944
5.70	0.683	0.320	0.218

Table D.9: Data table of invariant cross sections of prompt photon by WA70 collaboration at the beam momentum of 280 GeV ($\sqrt{s} = 22.3$ GeV) [81].

p_T	cross section (pb GeV ⁻² c ³)	statistical error	systematic error
12.3	57.7134	5.37019	0
17	12.1714	0.35578	0
19	6.74356	0.175919	0
21	3.47131	0.113689	0
23	2.13142	0.0830425	0
25	1.43885	0.0636659	0
27	0.960883	0.0471599	0
29	0.581774	0.0329306	0
31	0.393804	0.0282389	0
33.9	0.252128	0.0150244	0
37.9	0.129768	0.010079	0
41.9	0.0778729	0.00721749	0
48.9	0.0247698	0.00247373	0
62.4	0.00788171	0.000816229	0
80.8	0.00179454	0.000313208	0
114.7	0.000226189	5.68941e-05	0

Table D.10: Data table of invariant cross sections of prompt photon by CDF collaboration at $\sqrt{s} = 1800$ GeV [86].

p_T	cross section (pb GeV ⁻² c ³)	statistical error	systematic error
10.5	215.251	4.41114	0
13.5	47.2778	1.80387	0
16.5	12.4438	0.865277	0
19.5	5.39528	0.54769	0
22.5	2.22831	0.107525	0
25.5	0.979955	0.0686593	0
28.5	0.586396	0.0519938	0
31.5	0.322877	0.0380479	0
37.4	0.119586	0.00234491	0
40.5	0.0774209	0.00183138	0
43.5	0.0519572	0.00147822	0
46.5	0.0379942	0.00125278	0
49.5	0.0249519	0.00100322	0
52.5	0.0176749	0.000809466	0
55.5	0.0135362	0.000725562	0
58.5	0.00897852	0.000584964	0
61.5	0.00771237	0.000535725	0
65.7	0.00525704	0.000314938	0
72	0.00307276	0.000221062	0
78	0.0017957	0.000163246	0
85.	1 0.00125312	0.00011222	0
94.4	0.000472099	6.74427e-05	0
108.4	0.000161514	2.93662e-05	0

Table D.11: Data table of invariant cross sections of prompt photon by D0 collaboration at $\sqrt{s} = 1800$ GeV [87].

p_T	cross section (pb GeV ⁻² c ³)	statistical error	systematic error
2.59	4900	610	490
2.79	1580	380	250
2.99	1150	270	130
3.24	539	160	59
3.59	312	91	27

Table D.12: Data table of invariant cross sections of prompt photon by E704 collaboration at the beam momentum of 200 GeV ($\sqrt{s} = 19.4$ GeV) [79].

p_T	cross section (pb GeV ⁻² c ³)	statistical error	systematic error
3.75	1160	190	220
4.25	375	30	62
4.75	107.6	4.5	1.6
5.25	33.6	2.2	4.4
5.75	11.4	1.1	1.4
6.50	3.43	0.37	0.42
7.50	0.42	0.11	0.05
9.00	0.010	0.015	0.001

Table D.13: Data table of invariant cross sections of prompt photon by E706 collaboration at the beam momentum of 530 GeV ($\sqrt{s} = 31.5$ GeV) [76].

p_T	cross section (pb GeV ⁻² c ³)	statistical error	systematic error
3.75	1880	300	380
4.25	600	44	10
4.75	225.5	9.4	3.4
5.25	82.2	4.4	11
5.75	35.0	2.4	4.4
6.50	9.80	0.74	1.2
7.50	1.73	0.28	0.20
9.00	0.339	0.070	0.039
11.00	0.017	0.014	0.002

Table D.14: Data table of invariant cross sections of prompt photon by E706 collaboration at the beam momentum of 800 GeV ($\sqrt{s} = 38.7$ GeV).

Appendix E

Optical Alignment System for Muon Trackers

A micron-precision optical alignment system (OASys) for the PHENIX muon tracking chambers has been developed. To ensure the required mass resolution of vector meson detection, the relative alignment between three tracking station chambers must be monitored with a precision of $25\ \mu\text{m}$. The OASys is a straightness monitoring system comprised of a light source, lens and CCD camera, used for determining the initial placement as well as for monitoring the time dependent movement of the chambers on a micron scale.

E.1 Optical Alignment System (OASys)

The muon momentum is determined by measuring the displacement of a muon hit position at the station 2 chamber with respect to a straight line between those at stations one and three; therefore, only the relative straightness must be known to high accuracy. The absolute placement of the chambers is surveyed with respect to a PHENIX hall monument system and has accuracy of 1-2mm. The absolute positions of the chambers need to be known only to a few mm, but the relative alignment of the chambers to each other must be known to much higher precision than the chamber resolution. One prime task of the OASys is to measure the relative alignment after installing the chambers in the muon magnet. In addition, real-time monitoring of the relative straightness is required for correcting the motions of the chambers. To fulfill this requirement, the OASys must be able to measure the chamber position in the time span of minutes through out the data taking within a $25\ \mu\text{m}$ accuracy.

The OASys is a straightness monitor consisting of a fiber optic divergent

light source at station one, a convex lens at station two, and a CCD camera at station three. Any deflection at station 1, 2, or 3 causes a displacement of the focal center from the center point on the CCD with a magnification factor of around 2.5 for our system. If the measured deflection is always attributed to the movement of station 2, then the relative misalignment of the three stations is accounted for. There are seven OASys beams surrounding each octant chamber, therefore, there are $7 \times 8 = 56$ OASys beams in total for one muon arm, as shown in Figure E.2. By combining the seven OASys beams for one octant chamber, the translational misalignment of the chambers, as well as rotational and linear temperature expansions, can be measured. The present system measures the relative chamber positions only in X-Y directions (within the plane parallel to the chamber plane). The contribution of the misalignment in the Z direction to the momentum resolution is negligible to that of misalignment in X-Y directions. Therefore, an initial placement with an accuracy of about 2 mm is sufficient for our system.

The light source block consists of a fiber optic cable, cable terminator and mounting block. The mounting block is precisely pinned to the chamber frame and the cable terminator is located in the mounting block by a special procedure described in Sec.3. We use a 15m-long, core/cladding diameter = $62.5/125 \mu\text{m}$ multi-mode fiber optic cable with a FC connector at the chamber-side end, and bare fiber finish at the light source box side. The custom-made mounting block is designed to hold and tune the position of the FC fiber connector. A bundle of 56 fiber optic cables is connected to the light source box (FiberPro150, High Sierra Lighting). A 150 watt metal halide high-intensity discharge lamp with an average life of 6000 hours is used.

The lens block consists of a convex lens, a lens holder with an XY translation stage, and a mounting block. Because the OASys beams surround the chamber frame, they have different focal lengths. To accommodate various focal lengths, we have chosen to use single commercial lenses with focal lengths differing in steps of 100mm. A typical distance between the light source and lens is about $l_1 = 1200\text{mm}$, and between the lens and CCD camera is about $l_2 = 700\text{mm}$. The required focal length f of the lens is determined by $1/f = 1/l_1 + 1/l_2$. A typical focal length for our system is about 700mm. We use 1cm diameter plano convex glass lenses (MELLES GRIOT, Plano-Convex Glass Lens) of 600, 700, and 800mm focal lengths. The use of this series of lenses enables most of the OASys beams to produce a single sufficiently sharp focal image at the CCD position. However, some of the OASys beams with poorly focused lenses produce a concentric ring interference pattern on the CCD image. Some of them even exhibit destructive interference at the center point. These poorly focused OASys beams have broad, relatively low-intensity focal images. However, the center positions of the broad images are determined

well by our readout DAQ system described in Sec.4. The lenses are mounted inside a small ring-like lens-holding cell (MELLES GRIOT, Optical Component Cell). The placement of the lens into the lens holding cell is achieved by using an XY positioning device to center the lens. Precision pins accurately hold the lens holding cell in the lens block and the lens block is accurately pinned to the chamber frame. The lens-holding cells are set inside the XY positioning block (MELLES GRIOT, Y-Z Positioner for Optical Component Cells) which is attached on the mounting block with precision alignment pins. The same as for the light source block, the mounting block is placed on the chamber frame using precision alignment pins.

The CCD camera block consists of the CCD camera, camera holder and mounting block. The use of precision alignment pins ensures connection between the camera holder and the mounting block, and between the mounting block and the station three chamber frame. Considering the possible initial misplacement of the chamber position inside the muon magnet, the expected center position of the focal image on the CCD camera can be displaced from the camera center point by distances of a few mm. To allow for the possibility of a wide dynamic position range, we use a CCD camera (HITACHI DENSHI, KP-M1U) that has a 8.8×6.6 mm ($768(\text{H}) \times 493(\text{V})$ pixels) effective region. The pixel size is $11.0(\text{H}) \mu\text{m} \times 13.0(\text{V}) \mu\text{m}$. The video signal is sent through the EIA video format to the DAQ system.

E.2 Results

Sample CCD images are shown in Figure E.3 and Figure E.4. Figure E.3 represents CCD images for well focused OASys beam channels with sharp focal images. In contrast, Figure E.4 represents that for weakly focused channels with typical broad focal images. Because the focal image intensity for the broad images is very low, it is difficult to recognize even the existence of the focal image. In Figure E.4, we can see a clear multi-ring interference pattern at the intensified figure. The X-dimensional and Y-dimensional sliced histograms generated by the DAQ PC are also shown beside the image. Final Gaussian fitting curves and the window cut regions are also drawn. In spite of the small S/N ratio for the broad focus image, the wide and low peak is well identified by our system. Since these systems are located inside the muon magnet surrounded by steel plates with small cable throughput holes, there is still room to further reduce background light by shielding the cable holes. The image intensity can also be improved by modifying the light source box and the fiber distributor. However, our results show that the current system is satisfactory. We measured the focal position resolution as shown in Figure

E.5. Peak position distributions for 1000 samples taken within 30 minutes for the typical sharp channel and for the typical broad channel are displayed. The measured resolution is $1.4 \mu\text{ m}$ for the sharp channel, and $3.1 \mu\text{ m}$ for the broad channel. Considering the required focal position resolution of $25 \mu\text{ m}$, the results are excellent.

The system has been running for almost one year in a stable operation since its installation for the south muon arm early in 2000, taking data every hour. Figure E.6 shows an example of the history plot of the peak position over a period of 18 days. Both horizontal (azimuthal) and vertical (radial) movements are plotted in Figure E.6. They are well correlated with each other, indicating that deformation is parallel to a direction between horizontal and vertical axes at the OASys beam position. The magnitudes of the deformations are about $10 \mu\text{ m}$ for the horizontal direction and $50 \mu\text{ m}$ for the vertical direction, which represents large radial deformation. By combining the peak position data from all the OASys beam channels, we can analyze the chamber deformation mode. Such off-line analysis aimed at improvements of the muon-detecting position resolution within the required precision is ongoing. Most of the focal position movements can be understood to be a result of temperature change. In Figure E.6, the room temperature measured inside the muon magnet is also plotted. A clear correlation between the temperature and the peak positions is seen. Although an air-conditioning system is used inside the experimental hall, the room temperature varies from about 21°C to 22.5°C . The results show that the temperature dependence of the movements is about $70 \mu\text{m}/^\circ\text{C}$. Considering the possible large change of air temperature without air conditioning, it can be said that temperature control is a key for maintaining precise chamber geometries. It should be mentioned that the peak position also depends on the magnetic field inside the muon magnet. It is mainly because the temperature depends on the magnetic field condition or the electric current in the magnet coil. Therefore, stable magnet condition is also required.

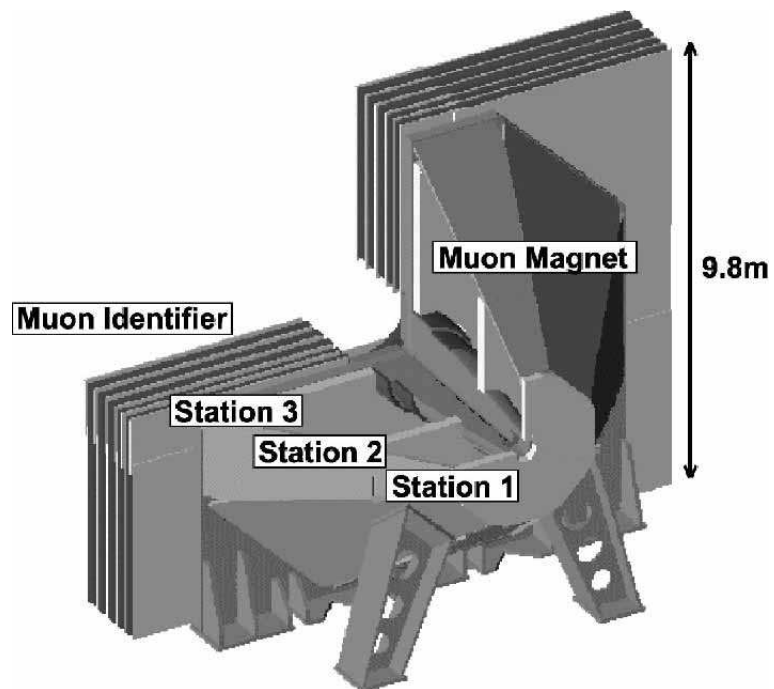


Figure E.1: One arm of the PHENIX muon detector. Three stations of the tracking chambers are placed inside the muon magnet. Each station consists of eight octant cathode strip chamber [128].

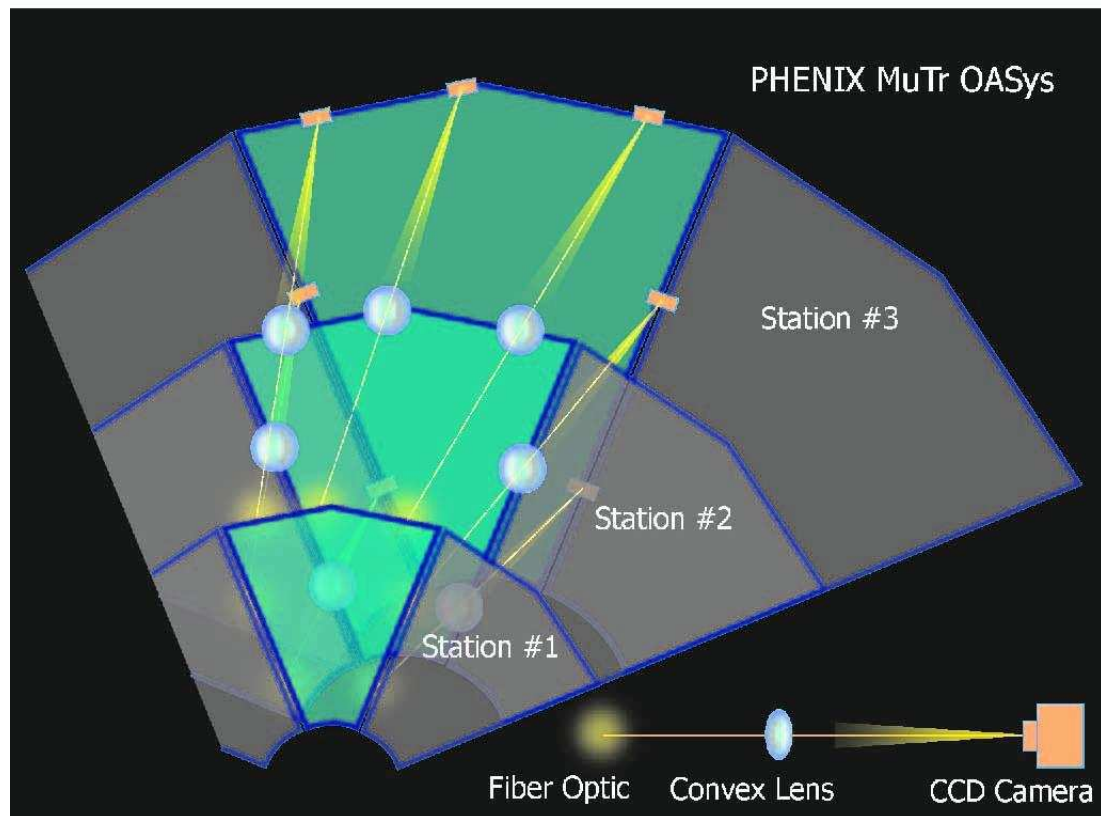


Figure E.2: Overview of the OASys. Seven OASys beams, from the light source, through the lens to the CCD camera, surround one octant chamber. There are $7 \times 8 = 56$ OASys beams in total for one muon arm. Relative straightness is measured from the focal image position on the CCD camera [128].

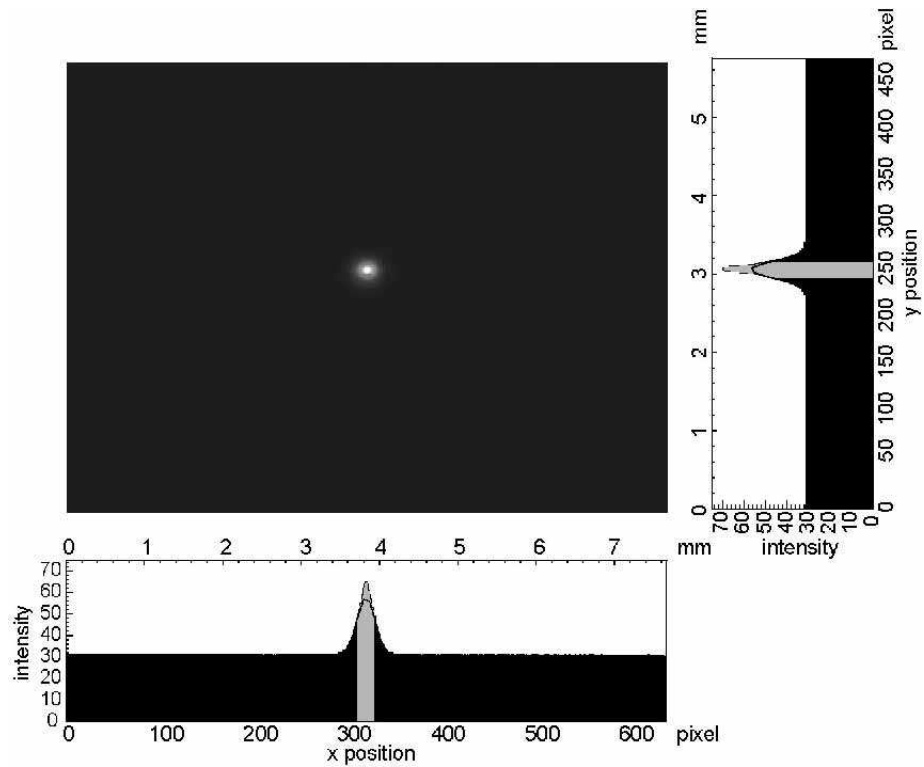


Figure E.3: Sample of focal image on the CCD, for a typical sharp-focus channel. Sliced X- and Y-dimensional light intensity histograms are also shown beside the image. The solid curves are the results of Gaussian fitting. The “window cut” regions ignored by the Gaussian fittings are indicated as the gray regions around the peaks [128].

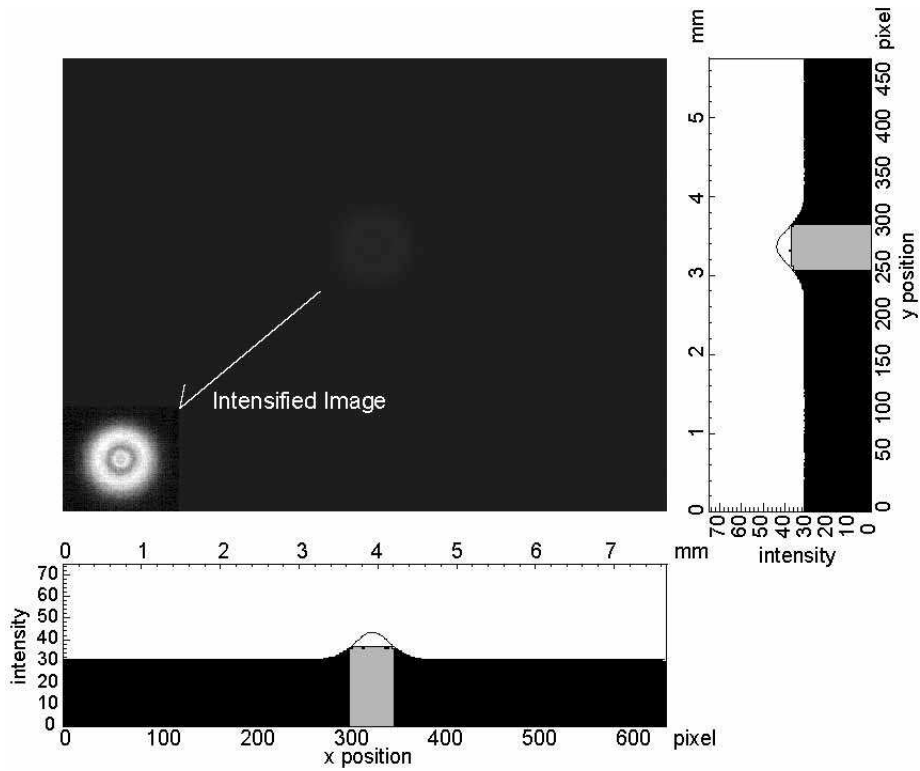


Figure E.4: Sample of focal image on the CCD for a typical broad-focus channel. Because the raw CCD image is too weak for the focal image to be recognized, an intensified image is also shown at the bottom left corner. The sliced X- and Y-dimensional light intensity histograms show that the wide, weak peaks can be clearly identified. The window cut indicated by the gray region is indispensable because of its highly deformed peak shape [128].

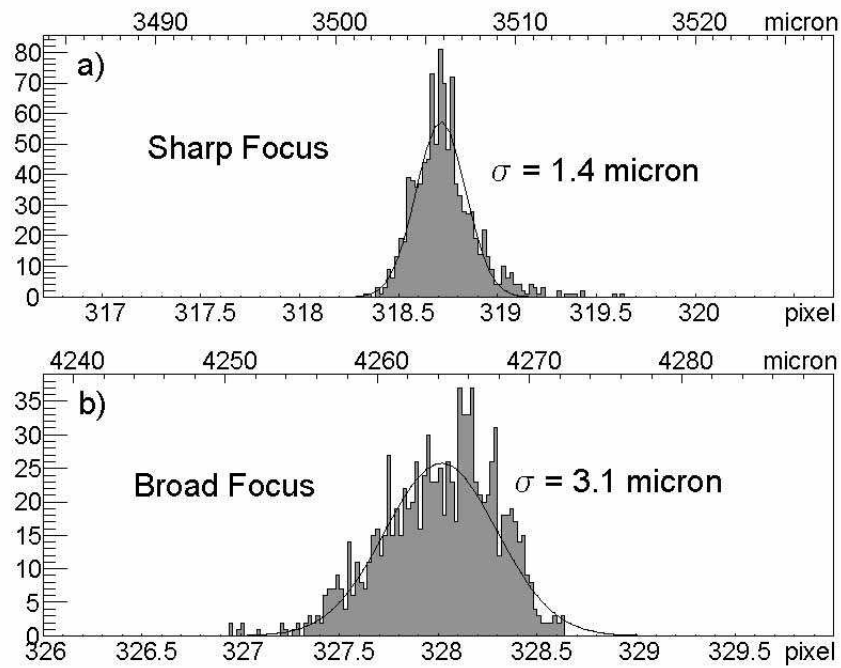


Figure E.5: Peak position distributions for the focal position resolution measurements: a) typical sharp-focus channel and b) typical broad-focus channel. One thousand events are taken for each channel. The width σ of the Gaussian-like peaks indicate the position determination resolution of 1.4 and 3.1 μm [128].

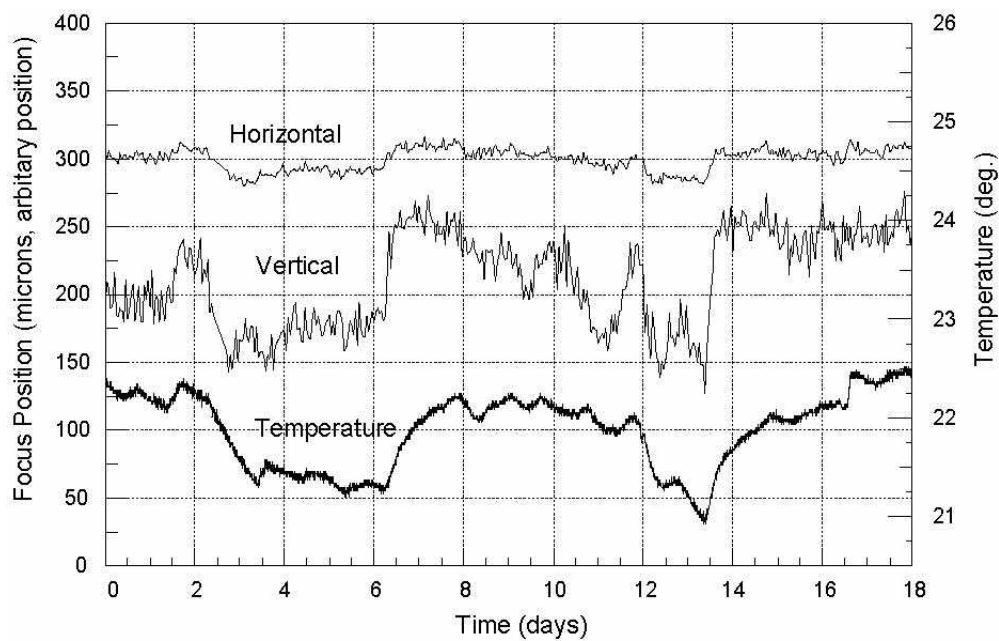


Figure E.6: Time dependent motions of the relative focal positions are shown for a period of 18 days. Both horizontal and vertical directional focal positions are plotted with arbitrary position offsets. Room temperature measured near the chambers is also plotted [128].

Bibliography

- [1] J. J. Thomson, *Phil. Mag.* **44**, 293 (1897).
- [2] J. J. Thomson, *Nature* **55**, 453 (1897).
- [3] E. Rutherford, *Phil. Mag.* **21**, 669 (1911).
- [4] J. Chadwick, *Nature* **129**, 312 (1932).
- [5] H. Yukawa, *Proc. Phys. Math. Soc. Jap.* **17**, 48 (1935).
- [6] G. P. S. Occhialini, C. F. Powell, *Nature* **159**, 186 (1947).
- [7] S. L. Glashow, *Nucl. Phys.* **22**, 579 (1961).
- [8] S. Weinberg, *Phys. Rev. Lett.* **19**, 1264 (1967).
- [9] A. Salam and J. C. Ward, *Phys. Lett.* **13**, 168 (1964).
- [10] A. Salam *Elementary Particle Theory* (1968).
- [11] M. Gell-Mann, *Phys. Lett.* **8**, 214 (1964).
- [12] G. Zweig, CERN-8182-TH-401 (1964).
- [13] G. Zweig, CERN-8419-TH-412 (1964).
- [14] S. Eidelman *et al.* [Particle Data Group], *Phys. Lett. B* **592**, 1 (2004).
(URL: <http://pdg.lbl.gov>)
- [15] M. Y. Han and Y. Nambu, *Phys. Rev.* **139**, B1006 (1965).
- [16] O. W. Greenberg, *Phys. Rev. Lett.* **13**, 598 (1964).
- [17] G. D. Rochester and C. C. Butler, *Nature* **160** (1947) 855.
- [18] J. J. Aubert *et al.* [E598 Collaboration], *Phys. Rev. Lett.* **33**, 1404 (1974).

- [19] J. E. Augustin *et al.* [SLAC-SP-017 Collaboration], Phys. Rev. Lett. **33**, 1406 (1974).
- [20] S. W. Herb *et al.*, Phys. Rev. Lett. **39**, 252 (1977).
- [21] D. P. Barber *et al.*, Phys. Rev. Lett. **43**, 830 (1979).
- [22] F. Abe *et al.* [CDF Collaboration], Phys. Rev. D **50**, 2966 (1994).
- [23] R. K. Ellis, W. J. Stirling and B. R. Webber, Camb. Monogr. Part. Phys. Nucl. Phys. Cosmol. **8**, 1 (1996).
- [24] D. J. Gross and F. Wilczek, Phys. Rev. Lett. **30**, 1343 (1973).
- [25] H. D. Politzer, Phys. Rev. Lett. **30**, 1346 (1973).
- [26] P. M. Stevenson, Phys. Rev. D **23**, 2916 (1981).
- [27] G. Altarelli and G. Parisi, Nucl. Phys. B **126**, 298 (1977).
- [28] L. N. Lipatov, Sov. J. Nucl. Phys. **20**, 94 (1975) [Yad. Fiz. **20**, 181 (1974)].
- [29] V. N. Gribov and L. N. Lipatov, Sov. J. Nucl. Phys. **15**, 438 (1972) [Yad. Fiz. **15**, 781 (1972)].
- [30] Y. L. Dokshitzer, Sov. Phys. JETP **46** (1977) 641 [Zh. Eksp. Teor. Fiz. **73** (1977) 1216].
- [31] S. Chekanov *et al.* [ZEUS Collaboration], Eur. Phys. J. C **21**, 443 (2001) [arXiv:hep-ex/0105090].
- [32] C. Adloff *et al.* [H1 Collaboration], Eur. Phys. J. C **21**, 33 (2001) [arXiv:hep-ex/0012053].
- [33] L. W. Whitlow, E. M. Riordan, S. Dasu, S. Rock and A. Bodek, Phys. Lett. B **282**, 475 (1992).
- [34] J. J. Aubert *et al.* [European Muon Collaboration], Nucl. Phys. B **259**, 189 (1985).
- [35] M. Arneodo *et al.* [New Muon Collaboration], Nucl. Phys. B **483**, 3 (1997) [arXiv:hep-ph/9610231].
- [36] A. C. Benvenuti *et al.* [BCDMS Collaboration], Phys. Lett. B **223**, 485 (1989).

- [37] M. R. Adams *et al.* [E665 Collaboration], 470-GeV,” Phys. Rev. D **54**, 3006 (1996).
- [38] A. Baldit *et al.* [NA51 Collaboration], Phys. Lett. B **332**, 244 (1994).
- [39] E. A. Hawker *et al.* [FNAL E866/NuSea Collaboration], Phys. Rev. Lett. **80**, 3715 (1998) [arXiv:hep-ex/9803011].
- [40] F. Abe *et al.* [CDF Collaboration], Phys. Rev. Lett. **81**, 5754 (1998) [arXiv:hep-ex/9809001].
- [41] T. Affolder *et al.* [CDF Collaboration], Phys. Rev. D **64**, 032001 (2001) [Erratum-ibid. D **65**, 039903 (2002)] [arXiv:hep-ph/0102074].
- [42] B. Abbott *et al.* [D0 Collaboration], Phys. Rev. Lett. **86**, 1707 (2001) [arXiv:hep-ex/0011036].
- [43] W. Vogelsang and M. R. Whalley, J. Phys. G **23**, A1 (1997).
- [44] M. Gluck, E. Reya and A. Vogt, Z. Phys. C **67**, 433 (1995).
- [45] H. L. Lai *et al.* [CTEQ Collaboration], Eur. Phys. J. C **12**, 375 (2000) [arXiv:hep-ph/9903282].
- [46] H. L. Lai *et al.*, Phys. Rev. D **51**, 4763 (1995) [arXiv:hep-ph/9410404].
- [47] A. D. Martin, R. G. Roberts, W. J. Stirling and R. S. Thorne, Eur. Phys. J. C **4**, 463 (1998) [arXiv:hep-ph/9803445].
- [48] S. Alekhin, Phys. Rev. D **68**, 014002 (2003) [arXiv:hep-ph/0211096].
- [49] J. Pumplin, D. R. Stump, J. Huston, H. L. Lai, P. Nadolsky and W. K. Tung, JHEP **0207**, 012 (2002) [arXiv:hep-ph/0201195].
- [50] A. D. Martin, R. G. Roberts, W. J. Stirling and R. S. Thorne, Eur. Phys. J. C **28**, 455 (2003) [arXiv:hep-ph/0211080].
- [51] S. Chekanov *et al.* [ZEUS Collaboration], Phys. Rev. D **67**, 012007 (2003) [arXiv:hep-ex/0208023].
- [52] A. D. Martin, R. G. Roberts, W. J. Stirling and R. S. Thorne, Phys. Lett. B **531**, 216 (2002) [arXiv:hep-ph/0201127].
- [53] A. D. Martin, R. G. Roberts, W. J. Stirling and R. S. Thorne, Eur. Phys. J. C **23**, 73 (2002) [arXiv:hep-ph/0110215].
- [54] R. Brandelik *et al.* [TASSO Collaboration], Phys. Lett. B **114**, 65 (1982).

- [55] W. Braunschweig *et al.* [TASSO Collaboration], *Z. Phys. C* **47**, 187 (1990).
- [56] D. Bender *et al.*, *Phys. Rev. D* **31**, 1 (1985).
- [57] A. Petersen *et al.*, *Phys. Rev. D* **37**, 1 (1988).
- [58] Y. K. Li *et al.* [AMY Collaboration], *Phys. Rev. D* **41**, 2675 (1990).
- [59] D. Buskulic *et al.* [ALEPH Collaboration], *Z. Phys. C* **73**, 409 (1997).
- [60] G. Alexander *et al.* [OPAL Collaboration], *Z. Phys. C* **72**, 191 (1996).
- [61] G. Abbiendi *et al.* [OPAL Collaboration], *Eur. Phys. J. C* **27**, 467 (2003) [arXiv:hep-ex/0209048].
- [62] K. Ackerstaff *et al.* [OPAL Collaboration], *Z. Phys. C* **75**, 193 (1997).
- [63] G. Abbiendi *et al.* [OPAL Collaboration], *Eur. Phys. J. C* **16**, 185 (2000) [arXiv:hep-ex/0002012].
- [64] H. Aihara *et al.* [TPC/Two Gamma Collaboration], *Phys. Rev. Lett.* **61**, 1263 (1988).
- [65] P. Abreu *et al.* [DELPHI Collaboration], *Eur. Phys. J. C* **6**, 19 (1999).
- [66] R. Barate *et al.* [ALEPH Collaboration], *Phys. Rept.* **294**, 1 (1998).
- [67] B. Adeva *et al.* [L3 Collaboration], *Phys. Lett. B* **259**, 199 (1991).
- [68] K. Ackerstaff *et al.* [OPAL Collaboration], *Eur. Phys. J. C* **7**, 369 (1999) [arXiv:hep-ex/9807004].
- [69] G. S. Abrams *et al.*, *Phys. Rev. Lett.* **64**, 1334 (1990).
- [70] J. Binnewies, B. A. Kniehl and G. Kramer, *Phys. Rev. D* **52**, 4947 (1995) [arXiv:hep-ph/9503464].
- [71] S. Kretzer, *Phys. Rev. D* **62**, 054001 (2000) [arXiv:hep-ph/0003177].
- [72] B. A. Kniehl, G. Kramer and B. Potter, *Nucl. Phys. B* **582**, 514 (2000) [arXiv:hep-ph/0010289].
- [73] L. Bourhis, M. Fontannaz, J. P. Guillet and M. Werlen, *Eur. Phys. J. C* **19**, 89 (2001) [arXiv:hep-ph/0009101].

- [74] L. Bourhis, M. Fontannaz and J. P. Guillet, *Eur. Phys. J. C* **2**, 529 (1998) [arXiv:hep-ph/9704447].
- [75] J. F. Owens, *Rev. Mod. Phys.* **59**, 465 (1987).
- [76] L. Apanasevich *et al.* [Fermilab E706 Collaboration], *Phys. Rev. D* **70**, 092009 (2004) [arXiv:hep-ex/0407011].
- [77] G. Balocchi *et al.* [UA6 Collaboration], *Phys. Lett. B* **436**, 222 (1998).
- [78] G. Sozzi *et al.* [UA6 Collaboration], *Phys. Lett. B* **317**, 243 (1993).
- [79] D. L. Adams *et al.* [E704 Collaboration], *Phys. Lett. B* **345**, 569 (1995).
- [80] A. L. S. Angelis *et al.* [CMOR Collaboration], *Nucl. Phys. B* **327**, 541 (1989).
Prompt photon production data WA70
- [81] M. Bonesini *et al.* [WA70 Collaboration], *Z. Phys. C* **38**, 371 (1988).
- [82] C. De Marzo *et al.* [NA24 Collaboration], *Phys. Rev. D* **36**, 8 (1987).
- [83] E. Anassontzis *et al.*, *Z. Phys. C* **13**, 277 (1982).
- [84] C. Albajar *et al.* [UA1 Collaboration], *Phys. Lett. B* **209**, 385 (1988).
- [85] J. Alitti *et al.* [UA2 Collaboration], *Phys. Lett. B* **288**, 386 (1992).
- [86] F. Abe *et al.* [CDF Collaboration], *Phys. Rev. Lett.* **73**, 2662 (1994) [Erratum-*ibid.* **74**, 1891 (1995)].
- [87] S. Abachi *et al.* [D0 Collaboration], *Phys. Rev. Lett.* **77**, 5011 (1996) [arXiv:hep-ex/9603006].
- [88] M. J. Alguard *et al.*, *Phys. Rev. Lett.* **37**, 1261 (1976).
- [89] G. Baum *et al.*, *Phys. Rev. Lett.* **51**, 1135 (1983).
- [90] J. Ashman *et al.* [European Muon Collaboration], *Phys. Lett. B* **206**, 364 (1988).
- [91] J. Ashman *et al.* [European Muon Collaboration], *Nucl. Phys. B* **328**, 1 (1989).
- [92] P. L. Anthony *et al.* [E142 Collaboration], *Phys. Rev. D* **54**, 6620 (1996) [arXiv:hep-ex/9610007].

- [93] K. Abe *et al.* [E143 collaboration], Phys. Rev. D **58**, 112003 (1998) [arXiv:hep-ph/9802357].
- [94] K. Abe *et al.* [E154 Collaboration], Phys. Rev. Lett. **79**, 26 (1997) [arXiv:hep-ex/9705012].
- [95] P. L. Anthony *et al.* [E155 Collaboration], Phys. Lett. B **463**, 339 (1999) [arXiv:hep-ex/9904002].
- [96] B. Adeva *et al.* [Spin Muon Collaboration], Phys. Rev. D **58**, 112001 (1998).
- [97] K. Ackerstaff *et al.* [HERMES Collaboration], Phys. Lett. B **404**, 383 (1997) [arXiv:hep-ex/9703005].
- [98] A. Airapetian *et al.* [HERMES Collaboration], Phys. Lett. B **442**, 484 (1998) [arXiv:hep-ex/9807015].
- [99] A. Airapetian *et al.* [HERMES Collaboration], Phys. Rev. Lett. **84**, 2584 (2000) [arXiv:hep-ex/9907020].
- [100] G. Bunce, N. Saito, J. Soffer and W. Vogelsang, Ann. Rev. Nucl. Part. Sci. **50**, 525 (2000) [arXiv:hep-ph/0007218].
- [101] Z. Fodor and S. D. Katz, JHEP **0203**, 014 (2002) [arXiv:hep-lat/0106002].
- [102] M. Gyulassy and X. n. Wang, Nucl. Phys. B **420**, 583 (1994) [arXiv:nucl-th/9306003].
- [103] X. N. Wang and Z. Huang, Phys. Rev. C **55**, 3047 (1997) [arXiv:hep-ph/9701227].
- [104] R. Baier, Y. L. Dokshitzer, S. Peigne and D. Schiff, Phys. Lett. B **345**, 277 (1995) [arXiv:hep-ph/9411409].
- [105] B. G. Zakharov, JETP Lett. **65**, 615 (1997) [arXiv:hep-ph/9704255].
- [106] H. Hahn *et al.*, Nucl. Instrum. Meth. A **499**, 245 (2003).
- [107] Y. S. Derbenev, A. M. Kondratenko, S. I. Serednyakov, A. N. Skrinsky, G. M. Tumaikin and Y. M. Shatunov, Part. Accel. **8**, 115 (1978).
- [108] K. Adcox *et al.* [PHENIX Collaboration], Nucl. Instrum. Meth. A **499**, 469 (2003).

- [109] S. H. Aronson *et al.* [PHENIX Collaboration], Nucl. Instrum. Meth. A **499**, 480 (2003).
- [110] K. Adcox *et al.* [PHENIX Collaboration], Nucl. Instrum. Meth. A **499**, 489 (2003).
- [111] M. Aizawa *et al.* [PHENIX Collaboration], Nucl. Instrum. Meth. A **499**, 508 (2003).
- [112] L. Aphecetche *et al.* [PHENIX Collaboration], Nucl. Instrum. Meth. A **499**, 521 (2003).
- [113] H. Akikawa *et al.* [PHENIX Collaboration], Nucl. Instrum. Meth. A **499**, 537 (2003).
- [114] M. Allen *et al.* [PHENIX Collaboration], Nucl. Instrum. Meth. A **499**, 549 (2003).
- [115] S. S. Adler *et al.* [PHENIX Collaboration], Nucl. Instrum. Meth. A **499**, 560 (2003).
- [116] S. S. Adler *et al.* [PHENIX Collaboration], Nucl. Instrum. Meth. A **499**, 593 (2003).
- [117] C. Adler, A. Denisov, E. Garcia, M. Murray, H. Strobele and S. White, Nucl. Instrum. Meth. A **470**, 488 (2001) [arXiv:nucl-ex/0008005].
- [118] K. H. Ackermann *et al.* [STAR Collaboration], Nucl. Instrum. Meth. A **499**, 624 (2003).
- [119] B. B. Back *et al.* [PHOBOS Collaboration], Nucl. Instrum. Meth. A **499**, 603 (2003).
- [120] M. Adamczyk *et al.* [BRAHMS Collaboration], Nucl. Instrum. Meth. A **499**, 437 (2003).
- [121] WA98 Collaboration, CERN Report. No. SPSLC 91-17 (1991).
- [122] GEANT 3.21, CERN Program Library
<http://wwwasd.web.cern.ch/wwwasd/geant/index.html>
- [123] PYTHIA v5.720 <http://www.thep.lu.se/~torbjorn/Pythia.html>
- [124] S. S. Adler *et al.* [PHENIX Collaboration], Phys. Rev. Lett. **91**, 241803 (2003) [arXiv:hep-ex/0304038].

- [125] S. S. Adler *et al.* [PHENIX Collaboration], Phys. Rev. Lett. **94**, 082301 (2005) [arXiv:nucl-ex/0409028].
- [126] <http://physics.nist.gov/PhysRefData>
- [127] R. F. Cahalan, K. A. Geer, J. B. Kogut and L. Susskind, Phys. Rev. D **11**, 1199 (1975).
- [128] J. Murata *et al.*, Nucl. Instrum. Meth. A **500**, 309 (2003) [arXiv:nucl-ex/0212027].